ENGINEERING APPROACHES FOR NERVE REPAIR

By

Chun Liu

A DISSERTATION

Submitted to
Michigan State University
in partial fulfillment of the requirements
for the degree of

Chemical Engineering - Doctor of Philosophy

2015

ABSTRACT

ENGINEERING APPROACHES FOR NERVE REPAIR

Bv

Chun Liu

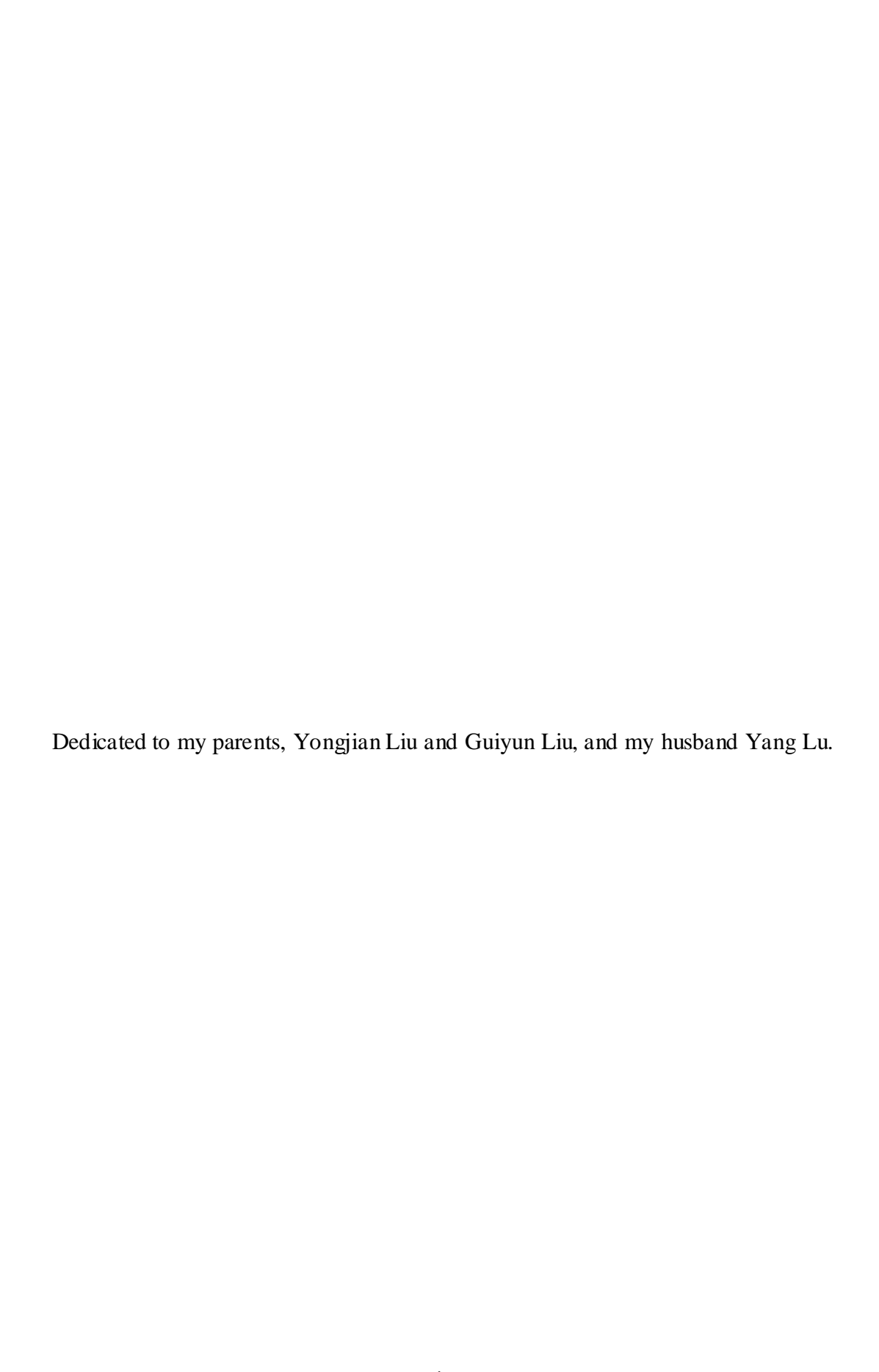
Spinal cord injury (SCI) has been shown to result in devastating consequences including temporary or permanent deficit in sensory as well as motor function. The regeneration of nerves is found to be a chaotic process due to unorganized axon alignment. Therefore, properly organized axonal alignment is necessary to bridge the lesion site. Furthermore demyelination after SCI strongly impairs the conductive capacity of surviving axons, remyelination is critical for proper function of the regenerated nerves. Schwann cells (SCs) migrate and aid both spinal cord and peripheral nerve injury repairs, as SCs are responsible for remyelination of the regenerated axons and provide guidance for regrowing axons. Therefore, SC migration is a key in axon regeneration and remyelination. This study focuses on developing engineering approaches to enhance axon regeneration and SC migration to promote remyelination.

We first demonstrate that mesenchymal stem cells aligned on pre-stretch induced anisotropic surface due to sensing a larger effective stiffness in the stretched direction than in the perpendicular direction. Next we show that an anisotropic surface arising from mechanical pre-stretch impacts axonal alignment and myelination. Culturing dorsal root ganglia (DRG) neuron cells on pre-stretched surfaces induced alignment of the regenerated axons in the direction of the pre-stretch, and further increased the thickness of the axons over those on an unstretched surface. Subsequent co-culture of the DRGs with the SCs showed preferential attachment of the SCs to the aligned axons and expression of the myelin component protein P0 by the SCs. Taken together

the results establish that a pre-stretch induced anisotropic surface enhances axon alignment, thickness, and myelination.

SCs play an instrumental role in aiding nerve repair. To better optimize the design of transplantable scaffolds, we studied the influence of channel diameter on the migration behavior of large populations of SCs over a period of two weeks. Micropatterned polydimethylsiloxane (PDMS) channel surfaces with different channel sizes served to mimic the varying channel sizes of transplantable scaffolds *in vitro*. The average cell migration speeds were quantified and normalized using two methods. We found higher SC migration speeds on PDMS channels with decreasing channel sizes. These results suggest that scaffold channel size provides a means to manipulate SC migration into the scaffold for nerve repair.

Finally to test the axon growth in microchannels, we further co-cultured DRGs and SCs at opposite ends of micropatterned channels of varying sizes. Freshly isolated DRGs were seeded at one end of the channels and SCs were seeded at the other end to provide growth factors to the axons. As a positive control, in lieu of SCs, collagen gel pre-loaded with Nerve Growth Factor (NGF) was added at one end of the channels. The results indicate that the addition of SCs or the NGF encapsulated gel effectively attracted axons to penetrate into the microchannels as compared to the negative control (blank control without SCs or NGF).



ACKNOWLEDGEMENTS

First, I would like to thank Dr. Christina Chan for being my research and life mentor throughout my PhD career. Without her careful and patient instruction, my future as a scientist and engineer would have been impossible. In addition, I thank all my thesis committee members, Dr. S Patrick Walton, Dr. Seungik Baek, and Dr. Neil Wright for providing constant guidance and support throughout the duration of my PhD.

I would also like to thank the past and present members of the Chan and Walton lab, Sumit Mehrotra, Linxia Zhang, Li Liu, Hyunju Cho, Ryan Thompson, Phil Angart, and Daniel Vocelle for being great colleagues and always displaying a zealous attitude in fostering collaborations. Especially, I want to thank all the undergraduate students with whom I have worked with, Ryan Pyne, Eric Vasko, Victoria Toomajian, and Jeremy Kray.

I'm also grateful to all my collaborators, Dr. Seungik Baek' group (Mechanical Engineering, Michigan State University), Dr. Jeff Sakamoto's (Mechanical Engineering, University of Michigan), and Dr. Mark Tuszynski's group (Neuroscience, University of California, San Diego).

I'd like to acknowledge Dr. Melinda Frame at the Center of Advanced Microscopy, Dr. Baokang Bi at the Keck Microfabrication Facility, Dr. Wen Li and Dr. Xiaopeng Bi for their help on photolithography, and Dr. Ning Xi and Dr. Bo Song for their help with AFM.

Last, I would like to thank my loving husband Dr. Yang Lu for his unconditional love and his advisor Dr. Andre Lee for being the witness at our wedding. Life is tough, but love is stronger. I'm thankful for all the kind help I received in the past 6 years and the nourishment it provided.

TABLE OF CONTENTS

LIST OF TABLES	X
LIST OF FIGURES	xi
LIST OF ABBREVIATIONS	xiii
CHAPTER 1 INTRODUCTION	1
1.1 Spinal cord injury	1
1.2 Potential of tissue engineering for treating SCI	
1.3 Material properties of PDMS	
1.4 Aims and objectives	
1.4.1 Design of pre-stretch induced anisotropic surface	11
1.4.2 Design of micropatterned channels for SC migration	
1.5 Conclusions and future work	14
ANISOTROPY ON ORIENTATION OF MESENCHYMAL STEM CELLS	15
2.2 Materials and methods	
2.2.2 PDMS substrate preparation	
2.2.4 Cell culture	
2.2.5 Quantification of cell orientation distribution and cell length	
2.2.6 Immunocytochemistry	
2.2.7 Statistical analyses	
2.3 Estimation of stretch-induced anisotropy	
2.3.1 Estimation of pre-stretch-induced anisotropy of the substrate in active cellular.	
small on large theory	_
2.3.2 Characterization of finite elastic behavior of the substrate	25
2.3.3 Estimation of stretch induced anisotropic response of substrate in active sensing	
2.4. Experimental results	_
2.4.1 Surface topography characterization	29
2.4.2 Orientation quantification	31
2.4.3 Actin cytoskeleton alignment and cell morphology change	
2.4.4 MSC differentiation potential on pre-stretched surface	39
2.5 Discussion	
2.5.1 Bio-mechanical environment	
2.5.2 Static vs. cyclic stretching	42

2.5.3 Pre- vs. post-stretch	43
2.5.4 Mechanical force vs. contact guidance	
2.5.5 PLL vs. fibronectin coating	
2.5.6 Application of mechanical stretch in tissue engineering	
CHAPTER 3 THE IMPACT OF PRE-STRETCH INDUCED SURFACE ANISO ON AXON GROWTH	
3.1 Introduction	
3.2 Materials and methods	
3.2.1 Materials	
3.2.2 Pre-stretched PDMS substrate preparation	
3.2.3 PDMS channel substrate preparation	
3.2.4 PDMS surface characterization	
3.2.5 Tensile test	
3.2.6 DRG neuron and Schwann Cell isolation and culture	
3.2.7 Immunocytochemistry	
3.2.8 Quantification of axon orientation distribution and axon thickness	
3.2.9 Quantification of co-localization of axon and SCs	
3.2.10 Statistical analyses	
3.3 Results and discussion	
3.3.1 Design and characterization of pre-stretched surface	
3.3.2 Axon alignment on pre-stretched surface	
3.3.3 Enhanced axon thickness growth on pre-stretched surface	
3.3.4 Co-culture of Schwann cells with aligned axons	
J	
CHAPTER 4 SCHWANN CELLS MIGRATION ON PATTERNED PDMS	
MICROGROOVED SURFACE	
4.1 Introduction	
4.2 Materials and methods	
4.2.1 Materials	
4.2.2 Microgrooved substrate fabrication	
4.2.3 Cell culture	
4.2.4 Immunocytochemistry	
4.2.5 Migration quantification	
4.3 Results and discussion	
4.3.1 Design of microgrooved substrate	
4.3.2 Schwann cells migrated on both the grooves and ridges	
4.3.3 Comparison of SC migration on different microgrooved surfaces	
4.3.4 Comparison of SC alignment in different channels	
4.4 Conclusion	94
CHAPTER 5 SCS ENHANCE REGENERATED AXONS PENETRATION INTO	
PATTERNED CHANNELS	95
5.1 Introduction	0.5

	97
5.2.1 Materials	97
5.2.2 Patterned channel cell co-culture system fabrication	97
5.2.3 DRG neuron and Schwann Cell isolation and culture	98
5.2.4 Fluorescent imaging	99
5.2.5 Pre-loaded collagen gel with NGF	
5.2.6 Quantification of axon penetration depth	100
5.2.7 Statistical analyses	
5.3 Results and discussion	
5.3.1 Design of the patterned channel cell co-culture system	101
5.3.2. Axons penetration into patterned channels	
5.3.3 Comparison of axon penetration depth under different conditions	105
CHAPTER 6 CONCLUSION AND FUTURE WORK	110
6.1 Summary	110
	110
6.1 Summary	110 112
6.1 Summary	110 112 112
6.1 Summary	110 112 112
6.1 Summary	110112112 scaffold design
6.1 Summary	110112112 scaffold design
6.1 Summary	110 112 112 112 scaffold design 114

LIST OF TABLES

Table 1.1. NTFs involved in neural regeneration after SCI	8
Table 6.1. LbL application in neural adhesion	121
Table A.1. Grid record of SC migration on day 8 for 50 µm (a), 100 µm (b), and 150 µm (c) microgrooved surfaces.	130
Table A.2. Grid record of SC migration on day 9 for 50 µm (a), 100 µm (b), and 150 µm (c) microgrooved surfaces.	132
Table A.3. Grid record of SC migration on day 10 for 50 μm (a), 100 μm (b), and 150 μm (c) microgrooved surfaces.	133
Table A.4. Grid record of SC migration on day 13 for 50 µm (a), 100 µm (b), and 150 µm (c) microgrooved surfaces.	135
Table A.5. Grid record of SC migration on day 14 for 50 µm (a), 100 µm (b), and 150 µm (c) microgrooved surfaces.	136
Table A.6. Grid record of SC migration on day 15 for 50 µm (a), 100 µm (b), and 150 µm (c) microgrooved surfaces.	138

LIST OF FIGURES

Figure 1.1. Templated agarose scaffold supports linear growth of axons.	5
Figure 1.2. Schematic of crosslinked polymer chain molecules.	. 10
Figure 2.1. Schematic illustrating stretch induced anisotropy.	. 18
Figure 2.2. Design of static pre-stretching device	24
Figure 2.3. Schematic drawing of the two-step deformation of the substrate in the experiment.	27
Figure 2.4. Stress-strain plot.	28
Figure 2.5. Effective stiffness.	29
Figure 2.6. Surface topological characterization.	30
Figure 2.7. MSCs on stretched vs. unstretched PDMS substrate.	32
Figure 2.8. Quantification of the orientation angles on stretched vs. unstretched membrane	33
Figure 2.9. Ratios of parallel orientation vs. magnitude of pre-stretch.	34
Figure 2.10. Actin filaments and focal adhesion staining of MSCs on stretched vs. unstretched surfaces.	
Figure 2.11. MyoD1 Staining of MSCs on stretched vs. unstretched surfaces	. 40
Figure 2.12. MSC orientation upon stretching of cell-attached PDMS surface.	. 45
Figure 2.13. MSC oriented on fibronectin coated pre-stretched surface.	47
Figure 3.1. Pre-stretched PDMS substrate and surface characterization.	. 60
Figure 3.2. Axon alignment on pre-stretched and unstretched surface.	62
Figure 3.3. Quantification of axon alignment on stretched vs. unstretched PDMS substrate	. 64
Figure 3.4. Axon thickness growth on stretched vs. unstretched PDMS substrate	. 68
Figure 3.5 Quantification of axon thickness on micropatterned PDMS substrate	. 70
Figure 3.6. Co-cultured of Schwann cells with the DRG neurons on the stretched vs. unstretch PDMS substrates.	
Figure 4.1. Schematic of channel design and PDMS preparation.	80

Figure 4.2. Migration of Schwann Cells (SCs) into the channels.	86
Figure 4.3. Flowcharts illustrating the various steps in the quantification of SC migration	-
Figure 4.4. Comparison of SC migration in the different size channels using the leading edvelocity.	dge
Figure 4.5. Comparison of SC migration in the different size channels using the binary ve	•
Figure 4.6. Comparison of SC alignment in the different size channels.	
Figure 5.1. Schematic of micropatterned co-culture platform.	102
Figure 5.2. Penetration of regenerated axons into channels.	104
Figure 5.3. Quantification of axon penetration depth.	105
Figure 5.4. Comparison between different channel sizes in SC group.	106
Figure 5.5. Comparison of SCs group with positive and negative control groups for each c size.	
Figure 6.1. Schematic of pre-stretched microchannel design.	114
Figure 6.2. Applicability of the LbL technology for SCI repair.	115
Figure 6.3. Co-culture of primary neurons and astrocytes on LbL-coated surfaces	123
Figure 6.4. Lysozyme release profile from LbL for 4 weeks.	127
Figure A.1. Definition of leading edge.	139
Figure A.2. Binary processing method.	140
Figure A.3. Plot of average position at leading edge vs. time.	141
Figure A.4. Plot of migration velocity with channel size.	141

LIST OF ABBREVIATIONS

AraC: 1-P-D-Arabino-furanosylcytosine

BDNF: Brain derived neurotrophic factor

BPE: Bovine pituitary extract

BSA: Bovine serum albumin

CNS: Central nervous system

CNT: Carbon nanotube

DRG: Dorsal root ganglion

ECM: Extracellular matrix

FBS: Fetal bovine serum

FDU-U: Fluoro-2 deoxy-uridine-Uridine,

GDNF: Glial cell line-derived neurotrophic factor

HA: Hyaluronic acid

LbL: Layer-by-layer

MSCs: Mesenchymal stem cells

NGF: Nerve growth factor

PAA: Poly (acrylic acid)

PAH: Poly (allylamine hydrochloride)

PBS: Phosphate buffered saline

PDAC: Poly (diallyldimethylammonium chloride)

PDMS: Polydimethylsiloxane

PEG: Poly (ethylene glycol)

PEM: Polyelectrolyte multilayer

PGA: Poly (glycolic acid)

PLA: Poly (lactic acid)

PLL /PDL: Poly-L (D)-lysine

PLGA: Poly (lactic-co-glycolic acid)

PNS: Peripheral nervous system

SCs: Schwann cells

SCI: Spinal cord injury

SEM: Scanning electron microscopy

SPS: Sulfonated poly (styrene), sodium salt

3D: Three dimensional

CHAPTER 1 INTRODUCTION

1.1 Spinal cord injury

Spinal cord injury (SCI) is a leading cause of disability worldwide. In the United States, the prevalence of SCI is ~250,000 out of 300 million with 11,000 new incidences each year [1]. SCI is ranked as one of the major causes of disability in young people, with an average age at injury of 33.4 years [2]. Defined as an occurrence of an acute traumatic lesion of neural elements in the spinal canal, which connect descending motor systems to the body and ascending sensory circuits to the brain, SCI results in temporary or permanent deficits in motor and sensory function [3]. In this chapter, we discuss current therapies for spinal cord injury and outline potential recovery strategies through tissue engineering approaches. These include transplantable scaffolds [4] and engineered neural cell differentiation/migration [5-6]. The findings that polyelectrolyte multilayer (PEM) coated surfaces are able to enhance neural cell adhesion and differentiation [7-8] suggest their potential to contribute to the treatment of SCIs.

Tissue damage after SCI occurs in two phases, a primary damage phase directly resulting from the trauma and a secondary damage phase which occurs post-trauma. Within the first 48 hours after SCI, the acute primary lesion causes extensive neuron and glial cell necrosis, followed by vascular damage-induced spinal cord swelling and glutamate excitotoxicity [9]. Secondary damage starts just after primary tissue destruction and usually lasts over several days or weeks, and involves necrosis of some neurons and apoptosis of some glia. Poor axon regeneration, axon demyelination, and inflammation are three major complications which arise after SCI. After acute SCI, axons sprout briefly, but soon undergo growth arrest and retraction. Lack of growth factors secreted by associated glial cells and the lack of orientation of neurites inside the scar tissue prevent axons from crossing the lesion site [9-10]. Therefore, reorganization of axon

connections requires not only a bridge to facilitate axon alignment, but also the local release of growth factors to enhance the axon growth and myelination. During the process of myelination, a myelinating cell wraps around an axon to build a myelin sheath, which is necessary for rapid conduction of action potentials along the axon. Myelination is accomplished by oligodendrocytes in the central nervous system (CNS) and Schwann cells in the peripheral nervous system [11]. Oligodendrocytes are quite sensitive to SCI and undergo both necrotic and apoptotic cell death after trauma. Therefore, SCI is usually accompanied by chronic progressive demyelination, which in turn affects neural function and axon survival [12]. Upon breakdown of the myelin sheath within the first few hours after injury, the debris from the myelin breakdown spreads to and further inhibits the growth of neighboring healthy neurons, followed by macrophage infiltration and inflammation [1, 9]. The degradation of myelin sheaths also exposes myelin-associated proteins such as Nogo, myelin associated glycoprotein (MAG) and oligodendrocyte myelin glycoprotein (OMgP), which hamper axonal regeneration by collapsing the axonal growth cone [13].

Nerve regeneration after SCI is a multi-step process. First, the injured neuron must survive, and then the regenerated axon must extend its processes in the same path as its original path/direction and form contacts with target neurons. As the processes extend, the axons need to be remyelinated and form functional synapses on the surface of the targeted neurons. Therefore, myelination is a significant step for neural function recovery. There is some remyelination of axons by oligodendrocyte precursor cells that reside in the spinal cord, although the precise extent of this response and its functional consequences are unclear. Alternatively, Schwann cells migrate into areas of spinal cord injury and can also remyelinate axons [14]. The influx of Schwann cells not only helps with remyelination, but may also offer other benefits to

regenerating axons, such as growth factors. However, whereas Schwann cells are a critical component underlying the success of peripheral nerve regeneration [15], the endogenous Schwann cells response to SCI is insufficient to meaningfully impact anatomical reconstruction and functional recovery. Efforts have been made to transplant Schwann cells to the injured spinal cord, resulting in a partial reduction in secondary damage and improved axon growth as well as myelination [16-17]; these findings suggest the potential importance of Schwann cells as therapies for SCI.

Therapeutic approaches for SCI span a broad range of goals including: (1) decreasing glial scar formation to provide a permissive environment for axon outgrowth, (2) replacing lost cells through stem cell or progenitor cell transplantation, (3) transplanting olfactory ensheathing cells or Schwann cells to provide a permissive substrate for axonal growth into the injury site, and (4) placing either peripheral nerve grafts or engineered scaffolds into the lesion site to provide both a permissive substrate and guidance for regenerating axons [1-3]. However, due to the complexity of SCI pathology and limited knowledge of cell and scaffold interactions, breakthroughs in nerve tissue engineering have been limited. Developing scaffolds with strong regenerative and cell-supporting capabilities that not only enhance the organization of the regenerating nerves but also improve myelination of these nerves to function properly, is central to nerve tissue engineering for SCI repair.

1.2 Potential of tissue engineering for treating SCI

Axon formation, a key event of neuronal polarization, requires coordinated rearrangement of the cytoskeleton [18]. Cytoskeleton reorganization is dependent on cell-substrate adhesion and plays a vital role in advancing axons. Thus, engineered substrates must be designed to modulate this process to promote axon guidance for tissue repair after SCI. Tissue engineering methods have

been explored for many years to build biomedical scaffolds to augment, repair, or replace damaged tissue *in vivo*. Engineered surfaces with varying chemistries and topographies have provided insight into cell responses and led to modifications of 3D scaffolds that better support cells for tissue formation [19]. In this section, we provide an overview of the key issues related to tissue engineering research as applied to SCI, ranging from cell-substrate interactions to incorporation of soluble factors into substrates. A major goal in repairing and treating SCI is to optimize the physical and chemical properties of the scaffold.

Biomaterial scaffolds provide an environment within which cells organize to form an artificial tissue in a highly controlled manner. The scaffold functions to guide cell behavior by facilitating cell-substrate and cell-cell interactions. As shown in Figure 1.1, agarose scaffolds containing linear guidance channels (200 mm diameter) generated with a fiber templating technology, can support the growth of aligned long-tract axons in the spinal cord lesion site [20]. Thus, to ensure the chemical and physical properties of the scaffold for neural regeneration after SCI elicit the desired cellular response, they should have the following characteristics: (1) possess substrate stiffness and anisotropic features such as channels or fibers of appropriate scale to direct axon alignment, (2) be biodegradable with controlled drug release capability, (3) have proper surface chemistry to control neural cell attachment, differentiation and migration, (4) possess sufficient mechanical integrity for implantation and handling [1-2, 4, 21-23].

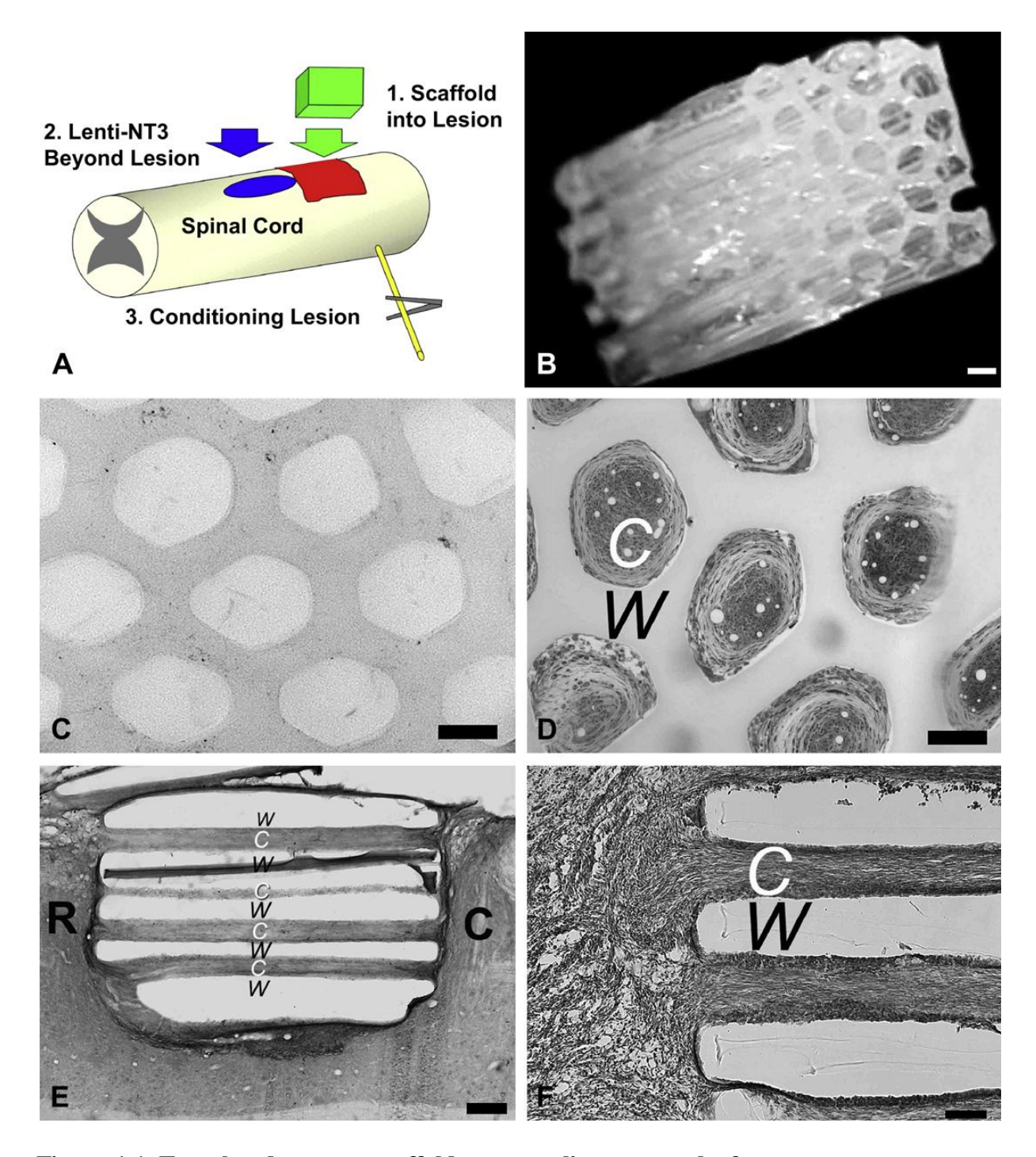


Figure 1.1. Templated agarose scaffold supports linear growth of axons.

(a) Schematic of scaffold implantation at the lesion site includes (1) scaffold implantation, (2) injection of lentiviral vectors expressing NT-3 beyond the lesion to attract regenerating axons, and, (3) lesion conditioning lesions to promote the growth of the axon. (b) Macroscopic the

(Figure 1.1 cont'd) architecture of the templated agarose scaffold. (c) Cross-section of the scaffold channels prior to implantation. (d) Scaffold stained with toluidene Blue 4 weeks after implantation. Channels are filled with cells. (e, f) Scaffold integration into the lesion site. Notations: W = walls of the scaffold; C = channels of the scaffold (containing cells); R and C label represent the rostral and caudal locations of the lesion, respectively. Scale bars: (b) 200 μ m, (c) 100 μ m, (d) 250 μ m, (e), (f) 100 μ m [20]. (Reproduced with permission from Ref. [20]. Copyright Elsevier Ltd.)

When designing a scaffold for neural tissue regeneration, a primary consideration is the choice of material. The vast number of biodegradable synthetic and natural biopolymers makes choosing the material a challenge. Synthetic polymers with well characterized properties have been widely used in tissue engineering applications. With a reliable source of raw materials, these polymers, such as poly ethylene glycol (PEG), poly-β-hydroxybutyrate (PHB), and poly-ε-caprolactone (PCL), can be tailored to provide a broad range of mechanical properties and degradation rates. In addition, synthetic polymers can be designed to achieve desired qualities, for example poly (glycolic acid) (PGA) and poly (lactic acid) (PLA) can be reacted to form the copolymer poly (lactic-co-glycolic acid) (PLGA) which is hydrophilic and have strong mechanical properties [24]. However, synthetic polymers have been found to provoke an immune response after transplantation as compared with natural materials [25]. Natural polymers, such as commonly derived proteins or carbohydrate polymers have been used as scaffolds for growing several types of tissues. These materials, such as collagen, fibronectin, chitosan, agarose, and alginate, are considered ideal matrices for engineered tissue constructs due to their non-toxic, noninflammatory properties [26] and similarity in structure and stiffness to the tissue being replaced.

Natural materials function biologically at the molecular level and are readily degraded and metabolized. Despite these advantages, natural materials are predominantly derived from animal sources which limit their application. Moreover, their complex structure and reduced liability (i.e. harder to control their mechanical properties) make them more difficult to manufacture.

Optimizing the chemical and physical properties are significant challenges in scaffold design. Tissue engineering strategies for controlling neuronal cell adhesion and axon guidance can be categorized into three main areas of design: surface chemistry, contact guidance, and stiffness [19]. While stiffness of substrate has been manipulated to control neuronal cell adhesion [27], contact guidance [28] and surface chemistry using gradients of extracellular matrix (ECM) proteins [29] are commonly used to control axon growth. Contact guidance describes a phenomenon by which cells respond to extracellular topography, both isotropic and anisotropic topographies, by altering the cell morphology, orientation, and motility. Patterned surfaces chemistry with cell adhesive molecules such as ECM proteins has been found to guide axons as well as glial cell alignment [30]. For tissue repair after SCI, scaffolds using either engineered fibers or channels, which direct axon outgrowth to bridge the lesion site, have shown promising results [4].

The re-establishment of functional nerve connections in the scaffold further requires growth factors. *In situ* delivery of growth factors that enhance axon growth or anti-inflammatory drugs that suppress inhibitory molecules to axon growth are critical components for successful SCI therapies. Neurotrophic factors (NTFs) consist of several families of structurally related growth factors in the nervous system that enhance the growth and survival of developing neurons and maintain the function of mature neurons (Table 1.1), and thus have been incorporated into

transplantable scaffolds in tissue engineering applications for SCI [31]. The efficacy of a particular NTF is influenced by the delivery method, the site of release, the specific axonal system involved, the expression level of NTF receptors after injury and the presence of a substrate [5].

Table 1.1. NTFs involved in neural regeneration after SCI

Abbreviation	Full name	Main function	Reference
NGF	Nerve growth factor	Survival and maintenance of sympathetic and sensory neurons	Fiore et al. [32]
BDNF	Brain-derived neurotrophic factor	Survival, differentiation and maintenance of multiple brain and spinal cord neurons; neurogenesis	Binder et al. [33]
NT-3	Neurotrophin-3	Survival and differentiation of hippocampal, cortical and spinal motor and sensory neurons	Maisonpierre et al. [34]
FGF	Fibroblast growth factor	Survival and differentiation of multiple neurons; neurogenesis	Zechel et al. [35]
PDGF	Platelet-derived growth factor	Proliferation of oligodendrocyte progenitor cells	Barres et al. [36]
GDNF	Glial cell line-derived neurotrophic factor	Survival of motor and sensory neurons; enhance Schwann cell migration and myelination	Deng et al. [37]

1.3 Material properties of PDMS

Polydimethylsiloxane (PDMS) is one of the most extensively used polymers to study cell–substrate interactions due to its tunable mechanical properties. It is easy to achieve a physiologically relevant range of mechanical properties (1kPa to 2 MPa) with PDMS through varying crosslinking [38]. The chemical formula for PDMS is (H₃C)₃SiO[Si(CH₃)₂O]nSi(CH₃)₃, where n is the number of repeating monomer [SiO(CH₃)₂] units. Network of PDMS polymer is assembled by crosslinking the polymer chains which usually have vinyl groups at each end, using short crosslinker (polymethylhydro-siloxane) [39].

To test the mechanical property of PDMS, usually a large-deformation tension experiment is conducted on macroscale specimens, while microscale tension experiments have also been tested on thin-film through micro-indentation [40-41]. Results from both stress-strain curve and force-depth curve have indicated a non-linear, large-deformation rubber-elasticity model to represent the behavior of PDMS [42].

Similar to rubber, the outstanding elastic property of PDMS can be explained by the molecular chain crosslinked network. The crosslinked molecular chains show highly twisted, kinked, and coiled morphology in an unstressed state, which results in an amorphous elastomer. Upon a tensile load, elastic deformation will occur which involves in partial uncoiling, untwisting, and straightening, and hence elongation of the chains in the stress direction, as shown in Figure 1.2. Once the stress is released, the chains will spring back to their unstressed conformations, resulting in the macroscopic piece to return to its original shape. During the elastic deformation, the crosslinkers act as anchor points between the chains, preventing the chain slippage to maintain the stability [43].

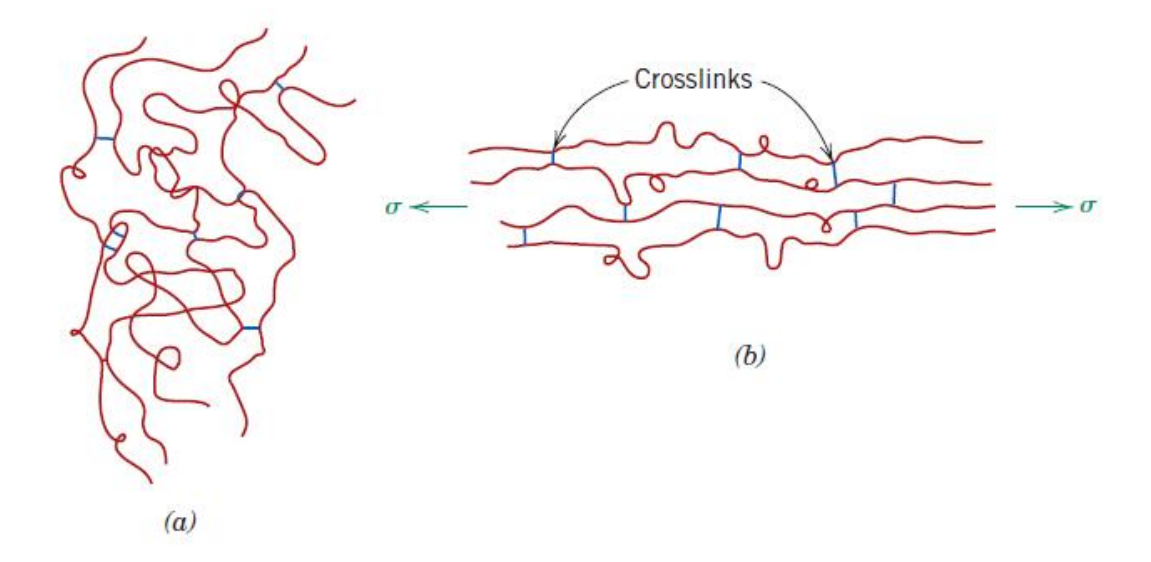


Figure 1.2. Schematic of crosslinked polymer chain molecules.

(a) Crosslinked polymer chain in an unstressed state and (b) during elastic deformation in response to an applied tensile load [43].

Besides the mechanical property, the surface chemistry also plays a role in regulating cell response. Due to the hydrophobic nature, it is rather difficult to maintain long-term culture of cells on PDMS. The challenge remains to modify the surface of PDMS with a stable cell-adhesive layer, as the high chain mobility of PDMS can lead to surface reorganization [44]. One common solution is through plasma treatment, where the hydrophobic surface of PDMS has been found to turn into hydrophilic upon oxygen plasma treatment. The process conditions affect the surface wettability significantly. Recently there has been study reporting that lower RF power with shorter duration makes a thin layer of undamaged oxide on the surface of PDMS with active silanol groups, which largely facilitates an irreversible hydrophilic coating [45]. Long-term stability of oxidized PDMS surfaces is also known to be influenced by the storage condition [46].

1.4 Aims and objectives

Spinal cord injury (SCI) has been shown to result in devastating consequences including temporary or permanent deficit in sensory as well as motor function. The regeneration of nerve after SCI is found to be a chaotic process due to unorganized axon alignment which is accompanied with limited remyelination. Therefore, in order to persuade sufficient regenerated axons to bridge the lesion site, properly organized axonal alignment is necessary. Furthermore demyelination after SCI strongly impairs the conductive capacity of surviving axons, remyelination is critical for proper function of the regenerated nerves. Schwann cells (SCs) migration is the key in axon regeneration and remyelination, as SCs are responsible for remyelination of the regenerated axons and provide guidance for regenerating axons. The goal of this doctoral work focuses on designing and characterizing engineering approaches to enhance both axon regeneration and SC migration. Therefore, this dissertation involves two main objectives: 1) design of a pre-stretch induced anisotropic surface to enhance axon alignment and myelination, and 2) developing a micropatterned channel system to promote SC migration.

1.4.1 Design of pre-stretch induced anisotropic surface

Chapter 2 outlines the methods of fabricating a pre-stretched substrate for cell culture and explores the effect of pre-stretch induced surface anisotropy on cell orientation. Mechanical cues in the cellular environment play important roles in guiding various cell behaviors, such as cell alignment, migration, and differentiation. Previous studies investigated mechanical stretch guided cell alignment predominantly with cyclic stretching whereby an external force is applied to stretch the substrate dynamically (i.e. cyclically) while the cells are attached onto the substrate. In contrast, in this chapter we created a static pre-stretched anisotropic surface in which the cells

were seeded subsequent to stretching the substrate, and quantified the extent of pre-stretch induced anisotropy and predicted the effective stiffness in the stretch direction as well as its perpendicular direction. We showed mesenchymal stem cells (MSC) aligned in the pre-stretched direction, and the cell alignment and morphology were dependent on the pre-stretch magnitude. In addition, the pre-stretched surface demonstrated an ability to promote early myoblast differentiation of the MSC. The cell orientation induced by the pre-stretch induced anisotropy provided insight into nerve tissue engineering applications for enhancing axon alignment in the absence of dynamic mechanical stimuli.

Based on the preliminary results from Chapter 2, Chapter 3 further investigates the impact of pre-stretch induced surface anisotropy on axon growth. In this chapter, we demonstrate that static pre-stretch induced anisotropy promotes dorsal root ganglion (DRG) neurons to extend thicker axon aggregates along the stretched direction and form aligned fascicular-like axon tracts. Moreover, Schwann cells, when co-cultured with DRG neurons on the pre-stretched surface co-localized with the aligned axons and expressed P0 protein, are indicative of myelination of the aligned axons, thereby demonstrating that pre-stretch induced surface anisotropy is beneficial in enhancing axon alignment, growth, and myelination.

1.4.2 Design of micropatterned channels for SC migration

Schwann cell migration is important for both spinal cord and peripheral nerve injuries, as Schwann cells are responsible for remyelinating the regenerated axons as well as providing guidance for regrowing axons. However, although numerous studies have focused on designing transplantable scaffolds for bridging the damaged nerve, few have taken into consideration the

migration of Schwann cells required for remyelination. Chapter 4 focuses on Schwann Cells migration on patterned PDMS microgrooved surface, studying the influence of channel diameter migration behavior of large populations of Schwann cells. Micropatterned polydimethylsiloxane (PDMS) channel surfaces with different channel sizes (50μm, 100μm, and 150µm) were prepared through photolithography, which served to mimic the varying channel sizes of transplantable scaffolds in vitro. Schwann cells were seeded onto PDMS substrates and monitored daily for cell migration. The average cell migration speeds were quantified and normalized. The experimental results support higher Schwann cell migration speeds on PDMS channels with decreasing channel sizes, which was most prominent in the 50µm channels with migration speeds of 2.3 times greater than on the 150µm channels. In conclusion, the data provided in Chapter 4 suggest that Schwann cell migration into the scaffold, required for nerve repair, could be manipulated by controlling the scaffold channel size. Finally to test the axon growth in 3D channels, in Chapter 5 we further co-cultured DRGs and SCs at opposite ends of micropatterned channels of varying sizes (50µm, 100µm, and 150µm). Freshly isolated DRGs were seeded at one end of the channels and SCs were seeded at the other end to provide growth factors to the axons. As a positive control, in lieu of SCs, collagen gel pre-loaded with Nerve Growth Factor (NGF) was added at one end of the channels which provided growth factors. As a negative control, the one end of channels, previously seeded with SCs or coated with NGFcontaining collagen gel, was left blank. The results indicate that the addition of SCs or the NGF encapsulated gel effectively attracted axons to penetrate into the microchannels as compared to the negative control, therefore providing promising insight into design of transplantable scaffold for nerve repair.

1.5 Conclusions and future work

Lastly, chapter 6 defines the significance of these works and their impact within the clinical setting, as well as the future direction of this technology. Specially, the collagen gel filled three dimensional microchannel scaffold is proposed to further study the axon penetration and SC migration. In addition, a schematic design of pre-stretched anisotropic channel scaffold is proposed for both *in vitro* optimization and *in vivo* transplantation.

Chapter 6 also outlines the applicability of the Layer-by-Layer technology on transplantable scaffold design. Due to their technological ease and flexibility in structure and components, layer-by-layer (LbL) technology could provide functional coatings that possess adhesive properties, axon guidance and control drug release capabilities. These advantages enable LbL self-assembled films to be integrated into transplantable scaffolds to provide a robust and versatile platform for promoting cell adhesion and delivering drugs for SCI repair.

CHAPTER 2 EFFECT OF STATIC PRE-STRETCH INDUCED SURFACE ANISOTROPY ON ORIENTATION OF MESENCHYMAL STEM CELLS

2.1 Introduction

While chemical stimuli have long been understood to regulate cell behavior, in recent decades mechanical stimuli have gained increasing attention in tissue engineering. Engineers are able to induce various changes in both morphology and intracellular signaling by manipulating the mechanical environment of the cell. For example, mechanical stretching can regulate cell behavior through the induction of cell orientation, remodeling of the cytoskeletal fibers, and changes in cell signaling [47-49]. When subjected to an external stretch, stem cells have been found to align in a specific direction with certain protein synthesis up-regulated, showing promising differentiation potential [50-51]. Uniaxial cyclic stretching has been shown to direct cell orientation perpendicular to the stretching direction [52-54]. However, compared to the large body of research focused on cyclic stretching, few studies have examined the effects of static stretch on cell orientation and morphology. Collinsworth et al. [55] found that after applying static stretch, the originally randomly oriented mammalian skeletal muscle cells showed clear alignment in the direction of static stretch. In contrast, Goli-Malekabadi et al. [52] recently claimed that with MSCs static stretch is not as influential as cyclic stretching in directing cell alignment or changing cell morphology.

While the alignment of cells on a statically stretched substrate is intuitive, the mechanism by which the cells sense the stretch is not easily understood. That is due in part to the confusion that arises from the preponderance of research where static stretching meant the cells are seeded first to ensure attachment prior to applying an external stretch. As a result, any change in the cell

orientation after the stretch was attributed to adaption to the sudden change followed by a slow recovery. In other words, the so-called static stretch in those prior studies is actually a one-time dynamic stretch without repetition. To address this issue, we undertook this study to create a purely statically stretched environment by seeding cells on a pre-stretched membrane. The major difference between our static pre-stretch and previous static stretch studies is that we applied the stretch prior to seeding the cells, and attributed the cell alignment to the pre-stretch induced anisotropy. A prior study by Haston et al. [56] used a similar procedure to ours; however they attributed their results to the topography induced by the fibrous collagen on the surface. In contrast, in our study the surface was coated with poly-L-lysine (PLL), which is not a fibrous matrix, and cell alignment was produced primarily as a result of the mechanical pre-stretch. We then proposed that cells behave actively by pulling the substrate to sense the mechanical environments and respond to the environmental condition by modulating their morphology and orientation after seeding, which can be predicted by using the theory of finite elasticity.

We have previously applied an "active mechano-sensing" model to show that the size of a cell depends not only on the mechanical properties of the substrate, but also on the energy consumption during active cellular probing [57]. Following an investigation of cell alignment on anisotropic surface generated by fixed and free boundaries (unpublished data), the experimental results agreed with our "cell active mechano-sensing" model which suggests that the cells can feel and respond to the surface anisotropy by orienting in the direction of maximal effective stiffness (unpublished data). In this study, we applied this concept on a static pre-stretched (previously stretched) poly-dimethyl-siloxane (PDMS) membrane. By culturing the cells on the pre-stretched PDMS membrane, the effective stiffness the cells experienced in the stretched

direction was significantly larger than that in the un-stretched direction. This increase of the effective stiffness results in the cells orienting in the stretched direction as well as modulating the cytoskeleton and focal adhesion.

This stretch-induced directional difference can be explained using Figure 2.1. Let the rectangular body on the far left of the figure be an isotropic material in the stress-free configuration. Let us first stretch this material in the vertical direction and deform it with a load F⁰ on a square shape, which we denote as the "pre-stretched configuration". From the pre-stretched state, if we deform it equi-biaxially (same deformation in both directions) then, in addition to the original loading F^0 , we have to apply F¹ and F² in the vertical and horizontal directions, respectively. Now we will find that F¹ should be larger than F² in order to achieve the same deformation in both directions from the pre-stretched state, because the material will be stiffer in the vertical direction due to the prior deformation. Similarly, if F¹ and F² are the same, then the deformation in the vertical direction would be smaller than in the horizontal direction. Thus, when a cell is cultured on a pre-stretched substrate, F⁰ can be considered as the force holding the substrate in this intermediate or pre-stretched state, F1 and F2 are traction forces applied by the cell, and the deformation from this pre-stretched substrate are the forces that the cell senses. We will denote this anisotropic response of the cells to the pre-stretched substrate under active cellular probing as "stretch-induced anisotropy". We propose, hence, that stretch is a natural mechanism to induce an anisotropic environment in the substrate for guiding cell morphology and functions. We should note that this stretch-induced stiffening arises from the change of the reference configuration for the strain measurement, which is different from a nonlinear material response called strain-hardening. We cannot capture this stiffening by linear elasticity because it uses only

one unchanged reference configuration to measure the strain. Instead, the theory of small deformation superimposed on large (often called "theory of small on large") based on finite elasticity enables us to accurately estimate the degree of anisotropy by measuring the pre-stretch of the substrate [58].

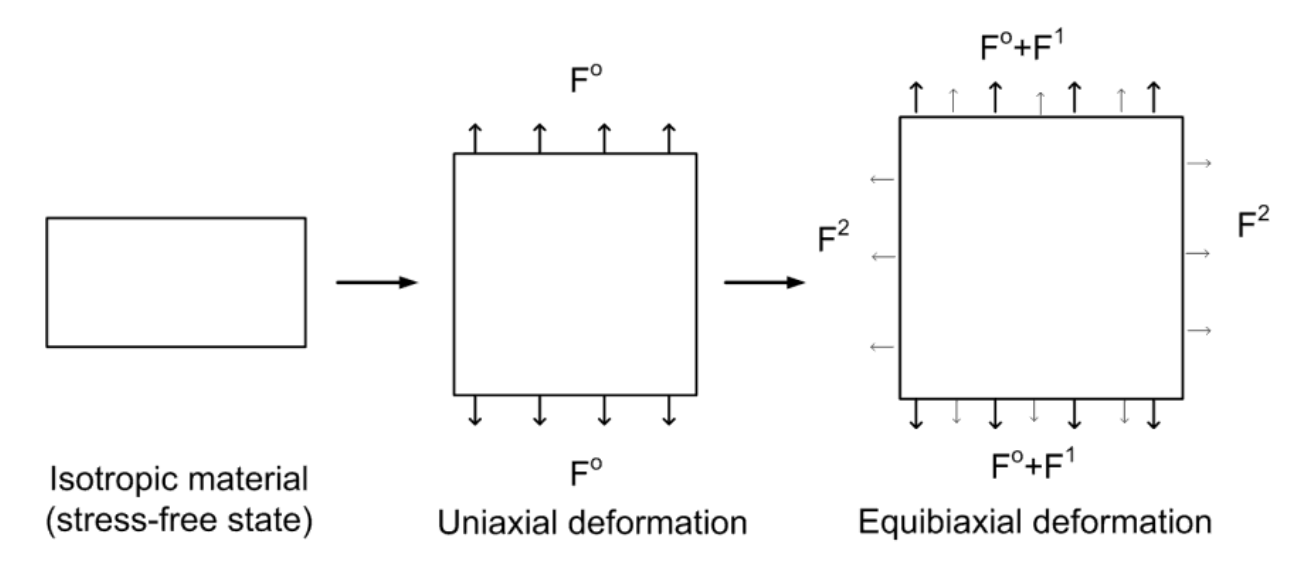


Figure 2.1. Schematic illustrating stretch induced anisotropy.

The cells experience a stiffer surface in the direction of stretch and this stretch-induced anisotropic cellular response on an isotropic substrate can be explained with a simple two-step deformation model (see text for details).

In the present study, we predict the anisotropy induced by the theory and found that the distribution of cell alignment is in the stretch direction; therefore we interpret the cell alignment as the resistance to active cellular pulling. We employ the concept of active cellular mechanosensing, and present a method that uses mechanical quantities (i.e. linearized stiffness) which can be obtained from the mechanical analysis. Specifically, we theorize that cells actively pull on the substrate and sense the mechanical resistance of the substrate, i.e., the deformation upon active probing, and the cells thereby align in the direction of highest resistance upon active pulling.

Based on our previous study [57], we define an effective stiffness of the substrate that correlates with the stiffness that the cells sense. For the experiments, we created surface anisotropy with a uniaxially sustained stretching of the PDMS substrate and cultured MSCs on the pre-stretched substrate. The distributions of the orientation of the cells during culture were quantified and the surface properties were examined on surfaces with and without pre-stretch. The impact of the magnitude of the pre-stretch on cell orientation and morphology were evaluated. We demonstrate that the effective stiffness can be estimated using conventional finite elasticity analysis, and predict the cellular orientations that were experimentally confirmed. In addition, the pre-stretched not only affects MSC morphology but also promotes early myoblast differentiation of the MSC.

2.2 Materials and methods

2.2.1 Materials

The poly-(dimethylsiloxane) (PDMS) substrate was prepared using the 184 silicone elastomer kit purchased from Dow Corning (Midland, MI). FlexiPERM ConA Silicone chamber was purchased from Greiner bio-one (Monroe, NC). Dulbecco's modified Eagle medium (DMEM), fetal bovine serum (FBS), penicillin, streptomycin, 0.25% trypsin-EDTA, 1X-phosphate buffered saline (PBS) and immunostaining components (mouse anti- vinculin antibody, Alexa Fluor 488 goat anti-mouse IgG secondary antibody, Texas Red-X phalloidin, and DAPI) were purchased from Invitrogen (Carlsbad, CA). Bovine Serum Albumin (BSA) was purchased from US Biological (Marblehead, MA). Cultrex® Poly-L-Lysine was purchased from Trevigen (Gaithersburg, MD). Fibronectin was purchased from Sigma- Aldrich (St. Louis). MyoD primary antibody (Santa Cruz) was kindly provided by Dr. Bruce D. Uhal at Michigan State University.

2.2.2 PDMS substrate preparation

The PDMS substrate was cured in polystyrene tissue culture dish by mixing a 35:1 solution of base and curing agent and pouring the mixture into the dish with a thickness of 1mm. The mixture was kept under vacuum for 20 minutes to remove air bubbles, prior to curing overnight at 60 °C. The PDMS surface was further cleaned with a PX-250 plasma cleaning/etching system (March Instruments) for 3 minutes at 165 mTorr and 65 sccm flow of O₂. A piece of rectangle membrane (5cm×3.5cm) was then stretched evenly with 10%, 20%, and 30% elongation in the longer axis and fixed on top of a plastic slide with a 1 inch diameter hole in the center. This was followed by placing a silicone chamber on top of the membrane. The silicone chamber without a bottom provides a circular well to hold the cell medium and at the same time enable a separate, flat PDMS membrane at the bottom (on which the cells are to be attached) to be pre-stretched. The entire device design is shown in Figure 2.2. Before seeding the cells, 1.5ml PLL was added to the chamber and incubated for 20 minutes to enhance cell attachment. Alternatively, fibronectin (1 µg/ml) was added to the chamber and incubated for 2 hours to enhance cell attachment.

2.2.3 PDMS surface characterization

The surface topography was analyzed by scanning electron microscope (JSM-7500F cold field emission SEM, JEOL Corporation) in secondary electron imaging mode. An acceleration voltage of 12kV was used for all experiments. Images were taken at a magnification of 3000X.

2.2.4 Cell culture

All procedures for cell isolation were approved by the Institutional Animal Care and Use Committee at Michigan State University.

Bone marrow mesenchymal stem cells (MSCs) were isolated from 6-8 week old Sprague-Dawley female rats. In brief, femurs and tibias from a 6-8 week old rat were dissected and both ends were cut off. The marrow was flushed using a needle and syringe. The cell suspension was then filtered through a 65μm nylon mesh to remove bone debris and blood aggregates. Cells were cultured in DMEM with 10% FBS, 100 μg/ml streptomycin and 100U/ml penicillin added, and placed in the incubator with a humidified atmosphere containing 5% CO₂ at 37 °C. The medium was replaced every 3 to 4 days until the cells reached 80%-90% confluence. Confluent cells were detached using 0.25% trypsin-EDTA and plated at a density of 20,000 cells per mL with 2 mL added to the chamber.

2.2.5 Quantification of cell orientation distribution and cell length

Phase contrast images were collected with Leica DM IL inverted microscope (Bannockburn, IL) equipped with SPOT RT color camera (Diagnostics Instruments, MI) using 10X objective. Image-Pro Plus Version 4.5 was used to measure the cell orientation angles. Briefly, a straight line was drawn perpendicular to the stretch direction which was used as the reference to indicate zero degree orientation. For each cell, the cell orientation was measured by drawing a straight line through the longest axis of the cell body, and the angle between the cell axis and the reference line was automatically given by the software and recorded for further analysis. All experiments were repeated at least three times for statistical verification. For the stretched vs.

unstretched comparison, the cells seeded on the stretched and unstretched membranes were from passages 12 to 16. For each experiment, we took 4 images in each stretch chamber everyday and quantified the cell orientation angles. Since the cells proliferated quickly, from 100 cells in 4 images on the first day to about 800 cells total on the fourth day, we normalized the cell number at each ten degrees of orientation to the total number of cells on that day. Two-sample Kolmogorov-Smirnov test were applied to evaluate the statistical significance. For the stretch magnitude analysis, we quantified the number of cells oriented at different angles (90 °represents parallel to the stretch direction) for each 10 ° on 10%, 20%, and 30% pre-stretched surfaces as compared with the unstretched (control) surface. We counted the number of cells in the parallel orientation (90 °±10 °angle) which was normalized to the total number of cells on each surface. The parallel orientation ratios were reported by the mean value and standard deviation. The cell length was measured using Image-Pro Plus by drawing a straight line through the longest axis of cell body starting from one end to the other end.

2.2.6 Immunocytoche mistry

Immunocytochemistry was performed at room temperature on cells seeded on the stretched surface for 6 days. Cells were rinsed with PBS, followed by fixation with 4.0% paraformaldehyde in PBS for 15 min, rinsed 3 times in PBS, then permeabilized with 0.1% Triton X-100 in PBS for 15 min and washed 3 times with PBS. After washing, cells were blocked in 1% BSA for 30 minutes. After BSA blocking, the cells were incubated with Texas Red-X phalloidin (5µl stock per 200µl of 1% BSA solution) for 20 minutes to visualize actin filaments, and then incubated with mouse anti-vinculin primary antibody (1:400 dilution in 1% BSA solution) or rabbit anti-MyoD primary antibody (1:200 dilution in 1% BSA solution) for 1

hour followed by three washes in 1X PBS, and then incubated with Alexa Fluor 488 goat antimouse or anti-rabbit IgG secondary antibody (1:500 dilution in 1% BSA solution) for 1 hour. Cells were washed again, three times in 1X PBS and then incubated for 5 minutes in 300nM DAPI to visualize the nucleus. The PDMS substrates were air dried and the silicone chamber was removed from the membrane, the stained PDMS membrane was finally kept in the dark to cure for 24 hours at room temperature. Confocal laser scanning microscopy (CLSM) images were obtained with Olympus FluoView1000 laser scanning confocal microscope using 60X oil, 40X oil and 10X objectives. Fluorescence intensity analysis was performed using software FluoView1000. Briefly, fluorescence images were taken using confocal microscopy. Each cell on the images was traced and the average cell intensity was measured automatically. The average intensity of each image was then calculated automatically by the software and the average intensity of 4 images was then calculated using Excel. For each condition, three samples were measured and the standard deviation and p-value were analyzed.

2.2.7 Statistical analyses

Data were expressed as the mean \pm standard deviation of the mean. ANOVA-Tukey's test was applied to assess for a significant difference in Figures 2.9 and 2.10h, Two-sample student t-Test was used to determine statistical significance for Figure 2.11e. The two-sample Kolmogorov-Smirnov test was applied to evaluate the statistical significance for Figure 2.8 and Figure 2.12. In all cases, a p value of < 0.05 was considered statistically significant.

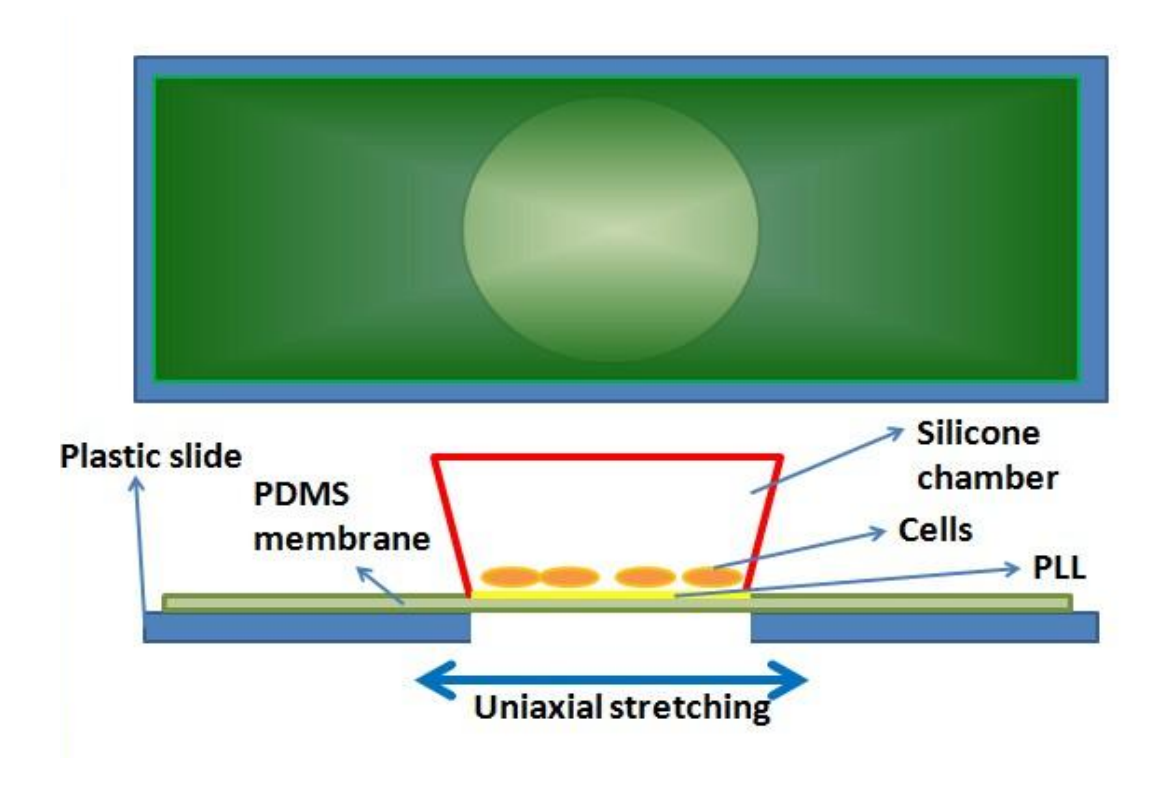


Figure 2.2. Design of static pre-stretching device

2.3 Estimation of stretch-induced anisotropy

2.3.1 Estimation of pre-stretch-induced anisotropy of the substrate in active cellular sensing: small on large theory

The deformation of the substrate can be divided into two parts: large deformation during prestretch and small deformation due to cell traction (Figure 2.3). A pre-stretch was applied before the cells were cultured on the substrate to induce anisotropy of the substrate prior to active cellular sensing/probing. The finite elastic behavior of the substrate was characterized by performing uniaxial tests of the substrate, and the effective stiffness and degree of anisotropy during cellular traction were calculated using the theory of small on large [58], which allowed us to accurately estimate the structural stiffening due to the pre-stretch (i.e., change in reference length for strain measurement) as well as the material stiffening (i.e., change of the slope in

stress-strain curve of Figure 2.4). The effective stiffness and degree of anisotropy represent the substrate responses sensed by the cells during active probing (i.e., small deformation).

2.3.2 Characterization of finite elastic behavior of the substrate

The mechanical properties of the substrate (i.e. PDMS membrane) were measured by the uniaxial tensile test, and the mechanical behavior was described by the incompressible, isotropic neo-Hookean model. Figure 2.4 shows the engineering stress of the PDMS membrane with respect to the change in the engineering strain obtained from the experimental data (dots) and a theoretical fit (solid line) using the neo-Hookean model.

The deformation gradient of the substrate during uniaxial deformation can be obtained from $\mathbf{F} = \operatorname{diag}\left[\lambda_1, \frac{1}{\sqrt{\lambda_1}}, \frac{1}{\sqrt{\lambda_1}}\right]$. From the classic theory of invariants, the strain energy density of an isotropic material is given by $W=(I_{\mathbf{C}},\ II_{\mathbf{C}},\ III_{\mathbf{C}})$, where $I_{\mathbf{C}}=\operatorname{tr}\mathbf{C}$, $II_{\mathbf{C}}=\frac{1}{2}\{(\operatorname{tr}\mathbf{C})^2-\operatorname{tr}(\mathbf{C}^2)\}$, $III_{\mathbf{C}}=\det\mathbf{C}$ for $\mathbf{C}=\mathbf{F}^T\mathbf{F}$. The constitutive relation between the stress and strain is then given by $\boldsymbol{\sigma}=-p\mathbf{I}+2\mathbf{F}\left(\frac{\partial W}{\partial c}\right)\mathbf{F}^T$, where $\boldsymbol{\sigma}$ is the Cauchy stress tensor and p is a Lagrange multiplier. Our preliminary study showed that the finite elastic behavior of a PDMS substrate could be described well with a neo-Hookean function, $W=\frac{c}{2}(I_{\mathbf{C}}-3)$ with a material parameter c (Figure 2.4). The substrate was tested with the uniaxial tensile tester, and the material parameter determined by a nonlinear parameter estimation technique. See previous study [59] for details on the parameter estimation using a finite elastic constitutive model.

2.3.3 Estimation of stretch induced anisotropic response of substrate in active sensing

In the theory of linear elasticity, the relationship between stress and strain is linear, and the stress induced by two-step loading is expressed by the sum of each stress (i.e., $\sigma = \mathbf{E}(\mathbf{\epsilon}^0 + \mathbf{\epsilon}) = \sigma^0 + \mathbf{E}\mathbf{\epsilon}$, where σ , ε , and \mathbf{E} are stress, strain, and fourth-order elasticity tensor, respectively, and the superscript '0' represents the pre-stress values). However, this superposition principle is not valid when the pre-stress σ^0 is induced by finite deformation, because the reference configuration of the second strain part ε is significantly different from the stress-free state which is the reference for the first strain part ε^0 . In this case, the stress-strain relationship could be derived from the finite elasticity theory (theory of small on large) and the incremental stress during small deformation is written as $\mathbf{\sigma} - \mathbf{\sigma}^0 = \hat{\mathbf{E}} \boldsymbol{\varepsilon}'$, where $\boldsymbol{\varepsilon}'$ is the strain measured from the prestretched state, and the stiffness obtained with respect to the pre-stretched state is, in index notation [58, 60], $\hat{E}_{ijkl} = \delta_{ik}\delta_{pl}\hat{\sigma}_{pj}^0 + \delta_{jk}\delta_{pl}\hat{\sigma}_{ip}^0 + E_{ijkl}$, where E_{ijkl} is the fourth-order tensor evaluated from the strain energy function at $\mathbf{\epsilon}^0$, δ_{ik} is the Kronecker delta, and $\hat{\mathbf{\sigma}}^0 = \mathbf{\sigma}^0 + p\mathbf{I}$. Since the cells were cultured on the stretched substrate and did not experience the pre-stretch, the strain induced during active cellular probing $(\sigma - \sigma^0)$ is estimated by ε' , and the stiffness that the cells sense is represented by the stiffness of pre-stretched substrate, $\hat{\mathbf{E}}$. As explained above and in previous studies [58, 60], the Ê depends on not only the material stiffness (i.e., tangent of stress-strain curve) but also on the pre-stress σ^0 at ε^0 . These two components are calculated from the finite deformation of the PDMS membrane and the mechanical properties using the uniaxial test. The stretch-induced anisotropy of the PDMS membrane is then represented by the ratio of effective stiffness in the stretched direction to its perpendicular direction $(\hat{E}_{1111}/\hat{E}_{2222})$. Figure 2.5 shows the change in effective stiffness in both directions with respect to the change in

strain. When there is no pre-stretch, $\hat{E}_{1111} = \hat{E}_{2222} = 268 \, kPa$, which equals the elastic modulus of the material (35:1 crosslinked PDMS membrane). While the stiffness in the stretched direction increases, the stiffness in the perpendicular direction decreases as the PDMS membrane experience more strain during uniaxial stretching. At 10, 20, and 30% of strain of the PDMS membrane, the predicted anisotropy ratio $(\hat{E}_{1111}/\hat{E}_{2222})$ is approximately 1.33, 1.73, and 2.20, respectively. MSCs aligned along the stretched direction on a PDMS membrane (see Figure 3.7) and were supported by the prediction based on the theory of small on large.

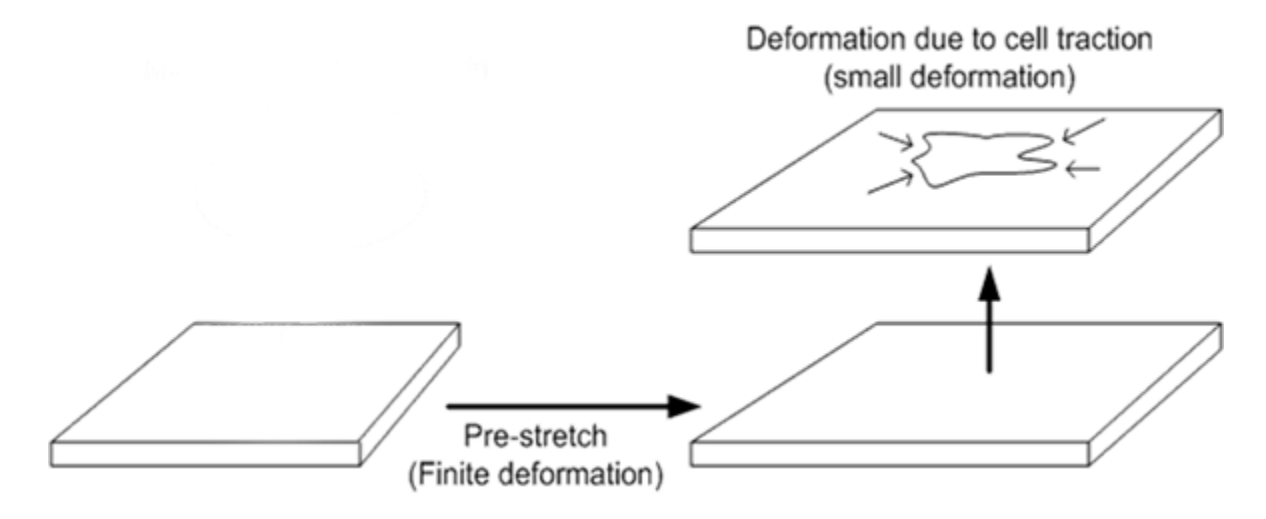


Figure 2.3. Schematic drawing of the two-step deformation of the substrate in the experiment.

For the test, the substrate is stretched in one direction to adjust the effective stiffness and anisotropy prior to culturing the cells. The relationship between the force applied by the cells and deformation of the substrate is then calculated by using the theory of "small on large".

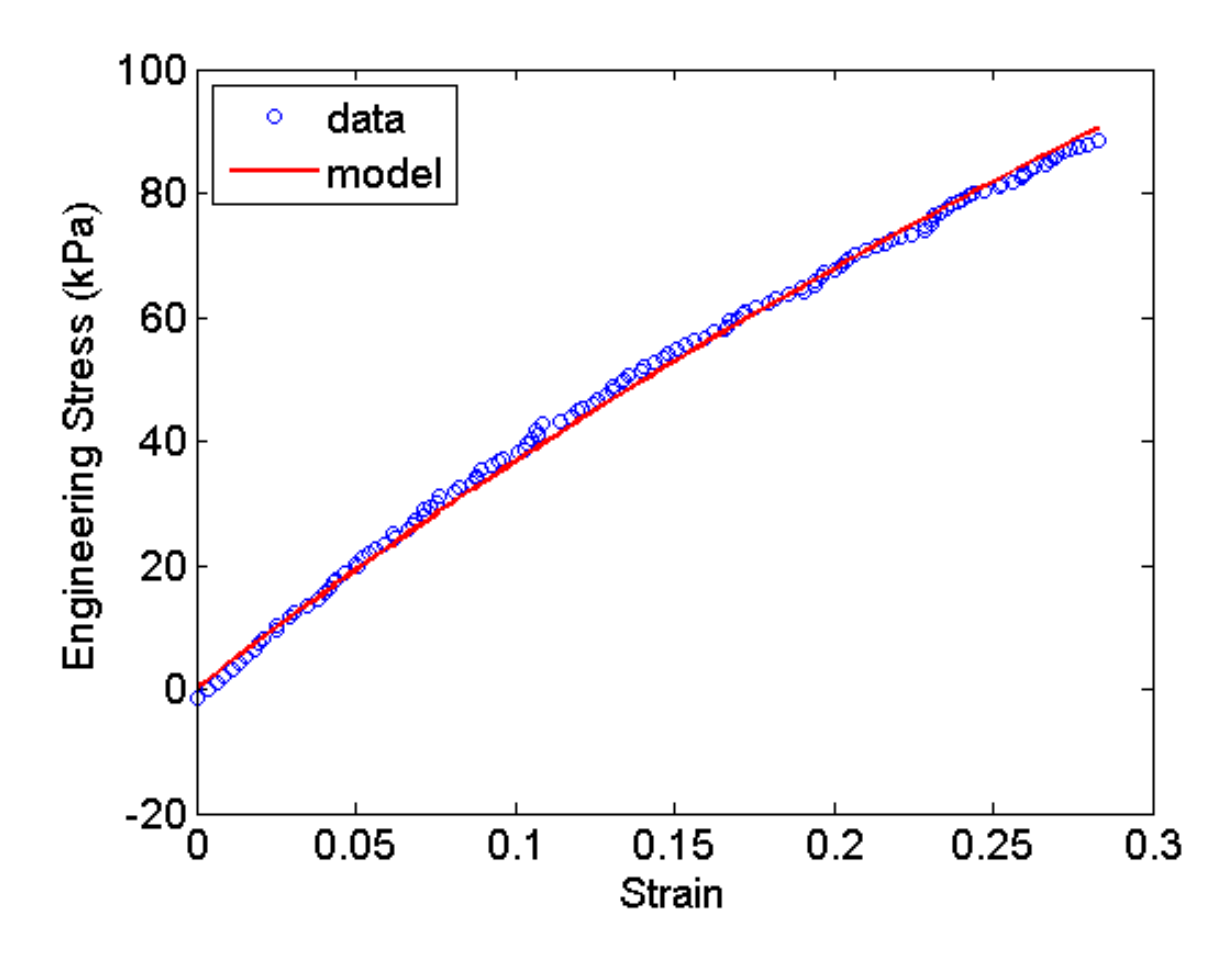


Figure 2.4. Stress-strain plot.

The plot of the uniaxial test data (dots) of a 35:1 PDMS substrate and the theoretical fit (solid line) using an incompressible neo-Hookean model.

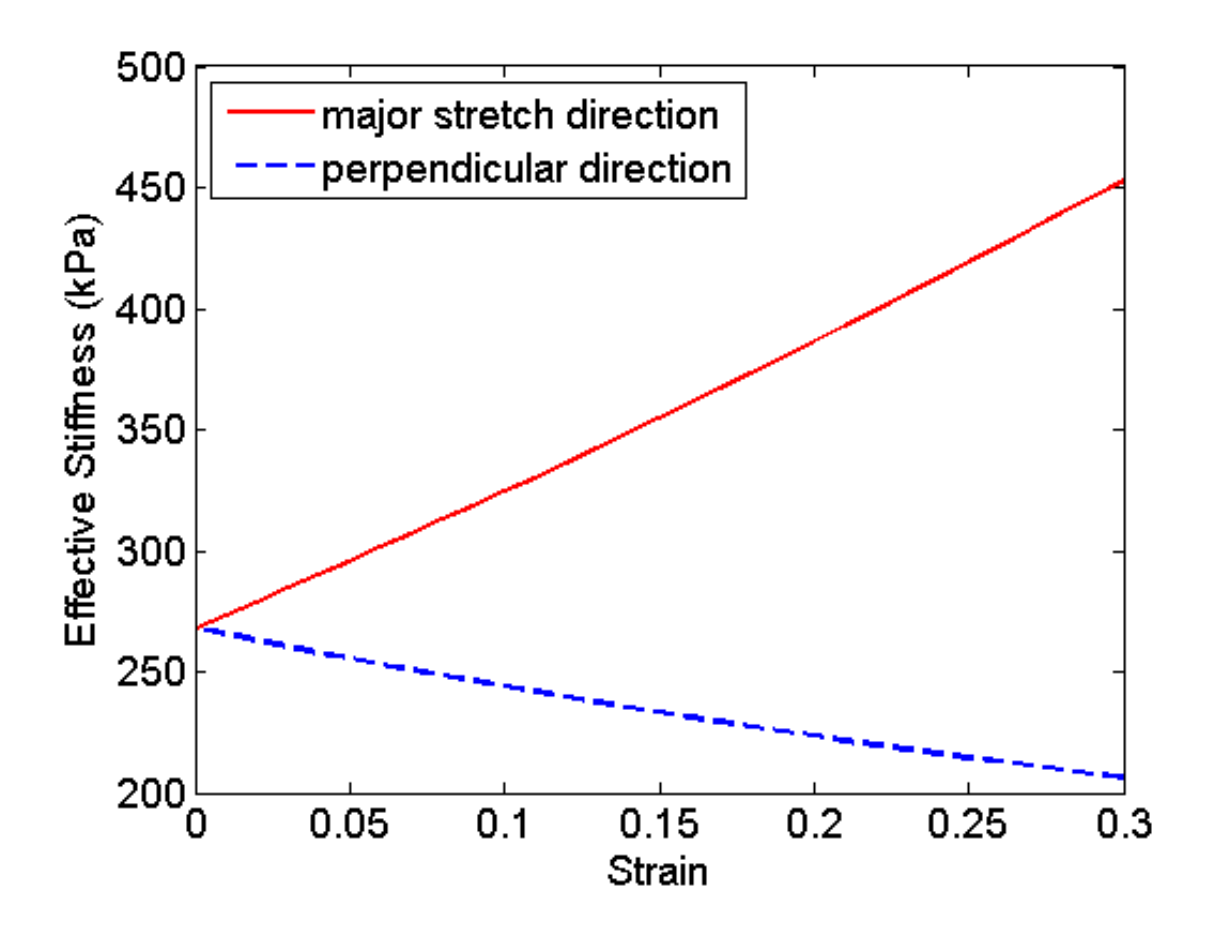


Figure 2.5. Effective stiffness.

An effective stiffness plot in the stretched direction and its perpendicular direction with respect to the change of strain ($\hat{E}_{1111}/\hat{E}_{2222}=1.33$ at 10% strain).

2.4. Experimental results

2.4.1 Surface topography characterization

Images of the surface topography were collected by applying the secondary electron imaging mode in SEM on PLL coated substrates, both unstretched (Figure 2.6a) and stretched (Figure 2.6b). As shown in Figure 2.6, due to the dehydrated imaging condition, the PLL peptides aggregated to be large particles sitting on the surface. However, both surfaces show clear and smooth background without any orienting direction; thereby confirming the cell alignment

(under the medium condition) was not due to contact guidance. Comparing Figure 2.6b with 2.6a, the stretch did not change the surface topography.

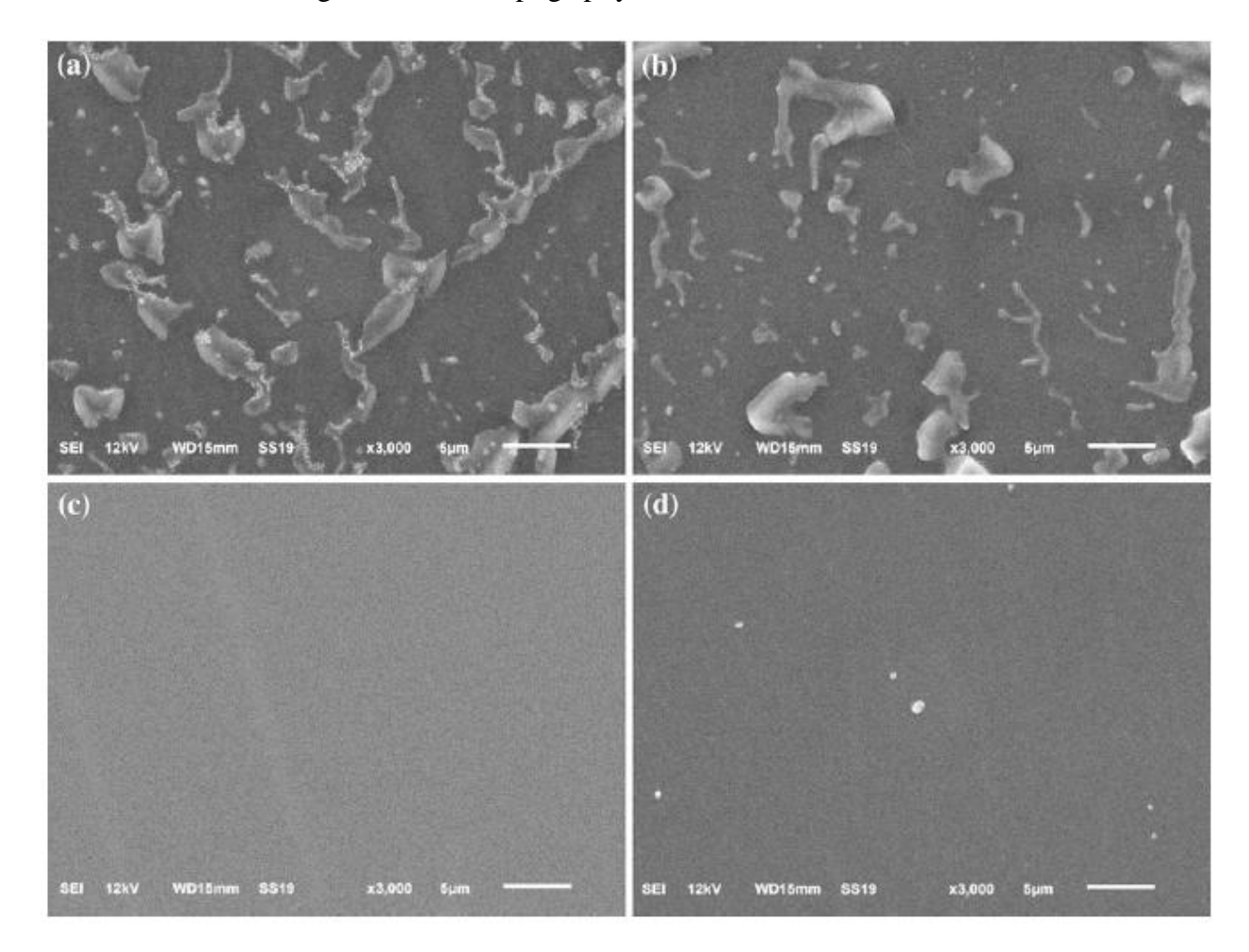


Figure 2.6. Surface topological characterization.

SEM images of the 3D topography of (a) unstretched PLL coated 35:1 PDMS membrane, (b) 10% pre-stretched PLL coated 35:1 PDMS membrane, (c) unstretched 35:1 PDMS membrane without PLL coating, and (d) 10% pre-stretched 35:1 PDMS membrane without PLL coating. The images were taken at a magnification of 3000X.

2.4.2 Orientation quantification

Figure 2.7 shows a comparison of MSC orientation on stretched and unstretched PDMS substrates. Cells orient parallel to the stretched direction (Figure 2.7a), whereas they show random orientation on the unstretched surface (Figure 2.7b). The orientation of the cells changes slightly over time as the cells become confluent, but the general trend remained. The cell orientation was quantified by determining the percentage of cells that aligned at each 10 degree angle during a 4 day culture (Figure 2.8). As shown in Figure 2.8, the pyramid shape of the bar graph is maintained for the stretched substrate. This indicates the cells oriented in the stretch direction and did not change significantly over time while on the unstretched surface the cells oriented more randomly. Two-sample Kolmogorov-Smirnov test applied to evaluate the statistical significance found the distribution of cell orientations on the unstretched samples for day 1, 2, 3 and 4 were statistically different from their respective stretched samples (p < 0.05). The p-values are 2.85E-04 for day 1, 2.85E-04 for day 2, 1.16E-05 for day 3, and 6.12E-05 for day 4.

To further explore the impact of the magnitude of pre-stretch on cell alignment, we evaluated the cell alignment vs. the magnitude of pre-stretch. We quantified the number of cells oriented at different angles (90 °represents parallel to the stretch direction) for each 10 °on 10%, 20%, and 30% pre-stretch surfaces as compared with the unstretched (control) surface. We counted the number of cells in the parallel orientation (90 °±10 °angle) which was normalized to the total number of cells on each surface. The ratio of cells in parallel orientation was determined as the number of cells that orient in the pre-stretched direction (90 °±10 °angle) divided by the total number of cells. We found the ratio of cells that oriented in the parallel direction increased

significantly when the stretch magnitude increased from 10%, 20%, and 30% pre-stretched surfaces as compared with the unstretched (control) surface (Figure 2.9).

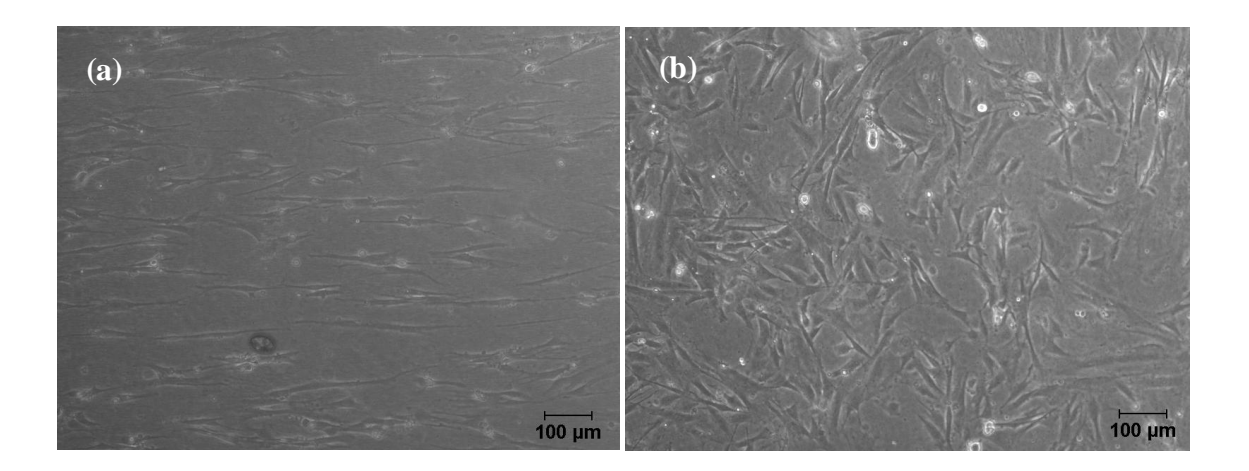


Figure 2.7. MSCs on stretched vs. unstretched PDMS substrate.

Phase contrast (10X) images of MSCs on (a) 10% pre-stretched and (b) unstretched PLL coated 35:1 PDMS membranes after 4 days of culture.

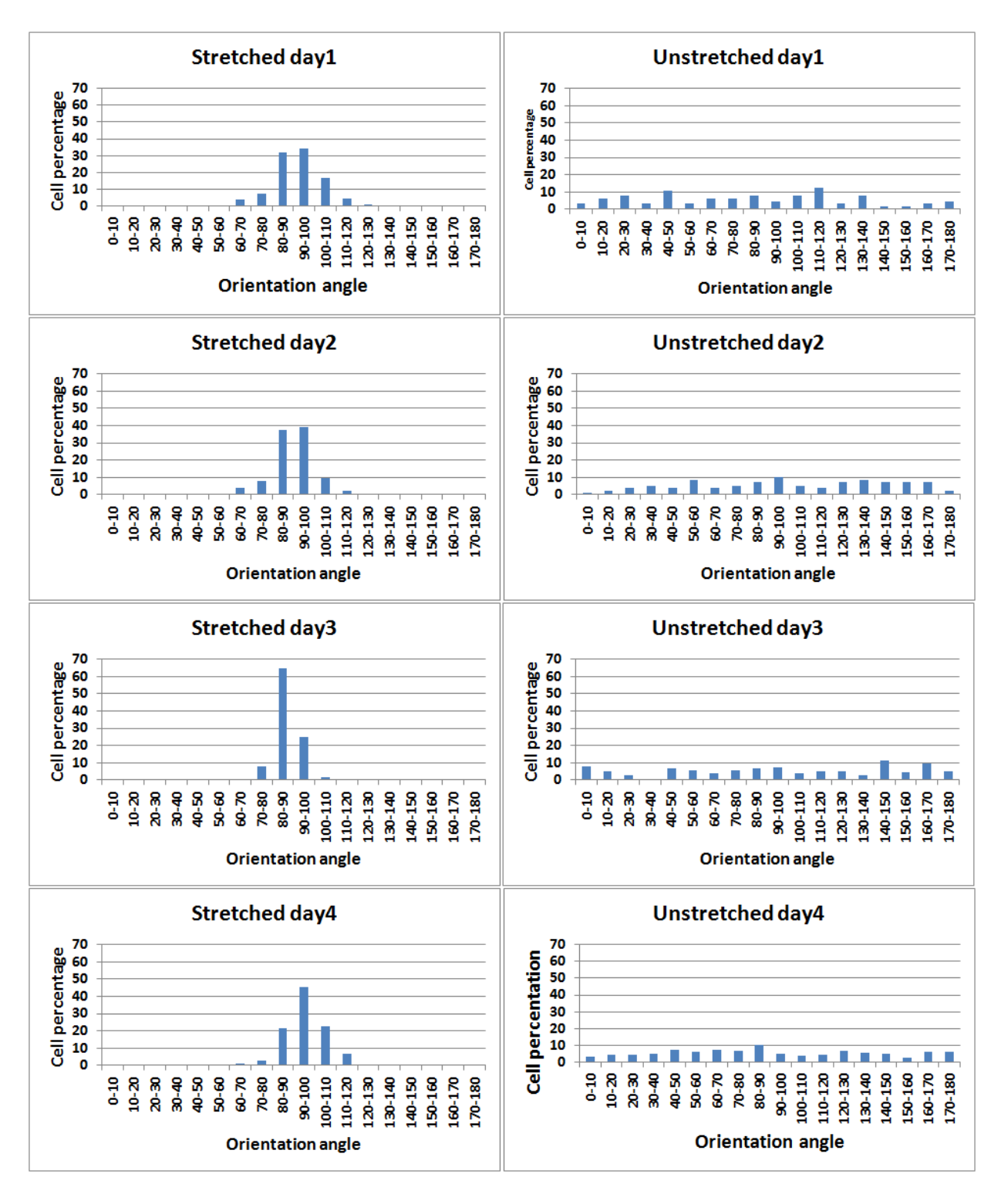


Figure 2.8. Quantification of the orientation angles on stretched vs. unstretched membrane.

The percentage of cells that orient at every 10 degrees. The 90 degree angle represents the direction of pre-stretch. Cell orientation angles were quantified by ImagePro Plus for up to 4

(Figure 2.8 cont'd) days of culture on stretched (left) and unstretched (right) 35:1 PDMS membranes. Two-sample Kolmogorov-Smirnov test were applied to evaluate the statistical significance. The results showed that the unstretched samples for days 1, 2, 3 and 4 have statistically different distributions (p < 0.05) as compared to their respective stretched samples. The p-values are 2.85E-04, 2.85E-04, 1.16E-05, and 6.12E-05 for days 1-4, respectively.

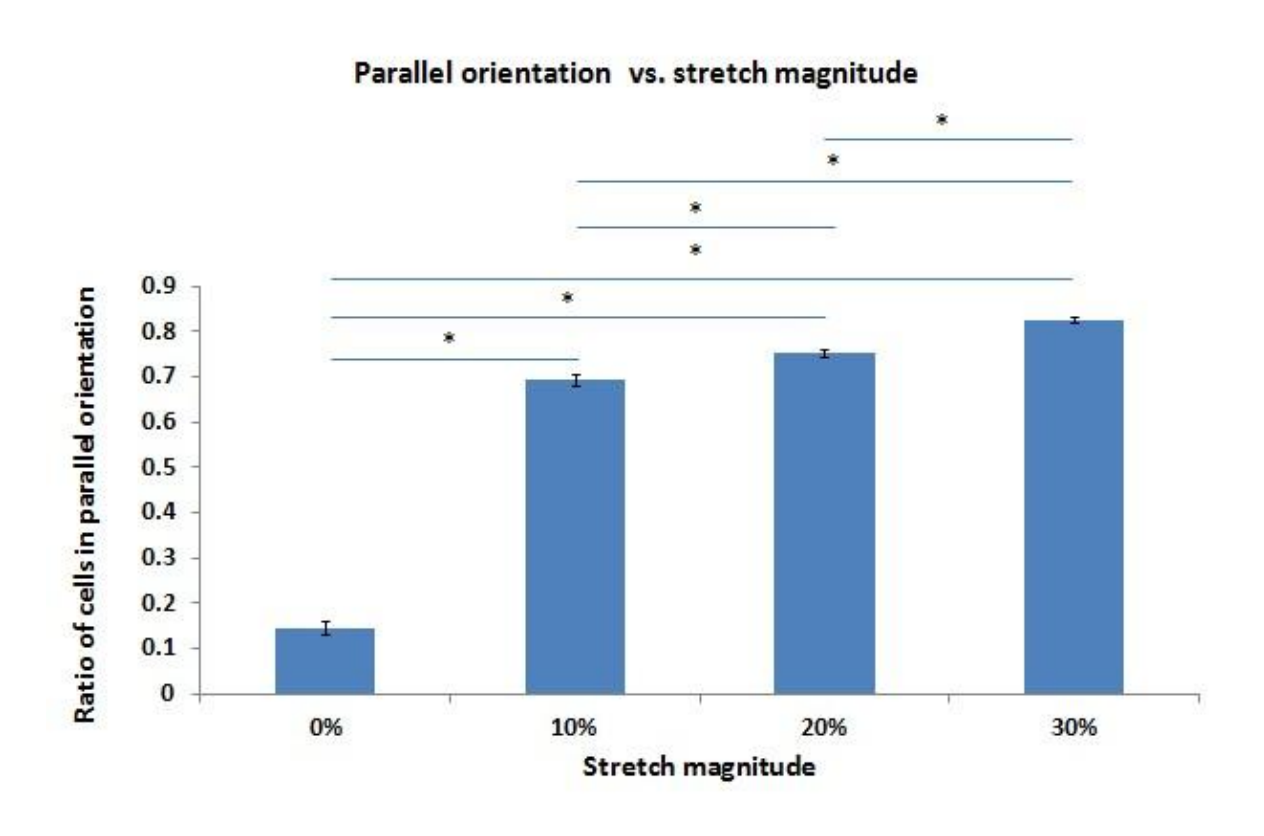


Figure 2.9. Ratios of parallel orientation vs. magnitude of pre-stretch.

The ratio of cells with orientation between 80 °to 100 °angles relative to the total number of cells on the pre-stretch substrate was quantified after 4 days of culture on PLL coated 35:1 PDMS membrane at 0%, 10%, 20% or 30% pre-stretch. The number of cells that aligned parallel to the stretched direction (within±10 °) was normalized to the total number of cells on each surface. (*) > 0% stretch, p value<0.00001; (#) > 10% stretch, p value<0.0001; (\$) >20% stretch, p value<0.0001.

2.4.3 Actin cytoskeleton alignment and cell morphology change

To further confirm the cell orientation on the pre-stretched surface, we stained actin filaments and focal adhesion, which illuminated the cytoskeleton organization. As shown in Figure 2.10a & 2.10c, the actin filaments aligned in the pre-stretch direction on the stretched surface, but aligned randomly on the unstretched surface (2.10b & 2.10d). Similar results were obtained with the focal adhesion staining (Figure 2.10e – 2.10g), where vinculin staining showed clear alignment on the stretched surface. Thus the cytoskeleton also aligned on the pre-stretched surface, which likely resulted in the cell orientation and morphology observed. In addition to alignment, we found the cell morphology changed with the magnitude of pre-stretch. As the magnitude of pre-stretch increased from 0% to 30%, the cell morphology became more elongated and the average cell length increased (Figure 2.10e – 2.10g). The cell length quantification was shown in Figure 2.10h.

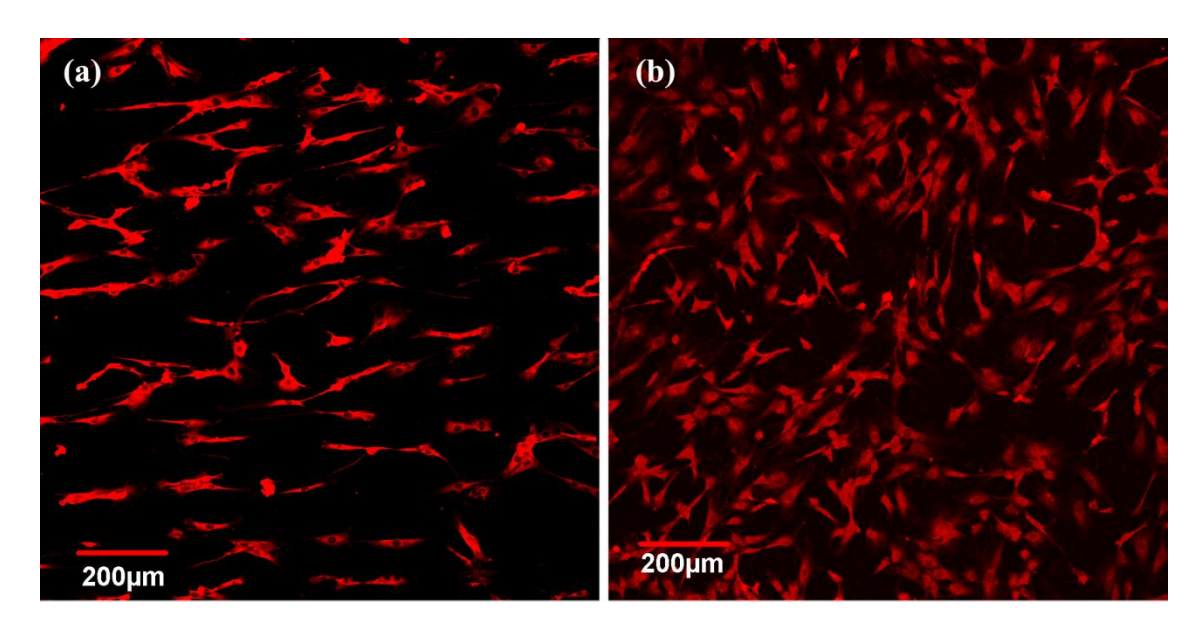
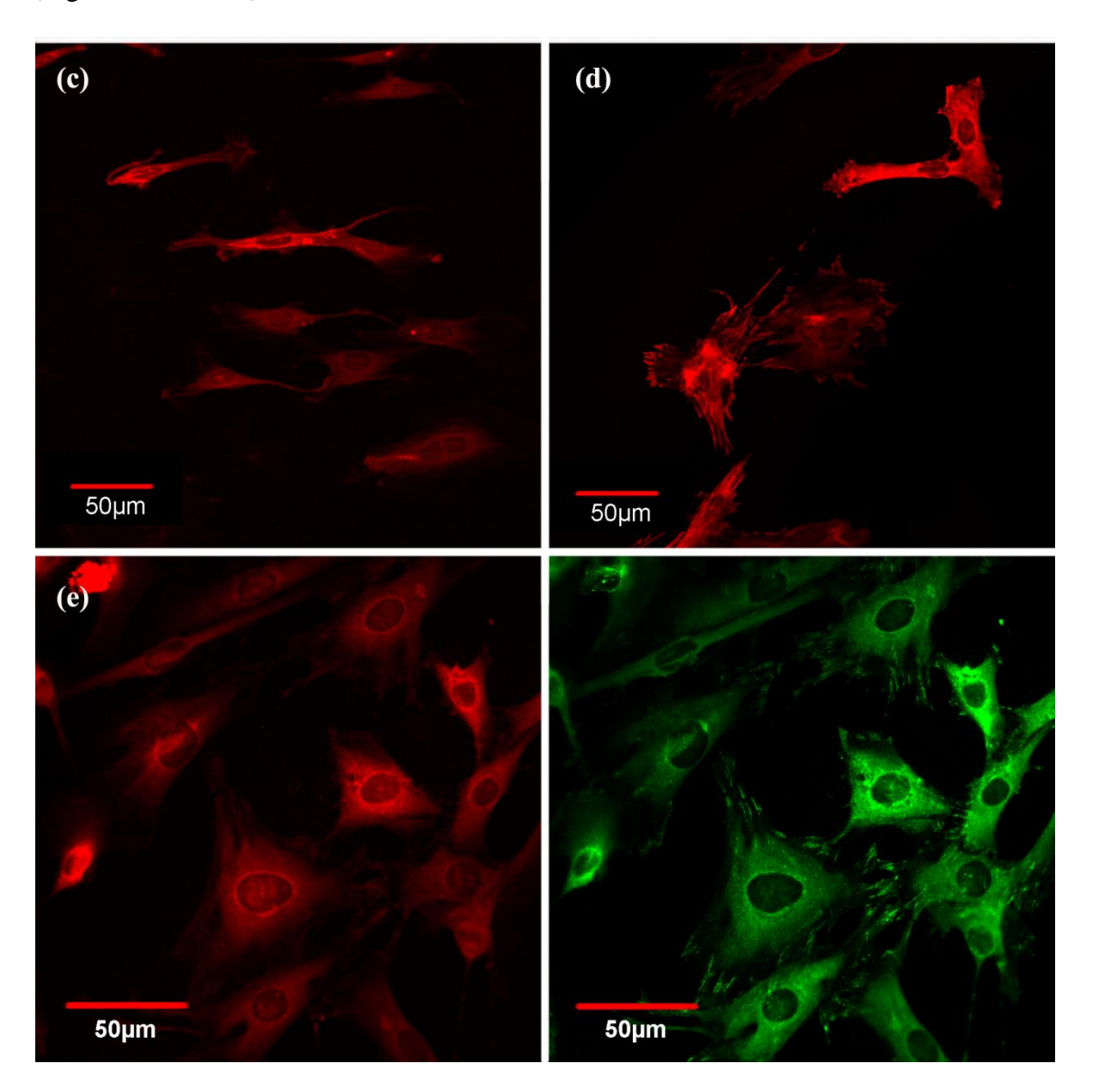


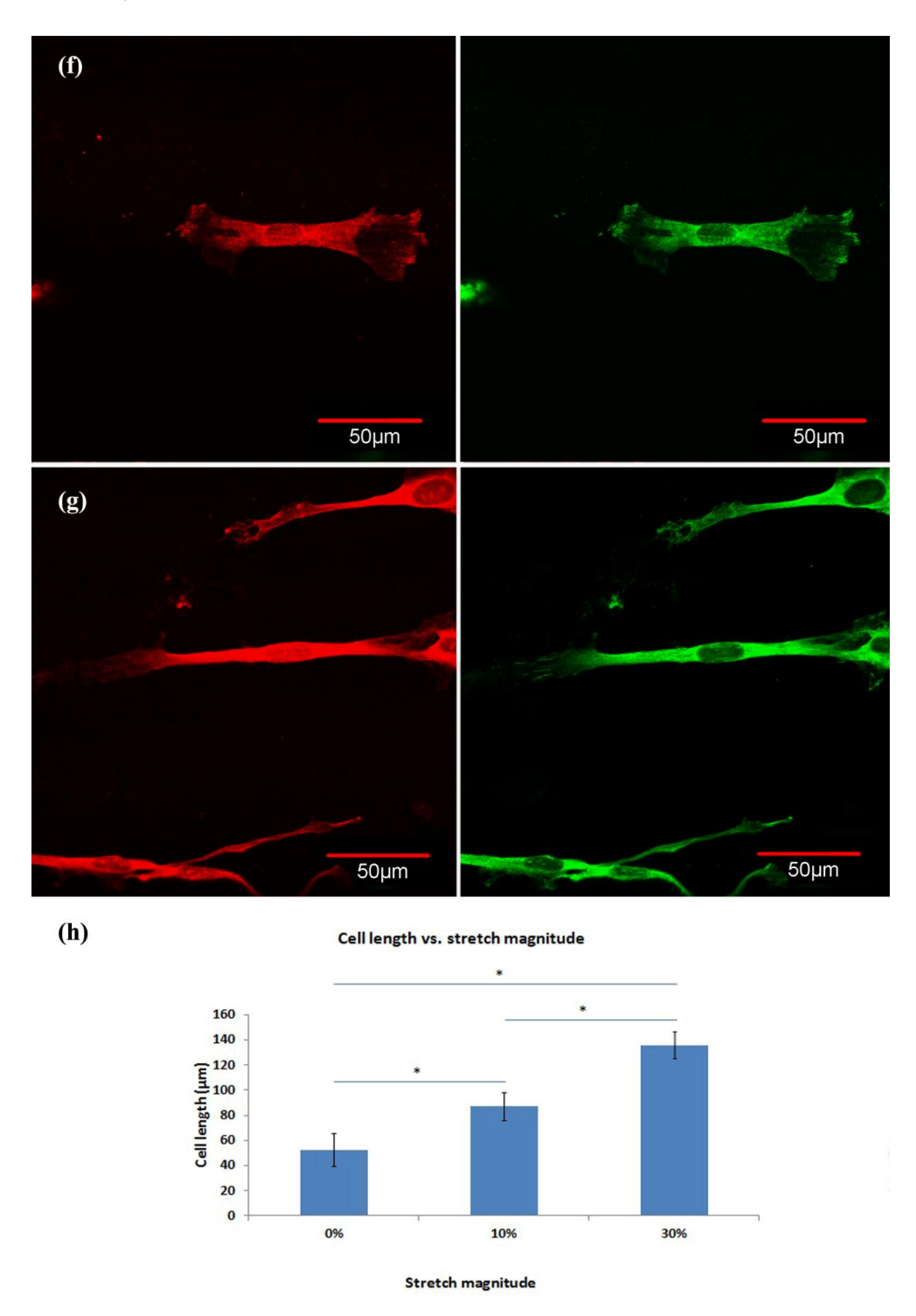
Figure 2.10. Actin filaments and focal adhesion staining of MSCs on stretched vs. unstretched surfaces.

Fluorescence confocal microscopy images were taken of MSCs after 5 days of culture on 10% pre-stretched (a and c) and unstretched (b and d) 35:1 PDMS membranes stained with Texas Red-X phalloidin for actin. Images were taken at 10X (a and b) and 40X (oil) (c and d). F-actin filaments (red) and vinculin (green) staining of MSCs after 5 days of culture on (e) 0%, (f) 10% and (g) 30% pre-stretched 35:1 PDMS membrane with confocal microscopy (60X oil). The average lengths of the cells on 0%, 10% and 30% pre-stretched surfaces were quantified in (h). (*):> 0% stretch, p value < 0.001.; (#):> 10% stretch, p value < 0.0001.

(Figure 2.10 cont'd)



(Figure 2.10 cont'd)



2.4.4 MSC differentiation potential on pre-stretched surface

We evaluated whether the pre-stretch impacted myoblast differentiation potential of the MSCs. The MSCs cultured on PLL coated 10% pre-stretched PDMS membrane for 4 days stained for MyoD1 (Figure 2.11). The MSCs on the pre-stretched surface stained positive for MyoD1 (green) through the entire cell body (Figure 2.11a) and an overlay with F-actin staining (red) showed orange (Figure 2.11b). In contrast, on the unstretched surface the MSCs did not stain for MyoD1 (Figure 2.11c) and an overlay with F-actin showed more red than orange (Figure 2.11d). The increased expression of MyoD1 was quantified (Figure 2.11e) and showed that the expression level of MyoD1 on the stretched surface is significantly higher than on the unstretched surface, thereby indicating that pre-stretch is able to induce early myoblast differentiation of MSCs.

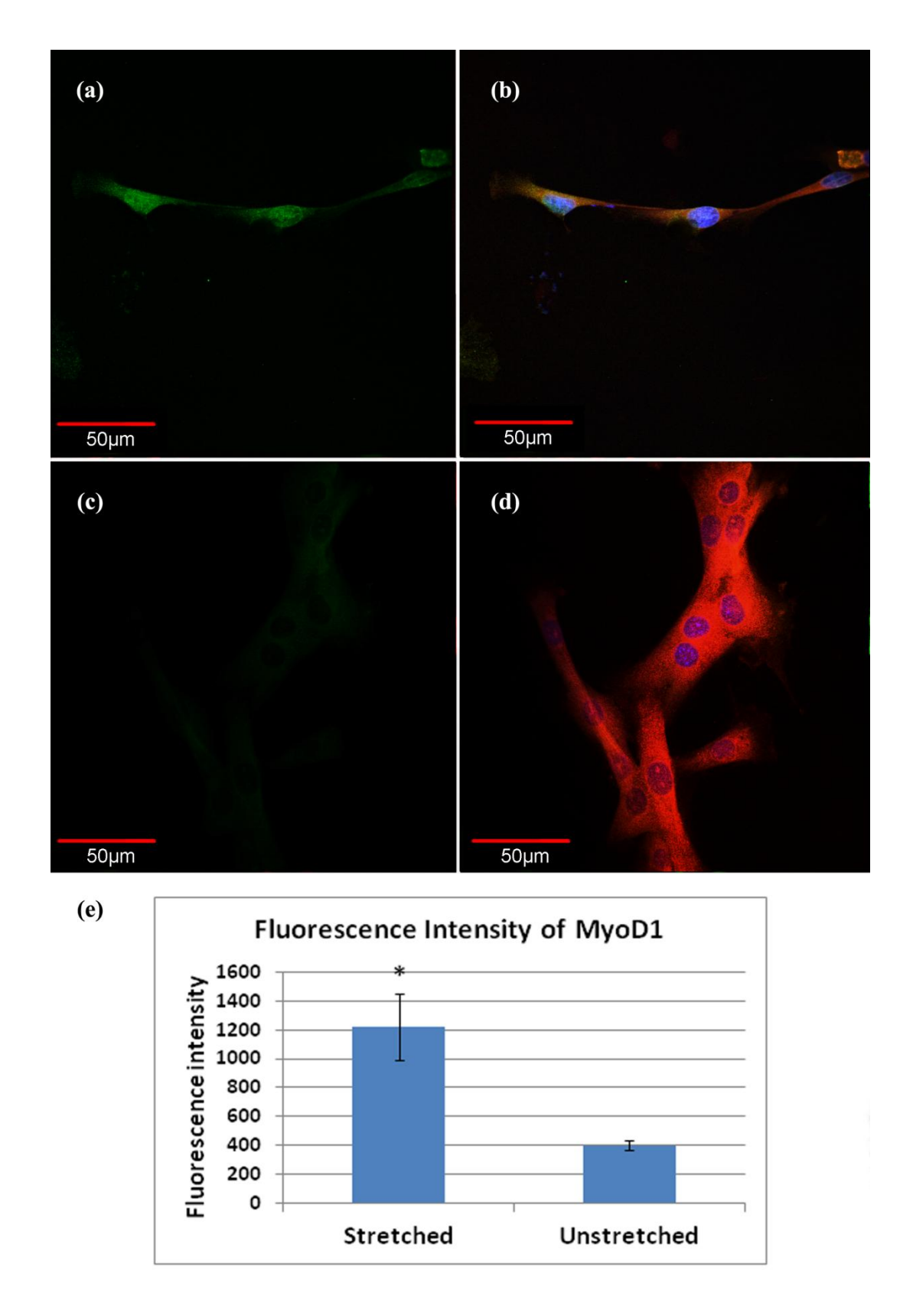


Figure 2.11. MyoD1 Staining of MSCs on stretched vs. unstretched surfaces.

(Figure 2.11 cont'd) Fluorescence images of MSCs after 4-day culture on 10% pre-stretched (a, b) and unstretched (c, d) 35:1 PDMS surface. (a) MyoD1 staining of MSCs on 10% pre-stretched PDMS substrate and (c) unstretched substrate. An overlay of MyoD1 (green), F-actin (red) and nuclei (blue) staining on (b) PLL coated 10% stretched 35:1 PDMS substrate and (d) PLL coated unstretched 35:1 PDMS substrate. Images were generated using confocal microscopy at a magnification of 60X (oil). (e) Quantification of fluorescence intensity of MyoD1 staining on the (a) stretched and (c) unstretched surfaces, *: p value = 0.0012.

2.5 Discussion

2.5.1 Bio-mechanical environment

The mechanical environment is involved in the regulation of tissue structure and function. It is well known that the mechanical microenvironment has a significant impact on cell morphology and behavior. Cells are anchored on the substrate through focal adhesion and the cell morphology is dependent on the cytoskeleton organization. By changing the substrate stiffness [61], applying external force [62] or surface topography [63], the cytoskeleton organization can be manipulated, resulting in changes in cell morphology as well as orientation. *In vivo*, there are several types of cells that align directionally, such as cardiomyocytes [64] and blood vessel endothelial cells [65]. These cells align and are located in an environment that involves mechanical stress and strain. To properly study these cells in an *in vitro* environment that more closely mimics the *in vivo* conditions, i.e. to achieve aligned cells, external mechanical forces are required, such as cyclic stretch on cardiomyocytes or shear stress on blood vessel endothelial cells [66-67]. However, even in the absence of cyclic external mechanical stimuli or shear stress certain types of cells remain aligned, e.g., alignment of cells (neuron, glial, etc.) in the cerebellar cortex [68-69]. Therefore, the objective of this study is to elucidate a possible mechanism of cell

alignment independent of external mechanical forces, namely, through pre-stretch induced surface anisotropy. We believe that insights gained through this study could inform on tissue engineering applications.

2.5.2 Static vs. cyclic stretching

It is well established that cyclic stretching is able to induce cell orientation as well as impact cell proliferation and differentiation [49-50, 70]. Cyclic stretch is a much stronger interference process as compared to our static pre-stretch and the cells' response to cyclic stretch has been shown to depend on the frequency of the cyclic stretch. The cell orientation appeared to be dependent on the magnitude and the frequency of the stretch. In other words, the higher the frequency the faster the cells respond [71] while the lower the frequency the slower the cells respond. When the cyclic stretching frequency is low, e.g. 0.5Hz, the MSCs do not orient, even after 8 hours [72]. Since our pre-stretch is static, it could be extrapolated to a zero frequency (cyclic) stretch, suggesting that the cells would need more time to respond to the anisotropy induced by the stretch and could explain why we have to wait until 24 hrs to see significant alignment as oppose to < 6 hrs with cyclic stretch.

Wang et al. found that orientation was due to the actual reorientation of the cells rather than a selective detachment, and propose the cells subjected to cyclic stretching orient in the direction of minimal substrate deformation [53-54]. In contrast, our results indicate that cells seeded on a pre-stretched substrate preferentially aligned along the pre-stretched axis, which is in agreement with our "active mechano-sensing" model [57]. Nevertheless both studies, Wang et al. [54] and ours, can be explained by cytoskeleton remodeling even though different mechanical inputs were

imposed. When subjected to a dynamic mechanical environment (i.e. cyclic stretching), the cells re-organize their cytoskeletons and attempt to maintain a favorable environment by avoiding the external stimuli of cyclic elongation as well as compression by the substrate. In contrast, on a pre-stretched substrate, the cytoskeleton reorganizes due to the surface anisotropy experienced by the cells. Previously, we showed that cells attempt to maintain a favorable environment by maintaining similar levels of energy consumption through active cellular probing, which manifests as changes in their cell morphology [57]. Here, the cells orient in the stiffer direction, changing their morphology, as a result of active cellular probing because the cells can sense the pre-stretch induced surface anisotropy. These results illustrate that the cells can sense the pre-stretch-induced surface anisotropy without having to experience an external stretching.

2.5.3 Pre- vs. post-stretch

In this study, a static stretch was achieved by pre-stretching the PDMS membrane prior to seeding the cells. In contrast, in almost all the previous studies on the effect of static stretching, the cells were seeded prior to the stretching process. In a recent study static stretching was found not to be as influential as cyclic stretching in inducing MSC orientation [52]. However, our results suggest that static stretch was sufficient to direct significant MSC orientation. We attribute this difference to the different experimental design, as the cells in this experiment did not experience dynamic changes from the external mechanical environment as compared with the previous studies [52]. The major difference between our study and the Goli-Malekabadi's study is that their static stretch started 24 hours after seeding of the cells to allow the cells to attach in [6]. In other words, they seeded the cells and allowed the cells to attach for 24 hours then stretched the cell-attached membrane by 10% and analyzed the results 24 hours after the

stretch was performed. In contrast, our substrate was pre-stretched prior to seeding the cells. Another more minor difference is that in their study they followed the cell orientation for another 24 hours after the stretch, whereas we followed the cell alignment on a pre-stretched surface for up to 4 days. Nevertheless we performed the same experiment as in [6] and found the percentage of cells that align in the stretched direction (using their procedure) was 36%, which was not as high as that on the pre-stretched surface (69%). In their study, the alignment of the cells on the statically stretched surface was not sustained after 24 hours. The cells oriented randomly when cultured on an unstretched PDMS surface for 24 hours (Figure 2.12a, cell orientations are quantified in Figure 2.12d). The cells appeared to align on the PDMS substrate 24 hours after a 10% static stretch of the cell-attached PDMS substrate (Figure 2.12b, cell orientations are quantified in Figure 2.12e). The alignment disappeared after 48 hours on the 10% static stretch PDMS substrate (Figure 2.12c, cell orientations are quantified in Figure 2.12f). However applying a two-sample Kolmogorov-Smirnov test on the orientation distribution from days 1 to 3 suggest the three orientation distributions are not statistically different from each other. This is in accordance with the results of the static stretch reported in their paper [6]. The p-values from our statistical analysis are 0.0982 for day 1 vs. day 2, 0.4255 for day 1 vs. day 3, and 0.2182 for day 2 vs. day 3.

The exact mechanism for the difference is currently unknown. We hypothesize that stretching after cell attachment creates a disturbance to the cell environment, but the previous "memory" or "condition" of the cells in response to the substrate impacts their subsequent response upon stretching of the substrate, similar to pre-conditioning [73], to diminish the cells alignment. In other words, in the post-stretch case the cells are pre-conditioned to an isotropic surface for 24

hours and then a disturbance occurs such that the randomly aligned cells experience an "anisotropic" surface but the pre-conditioning or "memory" causes the cells to show a reduced response to the anisotropy. However in the pre-stretched condition, the cells are not experiencing a disturbance or change in the environment. Instead, one could liken it to cells being pre-conditioned to an "anisotropic" surface for the first 24 hrs, and then this environment continues, such that the cells experience a "memory" of the anisotropy and when the anisotropy persists, the cells continue to align.

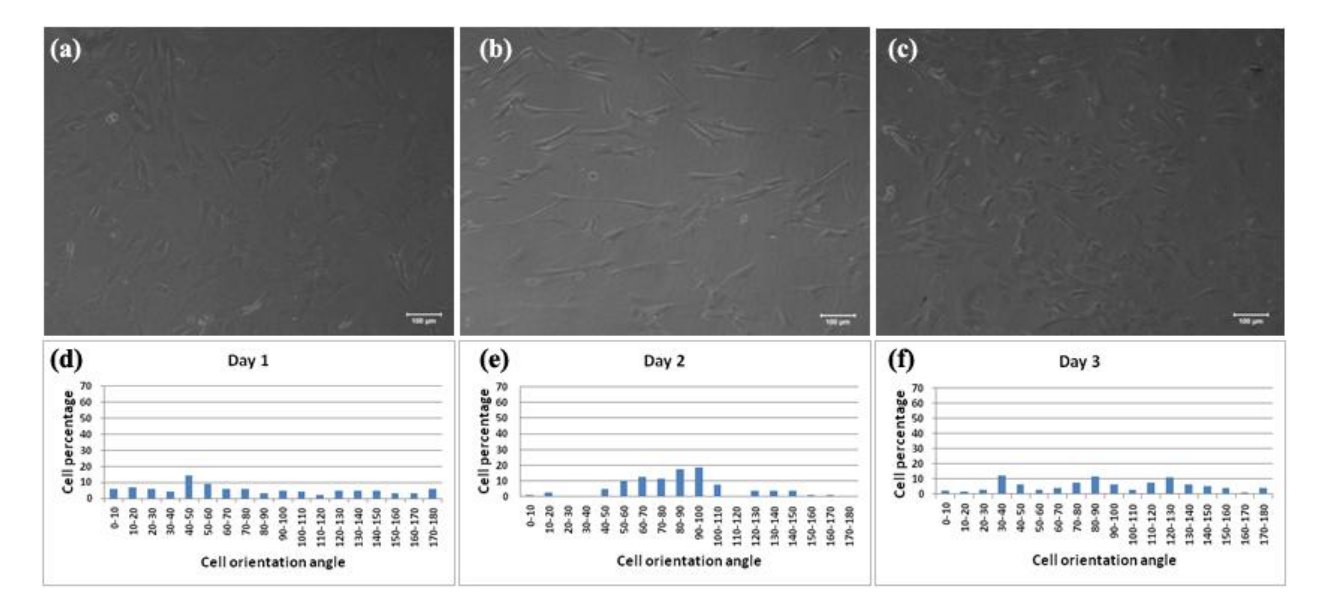


Figure 2.12. MSC orientation upon stretching of cell-attached PDMS surface.

(a) MSCs seeded on PLL coated unstretched 35:1 PDMS membrane for 24 hours (day 1) showed random orientation, orientation angle distribution is shown in (d). (b) MSCs aligned on the PDMS substrate 24 hours after a 10% static stretch of the cell-attached 35:1 PDMS substrate (day 2), orientation angle distribution is shown in (e). (c) MSCs lose their alignment 48 hours after the 10% static stretch (day 3), and the orientation angle distribution is shown in (f). The 35:1 PDMS membranes are coated with PLL. Phase contrast images were obtained at a magnification of 10X. Two-sample Kolmogorov-Smirnov test was applied to evaluate the

(Figure 2.12 cont'd) statistical significance. The cell orientation distributions for days 1, 2, and 3 are not statistically different when compared to each other. The p-values are 0.0982 for day 1 vs. day 2, 0.4255 for day 1 vs. day 3, and 0.2182 for day 2 vs. day 3.

2.5.4 Mechanical force vs. contact guidance

Researchers have long observed a significant effect of surface anisotropy on cell behavior, where the anisotropy is generated by changing the surface topography, which results in changes in both the mechanical properties and topography. In those previous studies, the anisotropic cellular behavior was due to the "contact guidance" [48, 74]. However, it might falsely indicate that anisotropy equals contact guidance. In this study, we used a pre-stretched surface and successfully induced surface anisotropy without modifying the surface topography.

Even without topography, not all anisotropic surfaces are due to effective stiffness. In an earlier experiment, Haston et al. [56] stretched collagen matrix to induce fibroblast orientation. Although their experiment applied a static pre-stretched membrane they found the cells aligned as a result of the stretch-induced oriented collagen fibers. They suggested that contact with the aligned collagen fibers induced cytoskeleton reorganization and the cell alignment. However, in this study a thin layer of PLL coating was added to promote cell adhesion on the pre-stretched membrane, the surface characterization show that this protein layer was evenly distributed so it is not likely affecting the cell alignment. Taken together, in this study we successfully created a purely mechanical force induced anisotropic surface without the influence of contact guidance.

2.5.5 PLL vs. fibronectin coating

PLL is a commonly applied coating that can enhance cell adhesion. There are a number of studies that show cells align on PLL coated patterned surfaces, such as James et al. [75] and Dowell et al. [76]. It is possible that the nonspecific binding of PLL could block potential chemical crosstalk and signaling between the substrate and the cell. Therefore to ensure our results are not due to nonspecific effects of PLL, we repeated the experiment with fibronectin and found the cells also aligned, as was observed with PLL, as shown in the Figure 2.13. Figure 2.13a shows MSCs seeded on fibronectin coated pre-stretched surface and Figure 2.13b shows MSCs seeded on fibronectin coated unstretched surface.

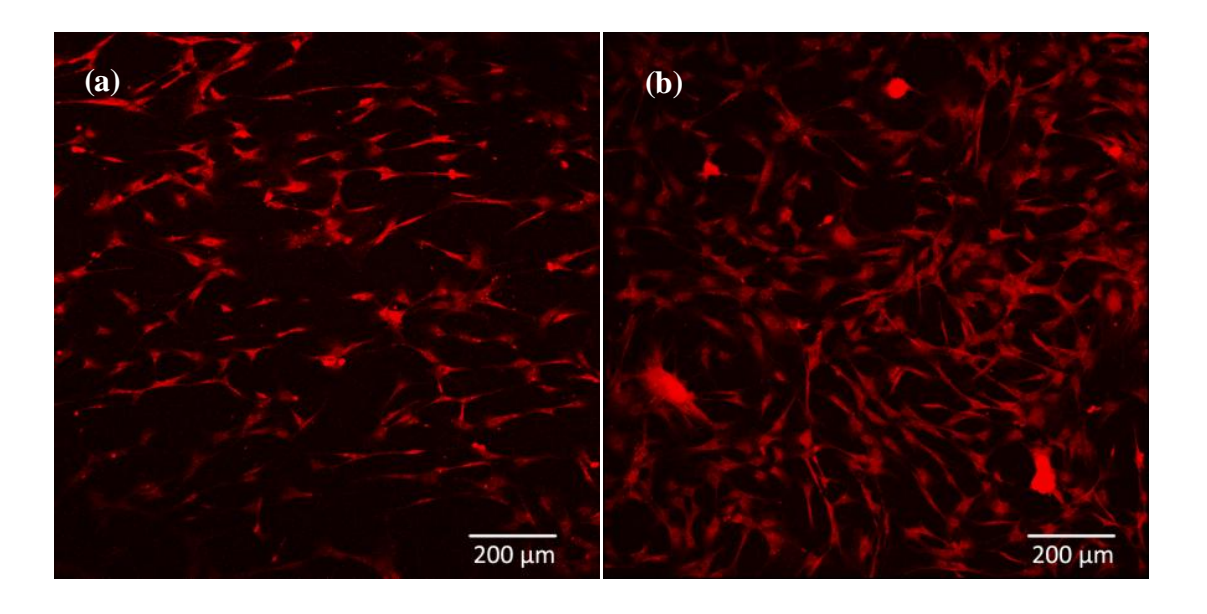


Figure 2.13. MSC oriented on fibronectin coated pre-stretched surface.

F-actin staining of MSCs seeded on fibronectin coated 35:1 PDMS membrane with (a) 10% prestretch and (b) without pre-stretch. Images were captured after 4-days of culture using confocal microscopy at a magnification of 10X.

2.5.6 Application of mechanical stretch in tissue engineering

Mechanical stretch has been applied in tissue engineering to guide cell behavior. It is especially important for inducing cell alignment in connective tissues such as tendons and ligaments, cardiac muscle tissues and blood vessel endothelium [64, 66-67, 77]. Along these lines, we created, alternatively, a static pre-stretched anisotropic surface, in the absence of dynamic external mechanical stimuli that also induced cell alignment. The results of this study could have potential implications to neural cell alignment during development where dynamic mechanical stimuli are not likely playing a role [68-69].

CHAPTER 3 THE IMPACT OF PRE-STRETCH INDUCED SURFACE ANISOTROPY ON AXON GROWTH

3.1 Introduction

As a leading cause of disabilities worldwide, spinal cord injury (SCI) is characterized by an acute traumatic lesion of neural elements in the spinal canal, which results in temporary or permanent deficits in sensory and motor function [78]. Structurally, axon tracts in the spinal cord, composed of highly ordered and aligned bundles of axons, form complex networks of connectivity. After acute SCI, axons sprout briefly, but soon undergo growth arrest and retraction due to the lack of secreted growth factors from associated glial cells and neurite orientation or alignment within the scar tissue, which prevent the axons from crossing into the lesion site [9-10]. If the nerve's gap from an injury is large, the distal and proximal ends of the damaged nerves are unable to communicate efficiently, thereby deterring the regeneration process. Transplantation of Schwann cells (SCs) or olfactory ensheathing cells has been shown to induce axon regeneration to an extent, with partial recovery of motor and sensory functions, as unorganized axon alignment leads to disordered regeneration [79-80]. Therefore, to persuade a sufficient number of regenerating axons to bridge the lesion site, it is necessary to have properly organized axonal alignment.

Biomaterials used to fabricate scaffolds and implantable substrates for nerve regeneration have been investigated for their ability to modulate mechanical cues such as substrate stiffness, topological features, and stretch to control neural cell growth, and have shown potential in neural regeneration post-SCI [81-84]. To elicit axon outgrowth from regenerating neurons, topological features have been reported as critical for providing contact guidance [81-82, 85]. Consequently,

significant effort has been invested in developing techniques that induce axon alignment to promote neural regeneration. Topological guidance achieved through aligned fibers, channels, and patterning have facilitated axon alignment [81, 86], but were unable to increase the length and thickness of the axons [87]. Furthermore, when transplanted *in vivo*, axons encounter difficulties in penetrating through the scaffold channels due to the formation of a reactive cell layer [20, 88].

Alternatively, gradually stretching the substrate at a constant rate has led to axon alignment in the stretch direction with increasing axon length over time [89]. Despite these promising results, translating these technologies into effective therapies remains elusive due to the complexity of the experimental setup. Therefore, alternative approaches for axonal regeneration are needed. Demonstration that anisotropic stress *in vivo* induces orientation and affects cell morphogenesis [90] inspired us to pursue an approach that capitalized on surface anisotropy based on static prestretch to facilitate axon regeneration for SCI repair.

We previously demonstrated that the static pre-stretch creates surface anisotropy that influences cell alignment and growth [87, 91-92]. While anisotropy is often attributed to the contact guidance provided by surface topography [93-96], it differs from surface anisotropy. Briefly, the surface anisotropy can be generated through mechanical stretching, i.e. pre-stretch, which we previously explored with poly-dimethyl-siloxane (PDMS) membranes to induce mesenchymal stem cells (MSCs) to express MyoD1. To predict the effective stiffness that the MSCs sense in the stretched direction, a finite elastic theory of "small deformation superimposed on large" [58] was applied. The MSCs were able to sense the anisotropy by actively pulling on the surface and

orienting in the pre-stretched direction [91]. Here we report axon alignment on a static pre-stretched PDMS substrate and show that static pre-stretch induced surface anisotropy enhanced axon alignment and growth of dorsal root ganglion (DRG) neurons, and myelination of the axons by SCs. Both the DRG neurons and SCs are regularly used in clinical models of neural regeneration for spinal cord injury. DRG neurons have been demonstrated to survive upon clinical transplantation [97-99]. The roots of DRGs close to the lesion site are known to enter the spinal cord and extend processes across the host-graft interface [100]. DRG nerve constructs are amendable to nerve repair since their axons can lengthen extensively to bridge the lesion [101]. SCs can migrate to the spinal cord injury to promote neural repair and myelinate the regenerated axons [102].

We designed a static pre-stretched cell culture system that provided surface anisotropy without topological features, enabling DRG neurons to extend thicker axon aggregates along the stretched direction and form aligned fascicular-like axon tracts. Moreover, the SCs aligned and co-localized with the aligned axons and expressed P0 protein, a marker for mature SCs and an indicator of myelination, thereby demonstrating that surface anisotropy is beneficial in enhancing axon alignment and growth, and myelination. We also compared the effect of stretch-induced anisotropy with that of topography-induced anisotropy. Although axons from cultured DRG neurons showed alignment on micropatterned PDMS channels, the axons in the channels do not form neatly aligned axon tracts or increase their thickness as on the pre-stretched surface, indicating an advantageous effect of pre-stretch induced anisotropy on regenerating axon growth.

3.2 Materials and methods

3.2.1 Materials

PDMS substrates were prepared using an 184-silicone elastomer kit purchased from Dow Corning (Midland, MI). A FlexiPERM ConA Silicone chamber was purchased from Greiner bioone (Monroe, NC). Poly-L-Lysine was purchased from Trevigen (Gaithersburg, MD). Poly-D-Lysine, Fluoro-2 deoxy-uridine, Uridine, Cytosine β-D-arabinofuranoside (AraC), Anti-Thy 1.1 antibody (cat. no. M-7898), and Rabbit Complement were purchased from Sigma-Aldrich (St. Louis). Heat inactivated Fetal Bovine Serum was purchased from Hyclone (Logan, Utah). Bovine Pituitary Extract (BPE) was purchased from Clonetics (Allendale, NJ). Forskolin was purchased from Calbiochem (Billerica, MA). Type I Collagenase was purchased from Worthington (Lakewood, NJ). Neurobasal Medium 1X, B-27 Supplement, Glutamax-I, Albumax-I, Nerve Growth Factor, Dulbecco's modified Eagle medium (DMEM), penicillin, streptomycin, 0.25% trypsin-EDTA, 1X-phosphate buffered saline (PBS), HEPES buffer and immunostaining components (mouse anti- β-III tubulin antibody (cat. no.4466), Alexa Fluor 488 goat anti-mouse IgG secondary antibody, Alexa Fluor 546 goat anti-rabit IgG secondary antibody, and DAPI) were purchased from Invitrogen (Carlsbad, CA). Bovine Serum Albumin (BSA) was purchased from US Biological (Marblehead, MA). Rabbit anti-Myelin Protein Zero antibody (cat. no. ab31851) was purchased from Abcam (Cambridge, MA).

3.2.2 Pre-stretched PDMS substrate preparation

Each PDMS substrate was cured in polystyrene tissue culture dish by mixing a 10:1 solution of base and curing agent with the mixture in the dish at 1-mm thickness. The mixture was kept under vacuum for 20 minutes to remove air bubbles and then cured overnight at 60 °C. The

PDMS surface was further cleaned with a PX-250 plasma cleaning/etching system (March Instruments) for 3 minutes at 165 mTorr and 65 sccm flow of O₂. A piece of rectangle PDMS membrane (5cm×3.5cm) was fixed onto the stretching frame and the frame was then placed on the stretching stage. The membrane was stretched evenly with 10% elongation in the longer axis and the stretch was fixed (Figure 3.1a). A silicone chamber was placed on top of the PDMS membrane, which provided a circular well to hold the culture medium. The entire device design is shown in Figure 3.1a. Before seeding the DRG neurons, 1.5 ml of PLL was added to the PDMS membrane and incubated for 2 hours within the chamber to enhance cell attachment.

3.2.3 PDMS channel substrate preparation

Different size (50 µm and 200 µm) channel patterns were designed with equally sized grooves and ridges using AutoCAD. Photolithography was used to fabricate the micropatterned silicon wafers that served as molds to transfer the microgrooves onto PDMS substrates as described previously [103]. PDMS substrates of 10:1 mixed base and curing agent were cured at 60 °C overnight. PLL was subsequently added to the chamber and incubated for 2 hours prior to seeding the DRG neurons.

3.2.4 PDMS surface characterization

Surface topography was analyzed by scanning electron microscope (JSM-7500F cold field emission SEM, JEOL Corporation) in the secondary electron imaging mode. An acceleration voltage of 12 kV was used for all experiments. Images were taken at a magnification of 1500X.

3.2.5 Tensile test

The mechanical properties of the substrate (i.e. PDMS membrane) were measured by the uniaxial tensile test, and the mechanical behavior was described by the incompressible, isotropic neo-Hookean model described previously [104].

3.2.6 DRG neuron and Schwann Cell isolation and culture

All procedures for cell isolation were approved by the Institutional Animal Care and Use Committee at Michigan State University.

DRG neurons are isolated from 5-8 day-old Sprague-Dawley rats. Briefly, after sacrificing the pups by decapitation, the skin overlying the spinal cord is cut away and any excess tissue is removed from the spinal cord. The spine is then completely removed from the body, and the spinal cord is extracted. Using a fine pair of tweezers and a pair of microsurgery scissors, approximately 10–16 DRGs are collected from both sides, trimmed of nerve roots and transferred to 5 ml of ice-cold HBSS buffer containing 1 ml penicillin/streptomycin. The dissection medium containing DRGs are then transferred into a new 15-ml tube, centrifuged at 900 RCF at 4 °C for 5 minutes. After centrifugation, the supernatant is removed and the DRGs are incubated in 6 ml of 0.05% Trypsin-EDTA (1X) (Sigma; 1 mg/ml, 45 min) at 37 °C and followed by 2 ml collagenase (Sigma; 500 U/ml, 20 min) at 37 °C. After chemical dissociation, the ganglia are centrifuged at 900 RCF in 4 °C for 5 minutes and the supernatant is subsequently removed. The pellet is further resuspended in 10 ml of standard growth media and centrifuged, as described above. After washing with medium, the cells are resuspended in standard growth media containing Neuralbasal A medium containing B-27 supplement, antibiotic

(penicillin/streptomycin), Albumax-I and nerve growth factor. The dissociated neurons are then plated onto the PLL coated pre-stretched surface and incubated at 37 $\,^{\circ}$ C at 5% CO₂.

SCs are isolated using the same protocol as described previously [105]. One-day old pups are sacrificed by decapitation. The sciatic nerves are then extracted by making an incision from the tail up the spine to the inner thigh near the foot. Nerve sections are cut into small pieces and transferred into dissociation medium containing collagenase and trypsin and incubated for 45 minutes at 37 °C. Mechanical dissociation is done using an 18-gauge needle and 10-ml syringe. Cells are then centrifuged for 5 minutes and resuspended in Dulbecco's modified medium E containing 10% fetal bovine serum and 1% antibiotic (penicillin/streptomycin). Purification begins upon adding AraC into the medium after 48 hours of culture, followed by antibody selection using Anti-thy 1.1 antibody and Rabbit Compliment on day 5.

The co-culture of DRG neurons and SCs was performed after 2 weeks of culture of purified DRG neurons on stretched and unstretched surfaces by adding the SCs to the DRG culture at a cell density of 5000 cells per ml. The co-culture was maintained for 1 week and then subjected to immuno-staining.

3.2.7 Immunocytoche mistry

Immunocytochemistry was performed at room temperature on cells seeded on the stretched surface for 6, 12, and 21 days. Cells were rinsed with PBS, followed by fixation with 4.0% paraformaldehyde in PBS for 15 min, rinsed 3 times in PBS, then permeabilized with 0.1% Triton X-100 in PBS for 15 min and washed 3 times with PBS. After washing, the cells were

blocked in 1% BSA for 30 minutes. After BSA blocking, the cells were incubated with mouse anti-mouse β-III tubulin primary antibody (1µ1 stock per 500µl of 1% BSA solution) for 1 hour, or rabbit anti-P0 primary antibody (1:500 dilution in 1% BSA solution) for 1 hour followed by three washes in 1X PBS, and then incubated with Alexa Fluor 488 goat anti-mouse or anti-rabbit Alexa Flour 546 secondary antibody (1:500 dilution in 1% BSA solution) for 1 hour. Cells were washed again, three times in 1X PBS and then incubated for 5 minutes in 300nM DAPI to visualize the nucleus. The PDMS substrates were air dried and the silicone chamber was removed from the membrane; the stained PDMS membrane was finally kept in the dark to cure for 24 hours at room temperature. Confocal laser scanning microscopy (CLSM) images were obtained with Olympus Fluo View1000 laser scanning confocal microscope using 20X objectives.

3.2.8 Quantification of axon orientation distribution and axon thickness

Image-Pro Plus Version 4.5 was used to measure the axon orientation angles. Briefly, before measurements, the fluorescent images were converted into high contrast binary images to remove the background noise. A straight line was drawn perpendicular to the stretch direction, which was used as the reference to indicate zero degree orientation. For each axon, the orientation was measured by drawing a straight line to follow the axon pathway, and the angle between the traced line and the reference line was automatically given by the software and recorded for further analysis. All experiments were repeated at least three times for statistical verification. For the stretched vs. unstretched comparison, the DRG neurons seeded on the stretched and unstretched membranes were from the same isolation. For each experiment, we took 8 images under the same condition and quantified the axon orientation angles. We counted the axons at each ten degrees of orientation and normalized the number to the total number of

axons in each condition. For axon thickness analysis, we enlarged each image by 10X, and measured the axon thickness by pixels, which were later converted into microns. The mean value and standard deviation of the axon thickness were reported.

3.2.9 Quantification of co-localization of axon and SCs

The fluorescent images of the co-culture were processed by setting the threshold of each color channel to remove background noise, and the co-localization was automatically quantified using the FV1000 software. The percentage of green that overlapped with red was calculated for both the stretched and unstretched surfaces. For statistical analysis, three biological samples were quantified, with 6 images analyzed for each sample.

3.2.10 Statistical analyses

Data were expressed as mean ± standard deviation. A two-sample Kolmogorov-Smirnov test was applied to evaluate the statistical significance for Figure 3.3. A two-sample Student's t-test was used to determine statistical significance for Figure 3.4 and Figure 4.6e. ANOVA-Tukey's test was applied to assess for significance in Figure 3.5. In all cases, p values of <0.05 were considered statistically significant.

3.3 Results and discussion

3.3.1 Design and characterization of pre-stretched surface

Using a previously designed cell culture system that induced alignment of MSCs, we explored how surface anisotropy affects axon alignment and growth. The cell culture system is composed of a PDMS membrane fixed onto a sliding frame, and placed on a stretching stage used to control the magnitude of pre-stretch (Figure 3.1a). The DRG neurons were seeded subsequent to

stretching the PDMS substrate, i.e. substrate pre-stretch, ensuring no other external forces were applied to influence the axon growth.

To ensure that there were no topographical features on the pre-stretched PDMS substrates that might affect axon alignment, e.g. fibers, the surface was imaged with the secondary electron imaging mode in SEM. SEM images of pre-stretched (Figure 3.1bi and 3.1bii) and unstretched (Figure 3.1biii and 3.1biv) surfaces, both with (Figure 3.1bii and 3.1biv) and without PLL coating (Figure 3.1bi and 3.1biii), showed that the stretch did not induce any topological features on the PDMS substrate (Figure 3.1bi and 3.1biii). The dehydrating imaging condition caused the PLL peptides to aggregate into large particles on the membrane surface (Figure 3.1bii and 3.1biv). Nonetheless both surfaces, including the PLL coated surface, show a smooth background without any surface topography (i.e., orienting features) that would provide contact guidance for axon alignment.

A non-linear parameter estimation method was used to fit a neo-Hookean model to the results of a uniaxial tensile test of the PDMS substrate. The material behavior shows a linear elastic behavior up to a strain of 0.2 as shown in the left panel in Figure 3.1c. A pre-stretch value of 0.1 (10%) was used in the experiments. The left panel in Figure 3.1c shows the experimental data of the Cauchy stress vs. engineering strain for the 10:1 crosslinked PDMS membrane while the middle panel compares the model with the measured values of the engineering stress as a function of the engineering strain. See our previous study [59] for details on the parameter estimation using a finite elastic constitutive model.

The stretch-induced anisotropy of the PDMS membrane is represented by the ratio of effective stiffness in the stretched direction to its perpendicular direction (i.e., $\hat{E}_{1111}/\hat{E}_{2222}$). The effective stiffness in both directions with respect to the change in strain is shown in the right panel in Figure 3.1c. When there is no stretch, $\hat{E}_{1111}=\hat{E}_{2222}$ (1.45 MPa), which provides the elastic modulus of the 10:1 crosslinked PDMS membrane. As the stiffness in the stretched direction increases, the stiffness in the perpendicular direction decreases as the PDMS membrane experiences more strain during the uniaxial stretch. The predicted anisotropy of the PDMS membrane under a 5% strain is approximately 1.158.

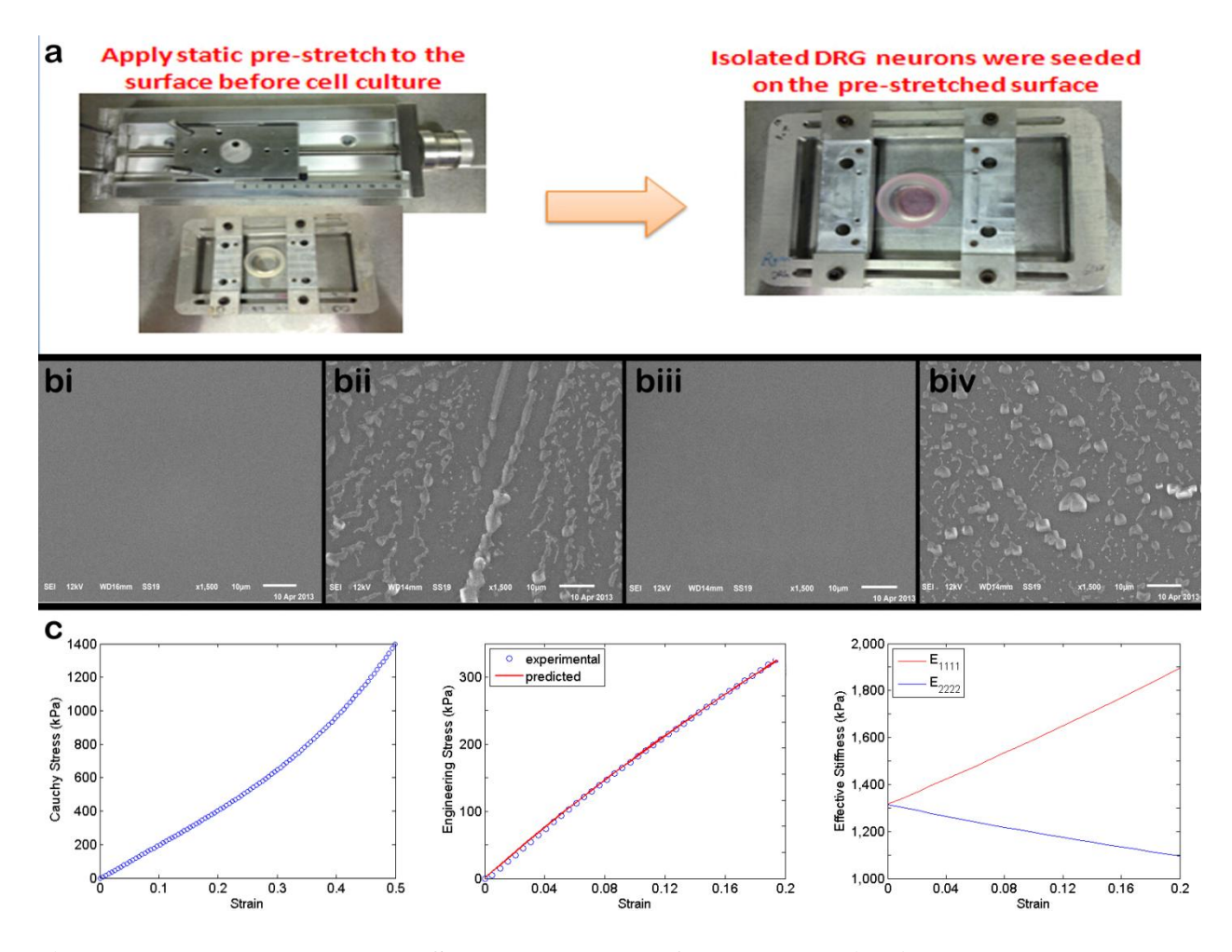


Figure 3.1. Pre-stretched PDMS substrate and surface characterization.

(a) PDMS membrane was placed on the stretching frame, and after the stretch was selected and secured, the DRG neurons were seeded onto the chamber; (b) SEM images of pre-stretched (bi and bii) and unstretched (biii and biv) PDMS surface with (bii and biv) and without (bi and biii) PLL coating; and (c) Stretch-strain plot and effective stiffness curve. The tensile test was performed on the 10:1 crosslinked PDMS membrane and the true stress-strain curve is shown for one of the samples in the left panel. A neo-Hookean was used to fit the experimental data in the middle panel, and the predicted effective stiffness in both the stretch and perpendicular directions is depicted in the right panel.

3.3.2 Axon alignment on pre-stretched surface

The DRG neuron cell suspension added to the chamber on the pre-stretched PDMS substrate was cultured for 6, 12, and 21 days to assess for DRG axon alignment. To examine axon growth, the cells on the pre-stretched and unstretched PDMS substrates were stained for β -III-tubulin (Figure 3.2). The DRG axons on the pre-stretched surface aligned parallel to the stretched direction, while the axons on the unstretched surface aligned randomly and formed interconnected network. The axons on the pre-stretched substrate increased their alignment over time and formed longer and thicker fascicular axon tracts, which resembled the in vivo nervous systems. The pre-stretch induced axon alignment was quantified and compared with the axons on the unstretched substrates according to the orientation angle (Figure 3.3), where 90° is parallel to the prestretched direction and has the highest effective stiffness. The axon alignment was quantified by determining the percentage of axons that aligned at 10 ° intervals. The pyramid shape of the bar graph is maintained over time on the stretched substrate indicating the percentage of axons that aligned remained constant. In contrast, the axons on the unstretched surface did not align. The distribution of cell orientation on the unstretched surface were statistically different than on the stretched samples based on a two-sample Kolmogorov-Smirnov test on days 6, 12, and 21 (pvalues are 0.001, 0.002, and 0.001, respectively).

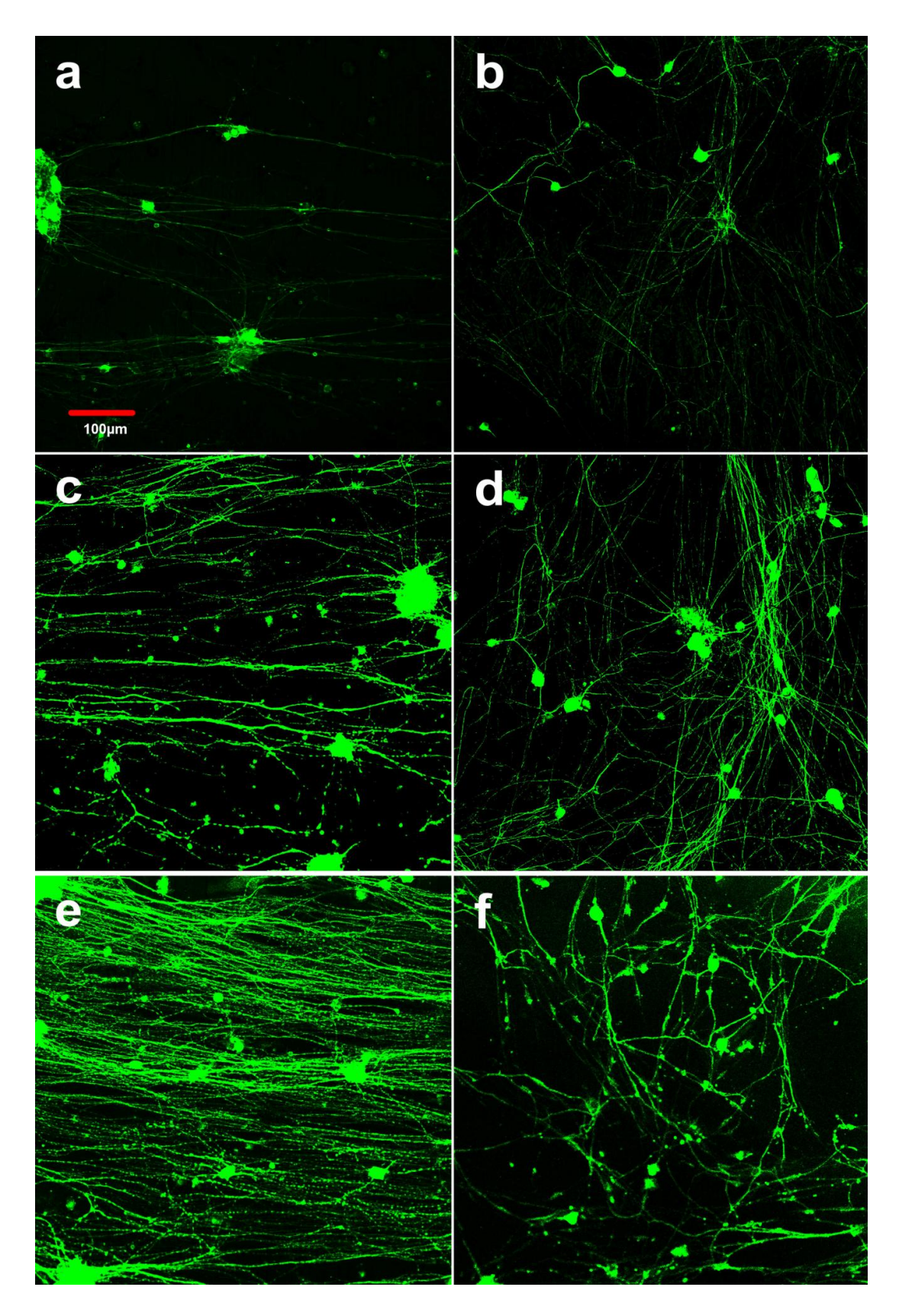


Figure 3.2. Axon alignment on pre-stretched and unstretched surface.

(Figure 3.2 cont'd) Fluorescent images of DRG neurons seeded on the static pre-stretched surface for (a) 6, (c) 12, and (e) 21 days, as compared with DRG cells seeded on the unstretched surface for (b) 6, (d) 12, and (f) 21 days. Axons were stained with anti-mouse β -III tubulin, and imaged with confocal microscopy (10X).

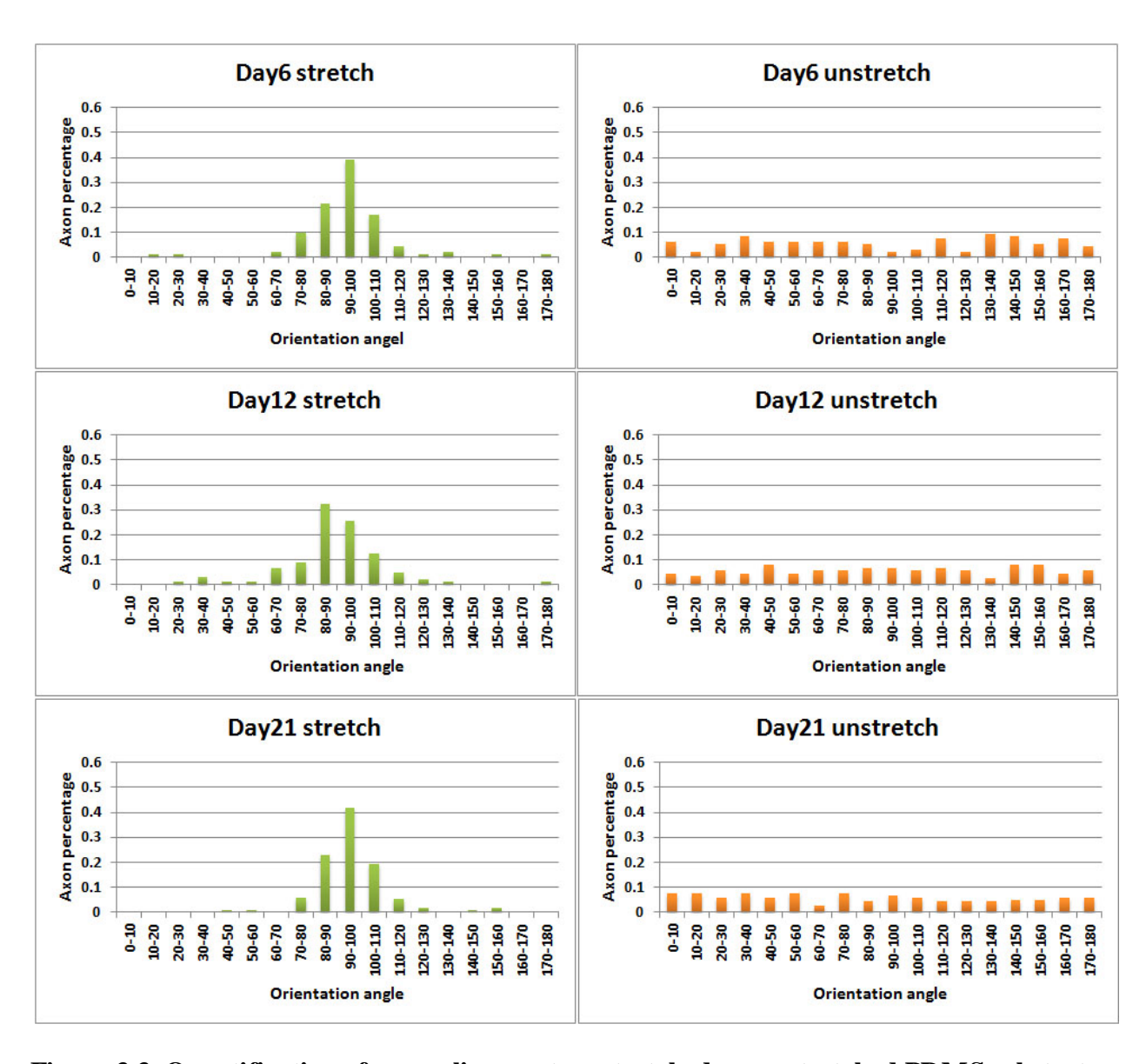


Figure 3.3. Quantification of axon alignment on stretched vs. unstretched PDMS substrate.

The ratio of DRG axon alignment at every 10 degrees on the pre-stretched and unstretched surfaces after 6, 12, and 21days, with 90 degrees representing the direction of the pre-stretch. Orientation angles were quantified by ImagePro Plus. The two-sample Kolmogorov-Smirnov test was applied to evaluate the statistical significance. The cells on the unstretched surface as compared to the cells on the corresponding stretched samples for 6, 12, and 21 days have statistically different distributions, p = 0.001, 0.002, and 0.001 respectively.

This observation is in agreement with our previous report of MSC alignment on pre-stretch induced anisotropic surface, which can be explained by the theory of active sensing. A possible explanation for the alignment of the DRG is that neurons can generate forces through the growth cone to sense the substrate stiffness [84, 106]. Growth cones can actively generate forces and sense the substrate stiffness and thus may be sensing the higher effective stiffness in the pre-stretched direction leading to its alignment in the direction of maximum effective stiffness.

During development and regeneration of the nervous system, neuronal growth cones navigate through tissues and experience environments with different mechanical properties established by the cytoarchitecture of the nervous tissue and surrounding tissues [107]. Koch *et al.* previously showed the growth cones of DRG neurons generate extensive traction force during axon extension, which is strongly dependent on the substrate stiffness [106]. The contractile forces that growth cones exerted have been associated with filopodia [108]. Thus, the axon alignment on the pre-stretched surface is potentially due to the active sensing by growth cones. Similar to MSCs, the filopodia of the growth cone actively pull on the substrate though binding sites, allowing cells to sense the difference in effective stiffness of the substrate in different directions [18]. This could cause the growth cone to move in the direction of maximum effective stiffness. In the present study, both the pre-stretched and unstretched substrates were coated with PLL and showed no topological features (Figure 3.1b), ensuring that the axon alignment was due to the pre-stretch induced anisotropy. Taken together these results suggest that active cell sensing is likely to explain the axon growth.

3.3.3 Enhanced axon thickness growth on pre-stretched surface

In addition to inducing axon alignment, the pre-stretch induced anisotropy appeared to enhance the fasciculation of axons. The aligned axons on the stretched surface formed thick clusters, which is quite different from the random axon network on the unstretched surface. The axons on the pre-stretched substrate grew thicker over time (Figure 3.4a), with some aggregates forming clusters that appear similar to fascicular tracts. To evaluate this fascicular-like effect on the pre-stretched surface, we measured the thickness of each single unit of the axon in the images, where the unit might contain individual or multiple aggregated axons, which were not easily distinguishable. The axon cluster thickness on both the stretched and unstretched surfaces on days 6, 12 and 21 increased over time. However, the average axon cluster thickness after 21 days of culture on the stretched surface was 1.5 times greater than on the unstretched surface, suggesting that the anisotropic pre-stretched surface has the potential to promote extensive axon growth.

Since axon alignment is a prerequisite for fascicle formation [109], the alignment might also be facilitating the fascicular-like effect observed on the pre-stretched surface. This fascicular-like effect has also been observed to increase on a gradually increasing stretching device, where axons were stretched daily using a stepper motor [89], similar to what was observed in this study. However, the quantification in Figure 3.4b was a combined effect of both fascicular-like tracts and single axon thickness increase. Thus, to differentiate between the fascicular-like tracts and single axons, we selected the 10 thinnest axon units on the stretched and unstretched surfaces in each image and measured their thicknesses and found that the mean single axon thickness on the pre-stretched surface was significantly larger than that on the unstretched surface (Figure 3.4c).

The average thicknesses of the single axons grew over time and were 1.17 μ m, 1.60 μ m, and 4.31 μ m on the pre-stretched surfaces and 1.01 μ m, 1.43 μ m, and 2.80 μ m on the unstretched surface after 6, 12 and 21 days of culture, respectively. The results on the unstretched surfaces are in agreement with the 2-3 μ m axon diameter reported in the CNS, which includes those in the brain that are typically thinner than in the spinal cord [12, 110], indicating the unstretched surface did not hamper the growth of axons. The axon thickness on the pre-stretched surface are similar to the mean diameters of 4.18 μ m and 5.95 μ m reported, respectively, for myelinated sensory axon proximal and distal to lumboscaral dorsal root ganglia [111], which are known to be the thickest axons in the CNS. Therefore, the pre-stretch induced anisotropic surface not only enhances fascicular-like tract formation but also increases single axon thickness.

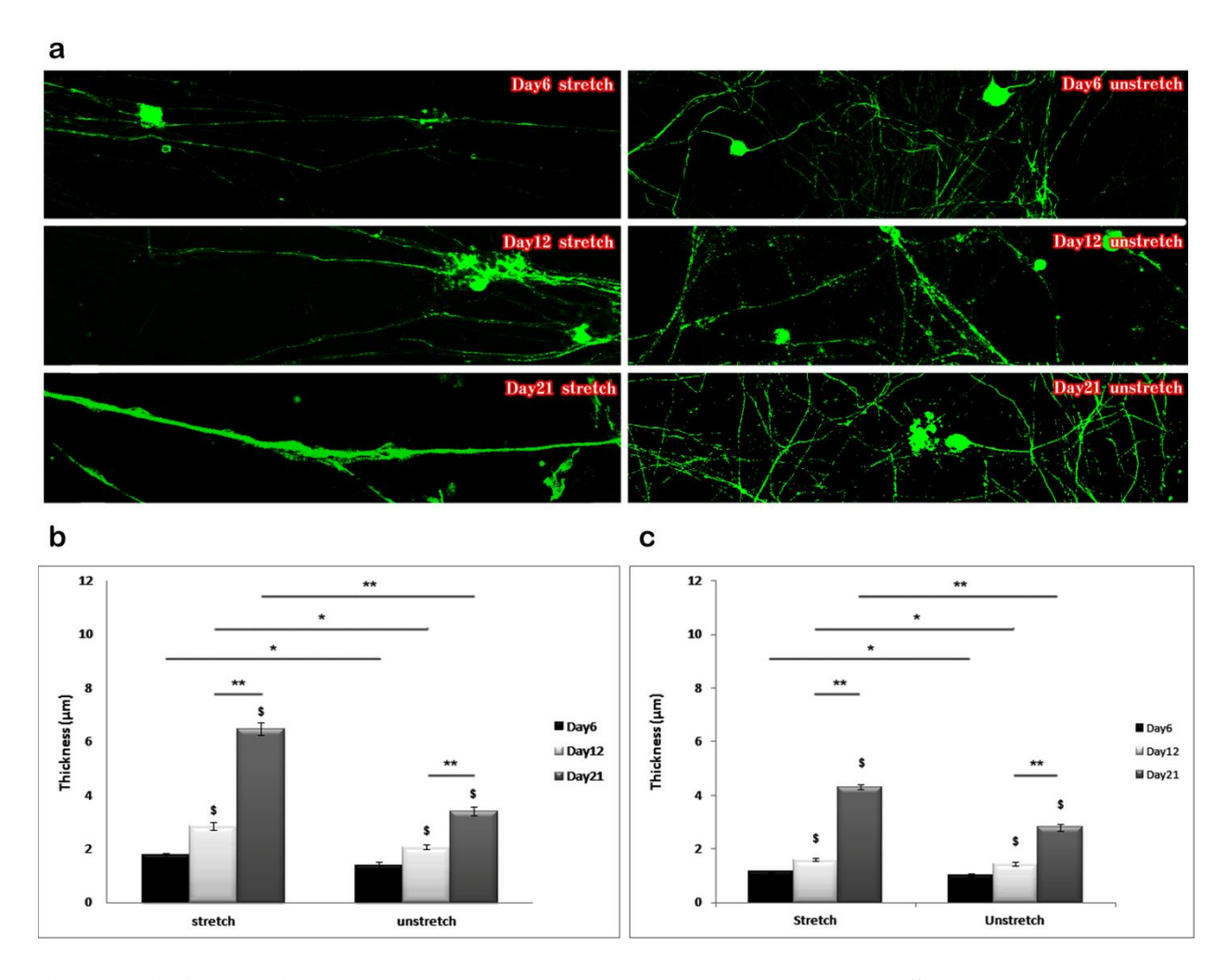


Figure 3.4. Axon thickness growth on stretched vs. unstretched PDMS substrate.

(a) Fluorescent images of the DRG axons on the stretched (left) and unstretched (right) surfaces after 6 (top), 12 (middle), and 21 (bottom) days. Axons were stained with anti-mouse β -III tubulin, and imaged with confocal microscopy (10X); (b) Quantification of DRG axon bundle thickness on the pre-stretched and unstretched surfaces after 6, 12, and 21 days; and (c) Quantification of single DRG axon thickness on the pre-stretched and unstretched surfaces after 6, 12, and 21 days. \$ p < 0.01, * p < 0.05, ** p < 0.01.

Axon alignment, given its significance in neural regeneration, has been extensively investigated [20, 95, 112-114]. Topological features such as fibers and channels provide contact guidance and

are commonly used to guide axon extension along the surface topography. There has been no study to date that demonstrated topological contact guidance induces both increases in axon thickness and a fascicular-like effect. To test this, we further cultured DRG neurons for 21 days on micropatterned channel surfaces of 50 μ m and 200 μ m, wherein the ridges and channels were of equal dimensions (Figure 3.5a). The contact guidance induced by the channels causes the axons to align to some extent (Figure 3.5b), however, the thicknesses of the axons on the channels were significantly smaller than on the pre-stretched surface (Figure 3.5c), suggesting that the pre-stretch induced anisotropy could be more effective for enhancing axon growth for neural regeneration.

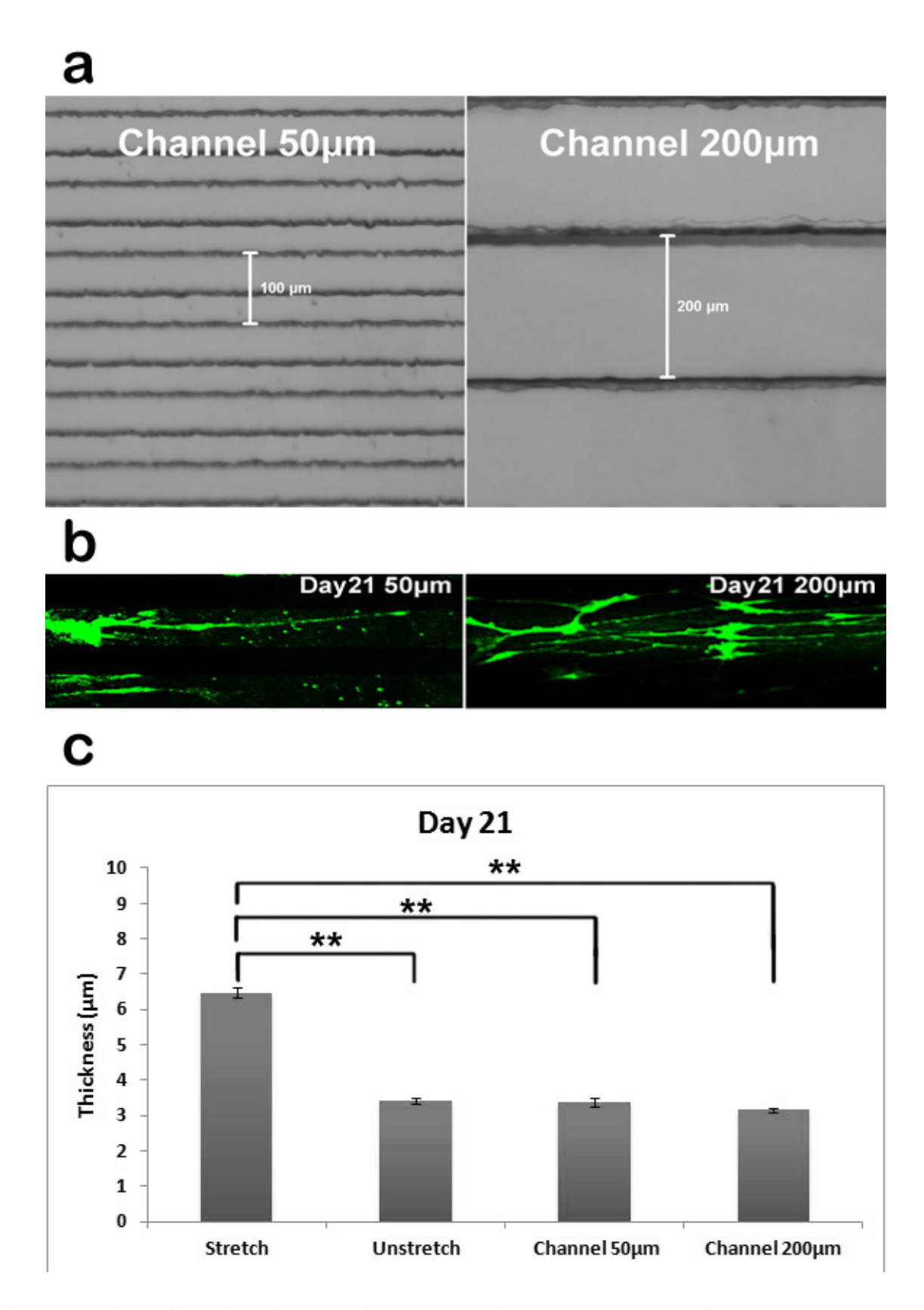


Figure 3.5 Quantification of axon thickness on micropatterned PDMS substrate.

(Figure 3.5 cont'd) (a) Phase contrast images (10X) of micropatterned channels of $50\mu m$ (left) and $200\mu m$ (right) widths; (b) DRG axons on channels of $50\mu m$ (left) and $200\mu m$ (right) widths after 21 days of culture were stained with anti-mouse β -III tubulin and imaged with confocal microscopy (20X); and (c) Comparison of axon thickness on the channels vs. on the prestretched PDMS substrate after 21 days of culture. ANOVA-Tukey's test was applied to assess for a significant difference. **: p < 0.01.

The exact mechanism of this pre-stretch induced axon thickening and fascicular-like effect is unclear. Evidence suggests, however, that microtubules may be involved in this process [115]. There are three main filamentous components inside axon tubular structures, including microtublues, neurofilaments, and the microtrabecular matrix [116-117]. Although there have been studies that showed neurofilaments are responsible for providing mechanical strength, a recent study suggests that microtubules contribute a majority of the mechanical stiffness to the axons [118]. Previous studies indicate that mechanical tension facilitates the growth of the axon, which may be associated with tensile loading of the microtubule bundle and subsequent growth. Microtubules have been suggested as mechanical force sensors that can detect the force direction and magnitude [115, 119-120]. Axons on the pre-stretch surface showed more β-III-tubulin, a marker of microtubule components, indicating thicker axons, thereby raising a possibility that the pre-stretch might impact microtubule dynamics. Future experiments are needed to determine whether the pre-stretch induced surface anisotropy signals microtubule polymerization to cause the axonal thickening observed.

3.3.4 Co-culture of Schwann cells with aligned axons

Schwann cells are able to migrate into areas of damaged central nervous system and remyelinate the demyelinated axons [121]. Since myelination is dependent on the axon thickness and thicker axons are preferentially myelinated, Schwann cells were co-cultured on stretched and unstretched surfaces with 2 week-old cultured and aligned DRG axons for a week (Figure 3.6). The axons were stained for β-III tubulin while the Schwann cells were stained for P0, an indicator of myelination. P0 is a marker of mature Schwann cells and is a component of the myelin sheath. Significant co-localization of green (β-III tubulin) and red (P0) fluorescence occurred on the stretched surface (Figure 3.6b) while on the unstretched surface the red and green fluorescence did not co-localized significantly (Figure 3.6d), The co-localization of β-III tubulin and P0 are quantified in Figure 6e, where the vertical axis represented the percentage of green fluorescence that overlapped with red fluorescence. From Figure 3.6e, the percentage of red and green fluorescence co-localized on the pre-stretched surface was ~80%, indicating the Schwann cells attached and aligned with the axons. In contrast, the percentage of co-localization on the unstretched surface was around 25%, indicating β-III tubulin and P0 did not co-localize significantly on the unstretched surface (Figure 3.6d). Therefore, as demonstrated in Figure 3.6 the pre-stretched surfaces enhanced not only axon alignment and fascicular-like tract formation but also increased the attachment of SCs to the aligned axons, a requisite for myelination.

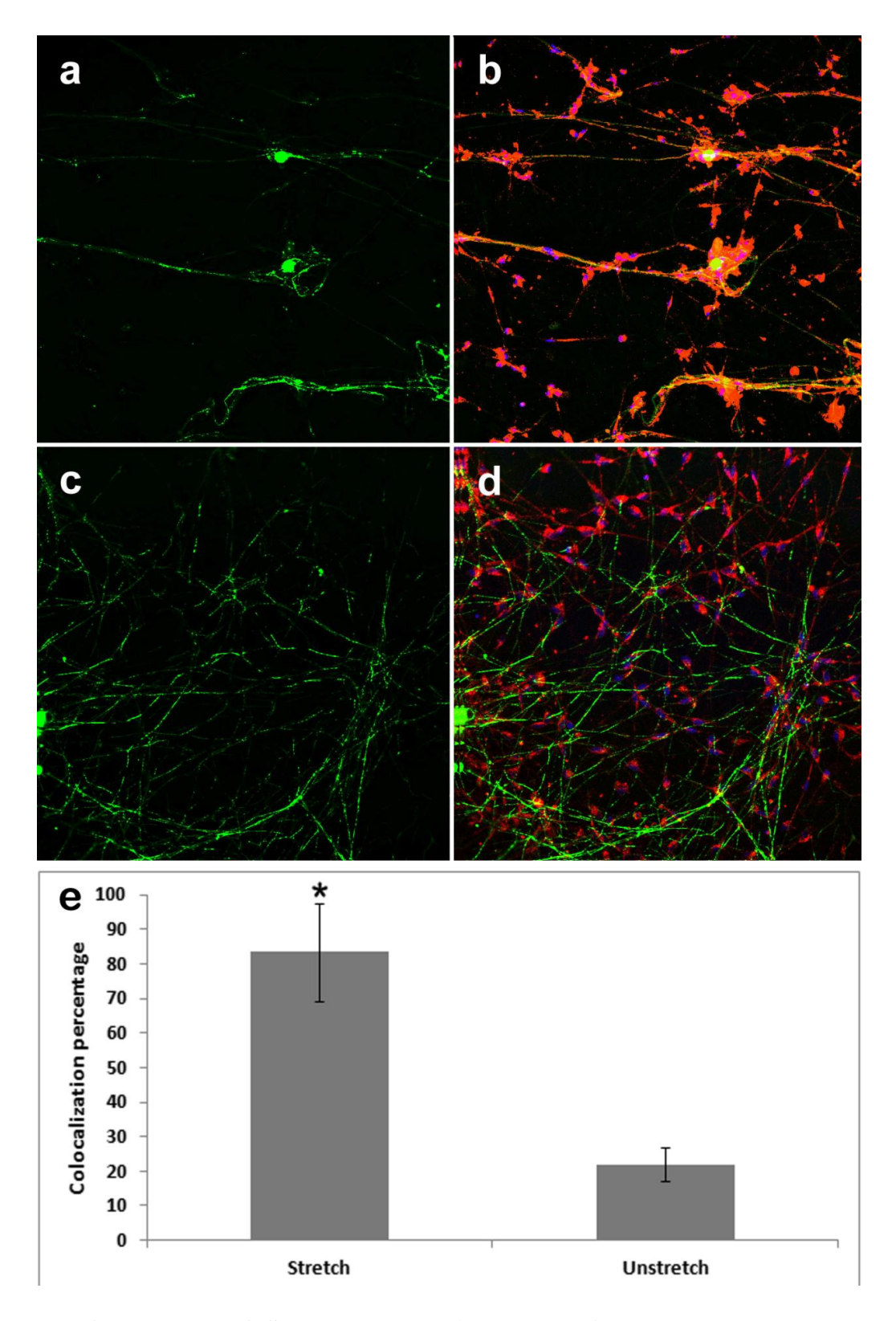


Figure 3.6. Co-cultured of Schwann cells with the DRG neurons on the stretched vs. unstretched PDMS substrates.

(Figure 3.6 cont'd) After culturing the DRG neurons on the stretched and unstretched surfaces for 2 weeks, purified Schwann cells were added to the chamber and cultured for another week. (a) β -III-tubulin (green) staining of axons on the stretched PDMS substrate; (b) Overlay of β -III-tubulin (green), P0 (red) and DAPI (blue) staining on the stretched substrate; (c) β -III-tubulin (green) staining of axons on the unstretched substrate; and (d) Overlay of β -III-tubulin (green), P0 (red) and DAPI (blue) staining on the unstretched substrate. (e) Quantification of the percentage of colocalization (overlap) of β -III-tubulin (green) with P0 (red), using the FV1000 software, for the stretched and unstretched surfaces. *: p < 0.01.

Many studies, using topological features or motor stretch, demonstrated that axons can be induced to align, but they did not explore myelination on the aligned axons [76, 122-124]. Although myelination has been shown with SC and DRG neuron co-cultures, the myelination results in the previous study were achieved by adding growth factors [125]. Oligodendrocytes myelinated axons on randomly oriented electrospun nanofibers of 0.4 μm thickness or larger [126], in contrast, the aligned axons on the pre-stretched surface shown in this study not only myelinated, but also formed thicker axons, all of which are important for nerve regeneration after SCI. Recently Xia *et al.* demonstrated that aligned PMMA nanofibers can enhance the colocalization of DRG neurons with SCs, however, they did not measure myelination [86]. In contrast, our study used P0 staining of SCs clearly indicates myelination of the aligned axons and suggests that the pre-stretched anisotropic surface is capable of enhancing myelination. In contrast, the SCs on the unstretched substrate also stained positive to P0, but with minimal colocalization with β-III tubulin demonstrating the axons were not myelinated. The alignment and attachment of the SCs to the axons suggest enhanced myelination on the pre-stretched substrate

and is likely due to the combined effect of both axon alignment and increased axon thickness. Thus, the ability of pre-stretch induced anisotropic surfaces to guide attachment of SC to aligned axons suggests that surface anisotropy could be capitalized upon to enhance myelination of endogenous axons.

CHAPTER 4 SCHWANN CELLS MIGRATION ON PATTERNED PDMS MICROGROOVED SURFACE

4.1 Introduction

Schwann cells (SCs) are support cells for nerve processes in the peripheral nervous system and are responsible for the production of the myelin sheath [121]. After the injury, SCs migrate into the lesion site to remove axonal and myelin debris, secrete growth factors and promote axon regeneration [127-128]. In peripheral nerve injury, SCs migrate from each end of the severed nerve to align with the basal lamina cable to form bands of B tingner which guide the regenerated axons to the distal site [129]. Improperly regulated SC motility underlies the limited recovery to the lesion site and failure in remyelination. Given the instrumental role of SCs in aiding nerve repair, SC migration has received growing attention in therapeutic applications [127, 130]. Thus therapies to promote sciatic nerve repair, notably nerve guidance channels for transplantation, need to be tailored to enhance SC migration from the host [131]. Approaches that speed SC migration could accelerate peripheral nerve regeneration and thereby lead to more efficient therapies.

Studies of SC migration have informed on scaffold design for neural regeneration, from peripheral nerve injury to spinal cord injury [127, 129]. To improve the alignment of regenerating axons and accelerate the migration of SCs, three-dimensional channels have shown promise [112]. However, due to limited knowledge on migrating SC populations within the channels, there have been few recent breakthroughs in scaffold designs. Numerous *in vitro* studies have focused on controlling SC behavior through contact guidance achieved by micropatterning ECM proteins [95], nano- or micro- fibers [93, 96, 114, 132-133], microgrooves

and channels [87, 94, 134]. However, the majority of studies on microgrooved substrates have focused on SC alignment [94, 134-135], rather than migration.

Studies on SC migration have focused primarily on single cell motility, with one study tracking the migration of a small group of cells over several hours using time-lapse microscopy [87, 136]. However, the cells were isolated from each other with minimal cell-cell interaction and migrated randomly. Furthermore, the study neglected cell proliferation resulting in a model of averaged migration of several individual cells [136]. Thus, it is unclear how this model would inform on the migration of a large proliferating population of cells over a period of days. During neural tissue formation and repair, SCs do not migrate as discrete single cells but as a population of cells over physiologically relevant time and length scales [137-138]. Thus from a practical perspective, a better understanding of the dynamic interactions between a migrating population of SCs and the collective guidance cues from the surrounding environment could provide more relevant insights into neural tissue repair that could influence future designs of transplantable scaffolds [128, 139-140]. Thus, there is a need to understand how large populations of SCs migrate into the injury site, under a complex environment where cell-cell interaction, cell proliferation, and extracellular guidance exert influence [92, 141].

This study investigates a large population of migrating SCs over a period of two weeks. We developed a method to quantify the migration speed of a large cell population while minimizing the confounding effect of cell proliferation. Micropatterned polydimethylsiloxane (PDMS) surfaces of different channel sizes, which served to mimic the topography and orientation of channel structures in transplantable scaffolds [142], were used to investigate the migration of

populations of SCs over two weeks. The migration velocities of the SC populations on different channel sizes were quantified and compared using two methods, one based on a leading edge velocity and a second based on a binary velocity.

4.2 Materials and methods

4.2.1 Materials

The poly-(dimethylsiloxane) (PDMS) substrate was prepared using the Sylgard 184 silicone elastomer kit purchased from Dow Corning (Midland, MI). Borofloat33 4"-Wafer was purchased from WRS Materials (Reno, NV), SU-8 photoresist was purchased from MicropositTM (Marlborough, MA), Poly-D-Lysine, β-D-arabinofuranoside (AraC), Anti-Thy 1.1 antibody (cat. no. M-7898), Rabbit Complement (cat. no. S-7764), and Anti-S-100 antibody (cat. no. S2644) were purchased from Sigma- Aldrich (St. Louis). Heat inactivated Fetal Bovine Serum (FBS) was purchased from Hyclone (Logan, Utah). Bovine Pituitary Extract (BPE, cat. no. CC-4009) was purchased from Clonetics (Allendale, NJ). Forskolin was purchased from Calbiochem (Billerica, MA). Type I Collagenase was purchased from Worthington (Lakewood, NJ). Dulbecco's modified Eagle medium (DMEM), penicillin, streptomycin, 0.25% trypsin-EDTA, 1X-phosphate buffered saline (PBS), HEPES buffer and immunostaining components (Alexa Fluor 546 goat anti-rabit IgG secondary antibody, and DAPI) were purchased from Invitrogen (Carlsbad, CA). Bovine Serum Albumin (BSA) was purchased from US Biological (Marblehead, MA). Rabbit anti-Myelin Protein Zero antibody (cat. no. ab31851) was purchased from Abcam (Cambridge, MA). Silicone inserts with a defined cell-free gap (cat. no. 80206) were purchased from Ibidi (Martinsried, Germany). Mylar films are from InfinityGraphics (East Lansing, MI).

4.2.2 Microgrooved substrate fabrication

Microgrooved substrates were fabricated as previously described [143]. Briefly, patterns were designed in AutoCAD (Autodesk), with 50, 100, 150 µm spacing, in 1x3 cm rectangular sections as shown in Figure 4.1. These patterns were printed on mylar films, which were used as masks to generate selectively polymerized regions on silicon wafers during the photolithography process. Photoresist SU-8 was spin-coated at 2,000 rpm for 40 s and baked at 110 °C for 1 min on a hot plate. Through conventional photolithography, the photoresist was patterned to expose openings on silicon wafers as desired. The alternating grooves and plateaus patterns were then transferred onto PDMS by curing a 10:1 solution of base and curing agent in polystyrene tissue culture dish at 60 °C for at least 2 hours. After curing, the crosslinked PDMS was peeled off and cut at the edges into separated pieces. A substrate was fit into each well of a 6-well plate, which was treated with a PX-250 plasma cleaning/etching system (March Instruments) for 3 minutes at 165 mTorr and 65 sccm flow of O₂. The substrates were subsequently incubated with PDL solutions at 37 °C for 2 hours prior to cell seeding. After the PDL coating, the surface is rinsed with sterile water. A piece of rectangular silicone insert was attached to the flat surface with one side aligning to the end of channels, which was used as a medium holder to maintain initial attachment of the cells within the square area. The medium holder also helped ensure the distance between the cell and channels was 50µm (width of the wall thickness) prior to commencing the migration study. The entire design is illustrated in Figure 4.1.

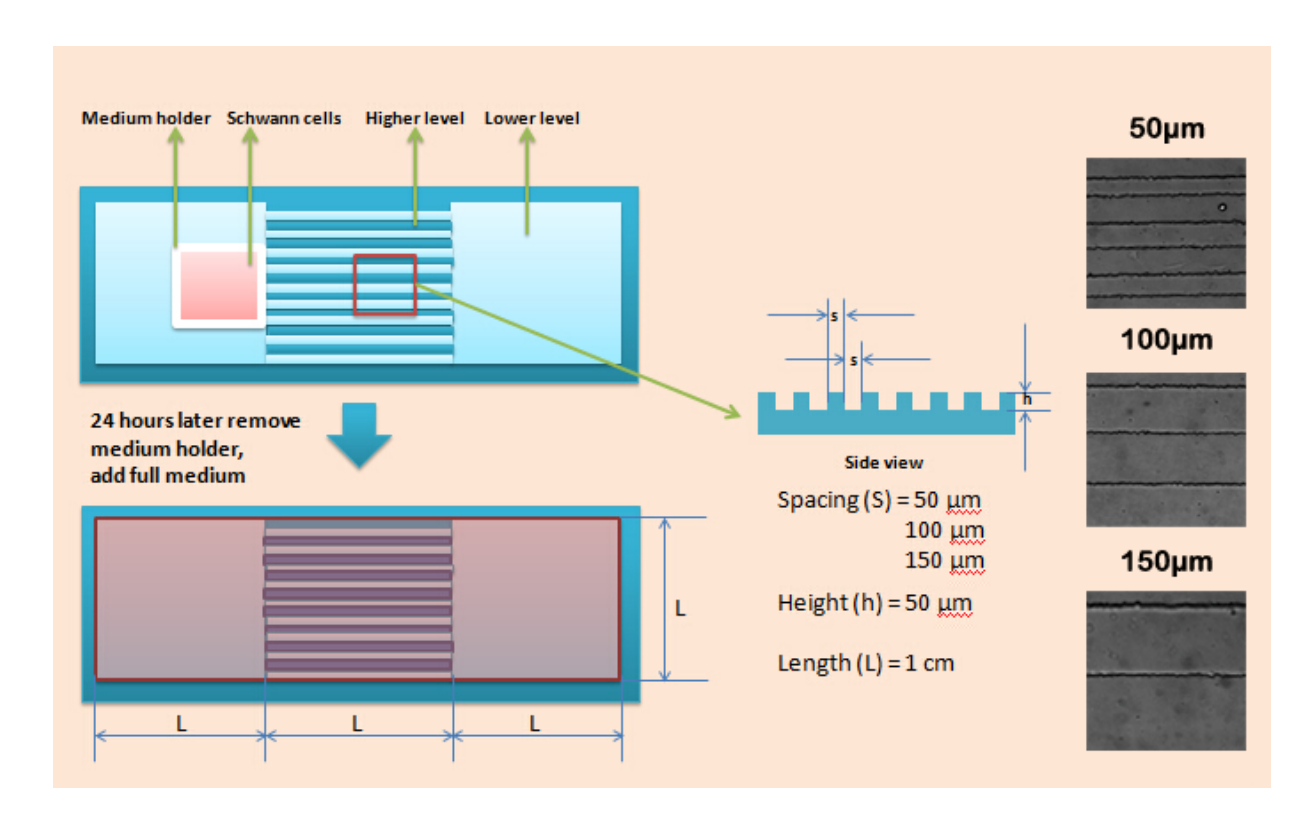


Figure 4.1. Schematic of channel design and PDMS preparation.

PDMS culture substrate consists of channels and two flat surfaces at each end. The flat areas are leveled with the groove and the ridges are $50\mu m$ in height. Both the grooves and ridges are of equal widths. Three different channel sizes, $50\mu m$, $100\mu m$, and $150\mu m$ are prepared. After coating with PDL, a square medium holder is placed at one end of the flat area near the edge of the channels. Schwann cells are seeded in the holder for initial attachment. After 24 hours the holder is removed and the medium is added to the entire surface. Phase contrast images of the three different channel sizes, $50\mu m$ (, $100\mu m$ and $150\mu m$ are shown on the right.

4.2.3 Cell culture

All procedures for cell isolation were approved by the Institutional Animal Care and Use Committee at Michigan State University. Schwann cells were isolated using the same protocol as described previously [105]. One day old pups were sacrificed by decapitation. The sciatic nerves

were extracted by making an incision from the tail up the spine to the inner thigh near the foot. Nerve sections were cut into small pieces and transferred into dissociation medium containing collagenase and trypsin and incubated for 45 minutes at 37 °C. Mechanical dissociation was performed using fire polished glass pasteur pipette. Cells were then centrifuged for 5 minutes and resuspended in DMEM containing 10% heat inactivated FBS and 1% antibiotic (penicillin/streptomycin). Purification procedure begins upon adding AraC into the medium after 48 hours of culture, following by antibody selection using Anti-thy 1.1 antibody and Rabbit Complement on day 5. After purification, the cells were cultured in complete SC growth medium containing DMEM, 10% FBS, 1X Penn/Strep, 21 μg/ml BPE, and 4 μM forskolin and placed in a humidified incubator containing 5% CO2 at 37 °C. The medium was replaced every 2 days until the cells reached 80%-90% confluence. Confluent cells were detached using 0.25% trypsin-EDTA and plated at a density of 100,000 cells per mL with 150μ1 added to each medium holder.

4.2.4 Immunocytoche mistry

Immunocytochemistry was performed at room temperature on cells seeded on the PDMS substrates for 6 days. Cells were rinsed with PBS, followed by fixation with 4.0% paraformaldehyde in PBS for 15 min, rinsed 3 times in PBS, then permeabilized with 0.1% Triton X-100 in PBS for 15 min and washed 3 times with PBS. After washing, cells were blocked in 1% BSA for 30 minutes. After BSA blocking, the cells were incubated with mouse S-100 primary antibody (1µl stock per 500µl of 1% BSA solution) for 1 hour followed by three washes in 1X PBS, and then incubated with anti-rabbit Alexa Flour 546 secondary antibody (1:500 dilution in 1% BSA solution) for 1 hour, followed by three washes of 1X PBS. Confocal

laser scanning microscopy (CLSM) images were obtained with Olympus FluoView1000 laser scanning confocal microscope using a 40X oil objective.

4.2.5 Migration quantification

Figure 4.3 illustrates a flowchart for quantifying the migration velocities. The overall process is presented in Figure 4.3a. Phase contrast images were collected with a Leica DM IL inverted microscope (Bannockburn, IL) equipped with SPOT RT color camera (Diagnostics Instruments, MI) using 10X objective. Image-Pro Plus Version 4.5 was used to process the images. For each set of experiment, images were taken daily of each sample in a grid pattern for the entire 1 cm x 1 cm patterned surface. A grid composed of successive rectangular images, with each rectangular image consisting of 1600 x 1200 pixels or 1212.12 x 909.09 µm, were numbered sequentially by column from end to end of the microgrooves and by row from top to bottom. This grid pattern was used to calculate the distance the cells traveled, by marking the cells in each image by their column and row. For example, image x-y represents an image located in column x and row y. An equivalent distance (e) of image x-y was calculated by multiplying the column number (x) by the length of the image (l).

$$e = x * 1$$

The total cell distance (t) in image x-y was calculated by multiplying the number of cells (n) in image x-y by the equivalent distance (e).

$$t = n * e$$

After generating the grid, the distance a cell traverses was further analyzed using two different methods of calculating migration speed.

1) The leading edge velocity (shown in Figure 4.3b) uses the furthest image in each row which represents the leading edge of the migrating cell population. The total cell distance (T) is calculated as the sum of the total cell distance for each image in the leading edge. The total cell number (N) in the leading edge is a sum of the cell number in each image in the leading edge.

$$T=\sum t; N=\sum n$$

The average cell position (a) in the leading edge is defined by the total cell distance divided by the total number of cells in the leading edge.

a=T/N

By plotting the average cell position with time (days), the migration speed in the leading edge is determined by the slope.

2) The binary velocity (shown in Figure 4.3c) uses a binary counting process which counts whether an image contains at least one cell, yes (1), or not, no (0), by asking "is this the furthest the cells have traversed in this row?" In this case, the total number of cells (N) equals the number of images that are counted as "1" (n1), and the total distance the cells traverses (t) in each image equals the equivalent distance (e).

N=n1; t=e

The total cell distance (T) in the binary analysis is the sum of the equivalent distance of the images counted as "1", and the average distance (a) in the binary analysis is calculated by the total cell distance T divided by the number of images counted as "1" (n1).

$$T=\sum e; a=T/n1$$

The slope obtained by plotting the average distance over time gives the migration speed of the cell population in the binary analysis. The process of generating, analyzing and calculating the

migration speeds from the data using both the leading edge and binary methods for one set of experiment is provided in the supplemental file.

For statistical significance, the experiments were repeated four times. Two-sample student t-test was used to determine statistical significance in Figures 4.4 and 4.5. A p-value of < 0.05 was considered statistically significant.

Quantification of the orientation angles of the cells is described in [91], briefly we counted the number of cells in parallel orientation (90 °±10 °angle) to the channels which was normalized to the total number of cells on each surface. This ratio of cells in the parallel orientation is reported by the mean value plus standard deviation. The two-sample Kolmogorov-Smirnov test was applied to evaluate the statistical significance in Figure 4.6. A p-value of < 0.05 was considered statistically significant.

4.3 Results and discussion

4.3.1 Design of microgrooved substrate

The current microgrooved substrate (Figure 4.1) for cell migration contains two flat areas at each end of the microgrooves that are flush with the grooves, with 50µm high ridges. This design differs from previous studies by enabling SCs to migrate from a flat area onto the microgrooves to the flat area at the other end. The flat areas at the ends permit simulation of SC migration during the repair process, wherein the SCs have to migrate from the host tissue to the injury site through the channels of a transplanted scaffold. In this design, the SCs are initially seeded within a medium holder placed onto one of the flat surfaces to maintain an isolated environment for SC seeding and attachment. After the initial 24 hr of cell attachment, the medium holder is removed and fresh medium is added to cover the entire surface. Different size channels (50µm, 100µm,

and 150µm) with equal sized grooves and ridges (Figure 4.1) were made such that the migration was similar on both the grooves and ridges.

4.3.2 Schwann cells migrated on both the grooves and ridges

After the initial 24 hrs of attachment the SCs initially migrated in all directions across the 50µm distance that is presented upon removal of the medium holder, until the SCs reach the microgrooves, whereupon they migrated directionally on the microgrooved surface. The cells migrated onto both the grooves and ridges (Figure 4.2a), suggesting that the cells must climb onto the 50µm ridge. This is in contrast to previous studies where the SCs were directly seeded onto the grooved surface resulting in random migration in all directions. Confocal fluorescent images in Figures 4.2b and 4.2c show the migrating SCs on the ridges and grooves 2 days after removal of the holder and the start of the migration. The cells were found on the flat area at the other end of the microgrooves; however the majority of cells remained at the start of the grooves. To analyze the migration behavior of the SC population across the channels, we captured images every other day for two weeks until the entire microgrooved surface was covered with SCs.

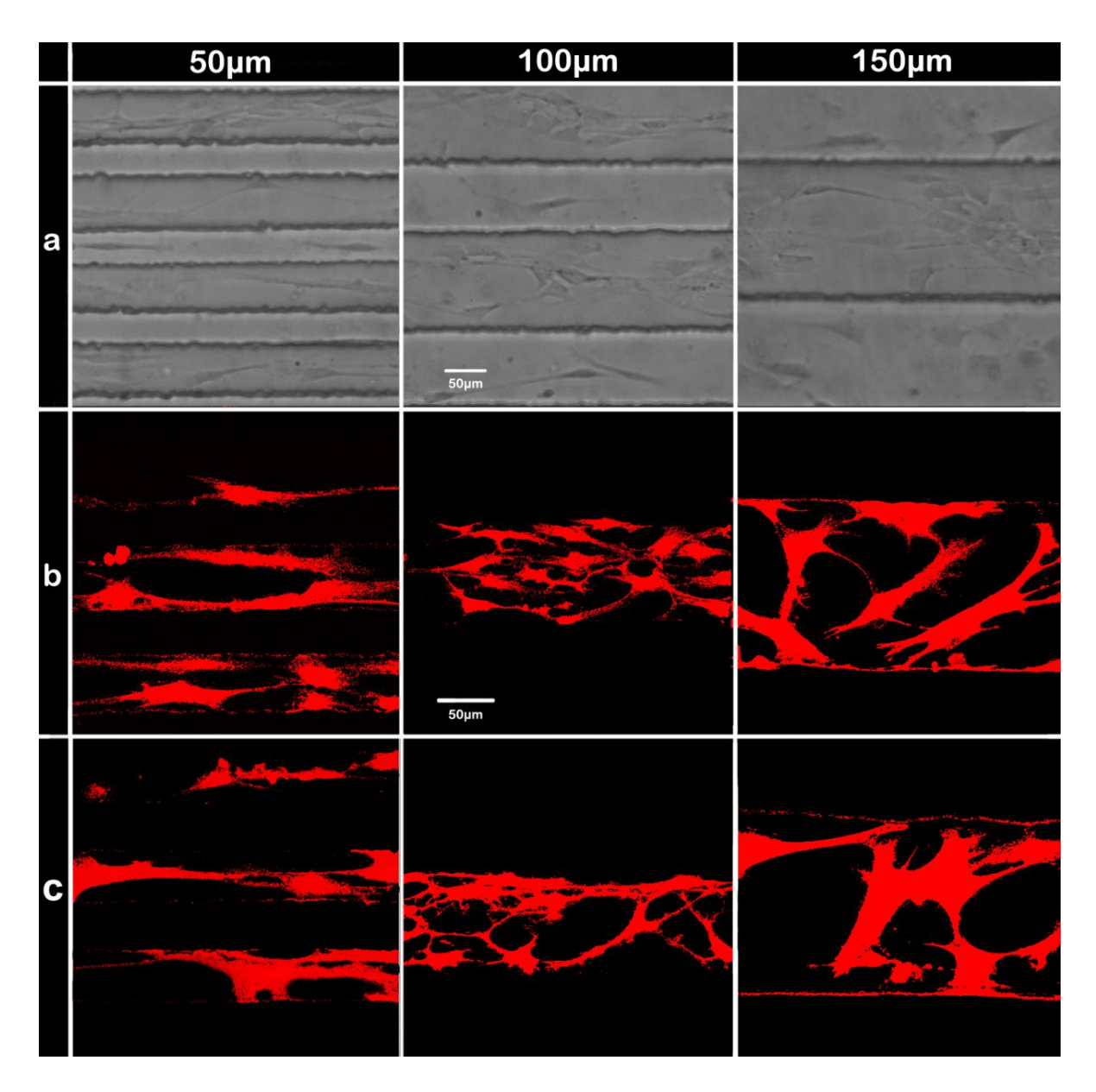


Figure 4.2. Migration of Schwann Cells (SCs) into the channels.

SCs are seeded at one end of the flat area on the PDMS culture substrate, after removal of the holder, the cells migrate into the channels. (a) Phase contrast images illustrate SCs migrate on both microgrooves and ridges. Confocal images specially focused on the ridges (b) and grooves (c). Cells are stained 2 days after removal of the medium holder with S-100 primary antibody and Alexa-546 secondary antibody. Confocal fluorescent images are taken using a 40X oil objective.

4.3.3 Comparison of SC migration on different microgrooved surfaces

Although this study focuses on the migration behavior of SC populations on the microgrooved surfaces over a period of 2-3 weeks, there is significant confounding effect due to the proliferation of the SCs. Therefore, the advancing SC population is the combined result of both SC migration and proliferation. The proliferation is more prominent at the entrance of the channels, while migration predominates at the leading edge of the SC population Thus to minimize the confounding effect due to proliferation, we calculated two different migration velocities, a leading edge, and a binary velocity, based on the distance traversed by the cells. Both methods aim to determine migration while minimizing the effect of proliferation at the backend of the migrating population.

The leading edge is defined as the furthest location that the cells traversed in each row, and indicated by the column number of the image. Figure 4.3b shows a flowchart for the leading edge quantification. To calculate the leading edge migration, only the cells in the grids at the leading edge of the microgrooved surface are counted and the total distance the cells migrated is calculated by summing the total distance traversed by each cell in each image (t) in the leading edge, which is denoted as the total cell distance (T). To calculate the average distance (a) which indicates the average position of the migrating cells in the leading edge, the total cell distance (T) of the leading edge is divided by the total number of cells (N) in the leading edge grid. The average distance (a) is plotted versus time to determine the front of the SC population over time. The slope of the plot provides the migration velocity of the SC population with units of micrometers traversed per day.

The idea behind the binary processing method is that at least one of the cells in this image has traversed that far, but ignores the actual number of cells in the image. Using the binary method which counts images as yes (1) or no (0), the entire grid is converted to a binary field and only the images marked as "1" are selected for further calculation. The average position (a) is calculated by summing the total distance traversed (t) by the cells (i.e. the furthest column number denoted as "1") divided by the number of images counted as 1. This is plotted over time and the slope provides the binary migration velocities of these cells.

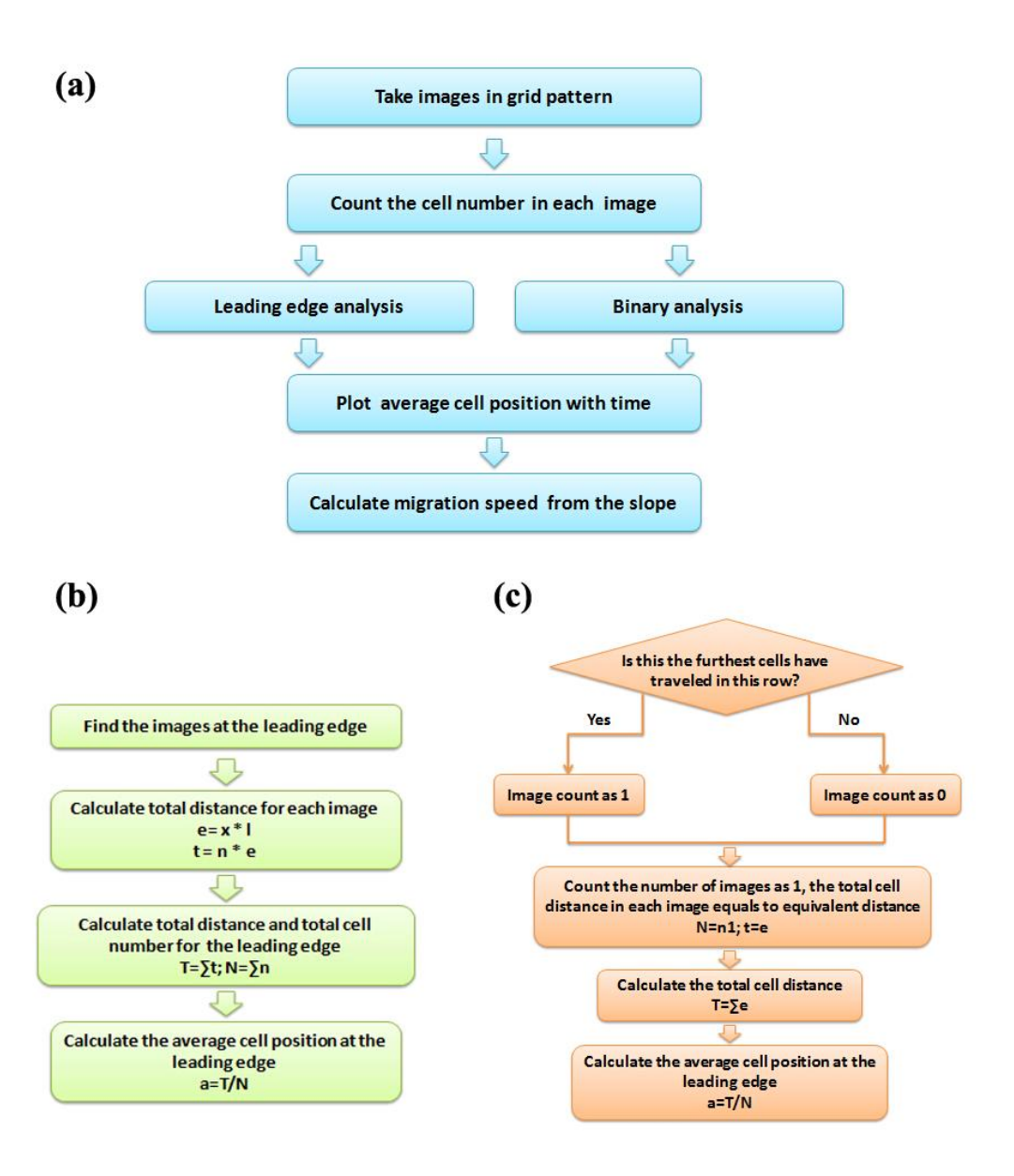


Figure 4.3. Flowcharts illustrating the various steps in the quantification of SC migration speed.

(a) The overall process of obtaining the SC migration speed. The migration of SC into the channels is monitored by capturing images in a grid pattern, and calculating the average position of the leading edge of the migrating SCs. (b) The algorithm for calculating the average position of the binary migration velocity. (c) The algorithm for calculating the normalized migration velocity of the leading edge.

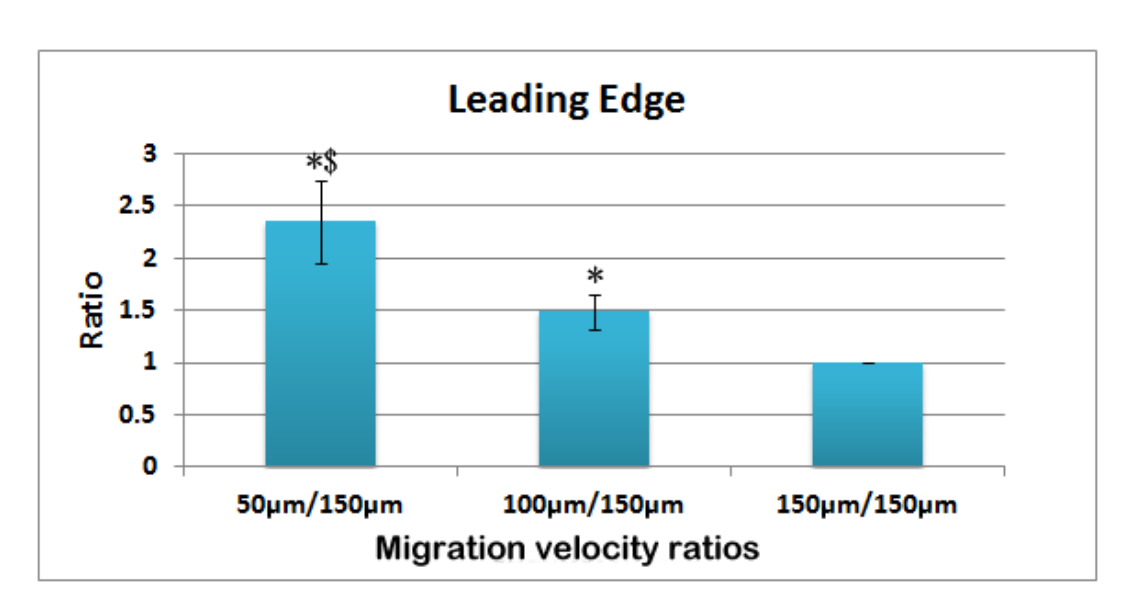


Figure 4.4. Comparison of SC migration in the different size channels using the leading edge velocity.

The migration speed of the leading edge in the different size channels is normalized to the speed in the $150\mu m$ size channels.

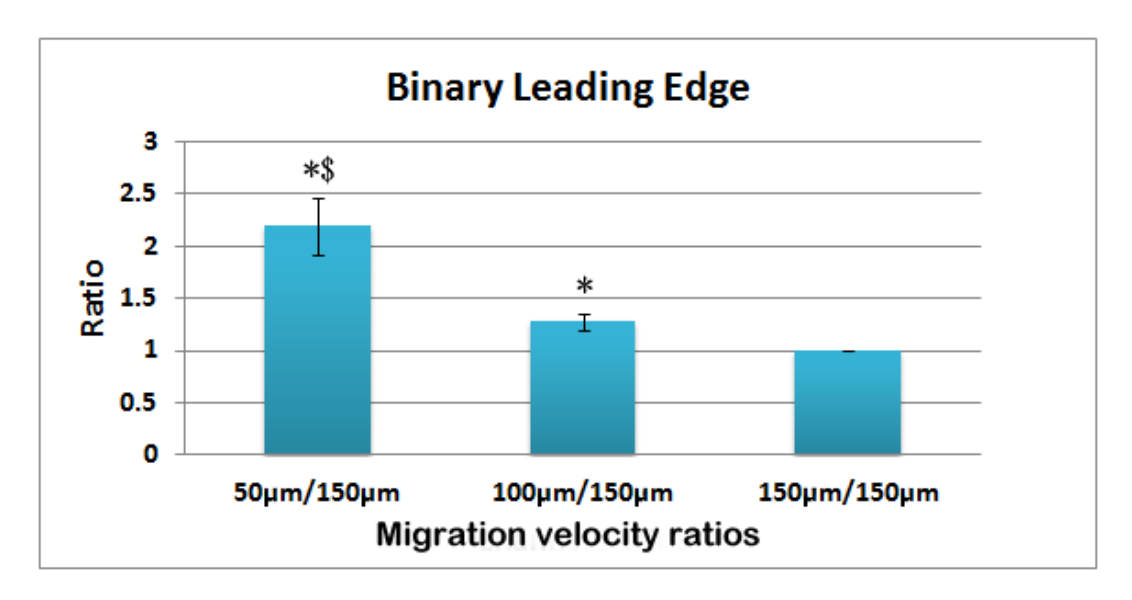


Figure 4.5. Comparison of SC migration in the different size channels using the binary velocity.

The binary migration speed in the different channels is normalized to the speed in the $150\mu m$ size channels.

Figures 4.4 and 4.5 show a comparison of the relative migration on the microgrooved surfaces for three different size microgrooves using both the leading edge and binary processing methods. The average migration velocity shows some variance between the different batches of cells. To minimize the impact of cell batch variance, the ratio of the average migration velocity of each channel size is divided by the migration velocity on the 150 μm microgrooved channel. This ratio indicates how much faster the cells traversed on each microgrooved channel over the 150 μm microgrooved surface. Using both quantification methods (Figures 4.4 and 4.5) the relative migration results show the cells traversed differently along the three different size microgrooves and fastest on the smallest size (50μm) microgrooved surface.

The ratios calculated using the leading edge method differs slightly from the binary method. The calculation based on the leading edge counts the real number of cells located at the leading edge, where the cell number for a grid in each row represents the frequency that the cells traverse a certain distance. Therefore, the results based on the leading edge method indicate how far the cells migrated on the different microgrooved channel sizes. In contrast, the binary method simplifies the actual number of cells in each image with a "yes (1) or no (0)", and indicates how far the cells can migrate on the different microgrooved surfaces. The results from both methods consistently show the fastest SC migration on the smallest size microgrooved surface.

Prior studies investigated the migration of single cells over a few hours [144-145], however, the results do not inform on how tissues within a complex environment of large populations of cells would behave. Recently, an SC migration study on microgrooved surfaces using time lapse microscopy demonstrated anisotropic microgrooved surface promoted cell migration in the

direction parallel to the microgrooves [87]. However, the migration speed was calculated based on the net distance a single cell traversed over several minutes and did not provide clear trends as a function of the microgroove size. Although the study calculated the net migration speed in the direction parallel to the microgrooves, the speed was bi-directional since the cells were seeded directly onto the microgrooved surfaces and migrated in both directions. In contrast, the current experimental design wherein the cells are seeded on a flat area on one side of the microgrooves induced directionality resulting in the migration of the cells to the flat area on the other side. Therefore, this design better simulates a migration behavior of SC population into scaffold channels.

4.3.4 Comparison of SC alignment in different channels

Previous studies indicated that cell morphology is causally linked to cell motility [146-147]. The bipolar morphology of SCs includes a long, spindle shaped soma which is flanked by two thin extensions, rendering them an ideal cell type for migration [148]. The direction of migration follows the long axis of the cell body, therefore the orientation of a cell determines the direction it migrates [149]. We evaluated the SC orientation on the different size microgrooved surfaces and quantified the cell orientation angle after 6 days of culture and calculated the ratios of cells that aligned in the channel direction. Figure 4.6 shows a comparison of the ratio of aligned cells on the different size microgrooved channels and found the ratio of aligned cells on the 50µm channel surface is significantly higher than the 100µm and 150µm surfaces, with the ratio on the 100µm also significantly higher than on the 150µm microgrooved channel. Thus, the cell alignment on the microgrooved surface exhibits a similar trend to the cell migration speed, i.e. both are greatest on the smallest size microgrooved channel.

It was demonstrated that cytoskeletal filaments and focal adhesions align along the edges of subcellular grooves [150], which was explained by the contact guidance that resulted from the mechanical stresses created through cell adhesion [63, 151]. Studies have shown that actin microfilaments and microtubules align parallel to subcellular sized grooves on surfaces [152-154]. Although cell alignment on subcellular sized grooved surfaces has been investigated, none to date have explored the motility of cells on microgrooved substrates with dimensions larger than the cell body, i.e. sizes close to the dimensions of channels in transplantable scaffolds, until this study.

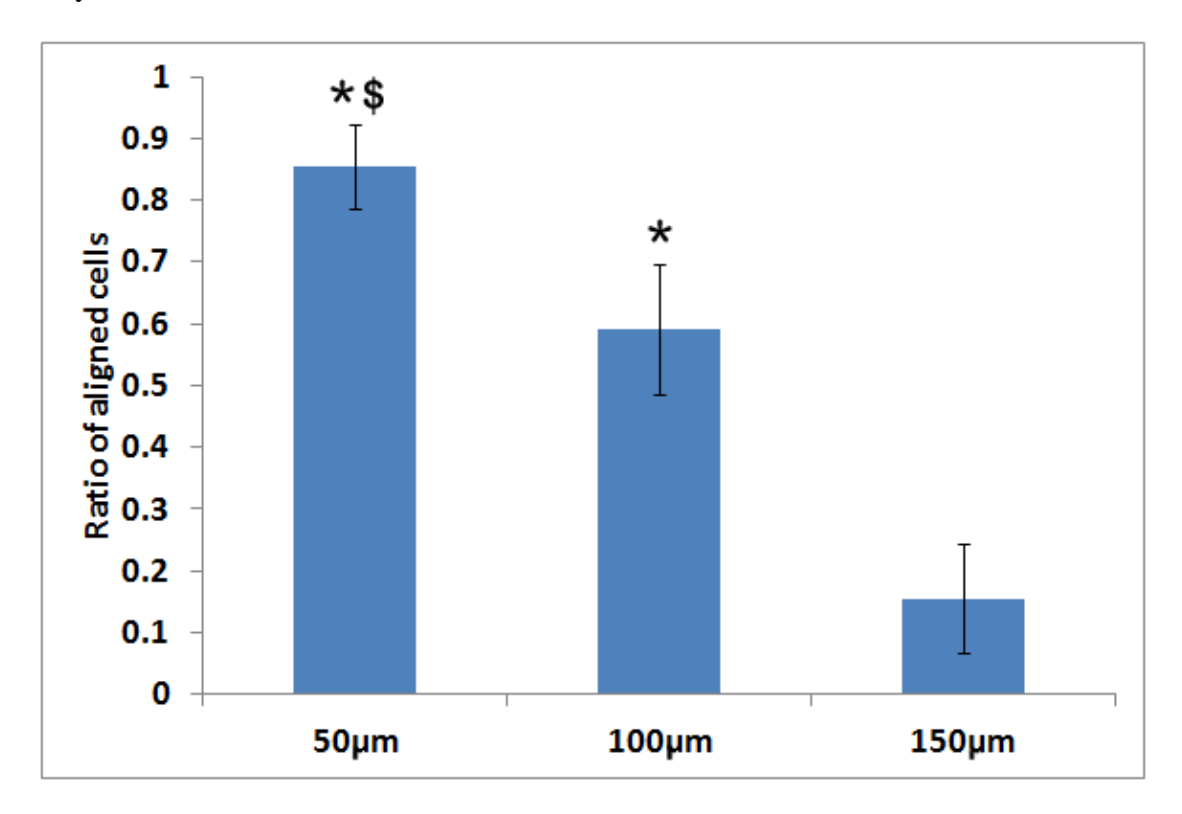


Figure 4.6. Comparison of SC alignment in the different size channels.

The orientation angles of the cells are measured after 6 days of culture on the different channel sizes. The ratios of aligned cells (within a range of $180\pm10^{\circ}$) are plotted for the different channel sizes.

4.4 Conclusion

This study investigated and quantified the cell alignment and migration on large-scale anisotropic topography over a period of weeks. Two strategies were used to calculate the velocity of the migrating SC population. Both methods aimed at minimizing the confounding effects due to cell proliferation, and showed similar trends, i.e. SC population migrated fastest on the smallest size microgrooved surface. These results of the SC migration presented in this study provide insights that could inform on future designs of transplantable tissue scaffolds.

CHAPTER 5 SCS ENHANCE REGENERATED AXONS PENETRATION INTO PATTERNED CHANNELS

5.1 Introduction

In the central nervous system (CNS) and peripheral nervous system (PNS) axons fail to spontaneously regenerate after nerve injury, resulting in permanent deficits of motor, sensory or autonomic function. Nerve regeneration after injury show limited axonal plasticity due to the presence of inhibitory molecules both in the extracellular matrix [155] and in the myelin [156], as well as the lack of appropriate spatial and temporal growth factor gradients to stimulate growth [128, 157].

Bioengineered scaffolds have the potential to enhance the organization of axon growth and guidance through the injury site after spinal cord injury [158-160]. Considerable progress has been made in enhancing the growth potential of injured adult axons, including aligning, lengthening, thickening, and myelinating the axons. Seeded with bone marrow stromal cells expressing neurotrophin-3 (NT-3), templated agarose scaffolds have induced 83% of the axons to penetrate into the scaffolds and grow over a 2 mm distance [20]. We have previously developed a pre-stretched anisotropic surface that successfully induced axon alignment and thickness of dorsal root ganglion (DRG) neurons and myelination [142]. Despite promising demonstrations in animal models, repair of long distance nerve injury with functional recovery is still challenging due to multiple factors, including axonal disruption, growth inhibitory molecules in the scar, lack of growth-promoting molecules, and incomplete remyelination [161-163]. Therefore, treatments to overcome these multiple deficits will require a multifaceted

strategy, i.e. a multifunctional scaffold that can not only enhance axon growth and alignment but also deliver growth factors and promote myelination.

Schwann cells (SCs) are essential to the survival and function of neurons and play a vital role in the PNS by maintaining and aiding in the regeneration of axons [164]. It is known that SCs provide trophic support to promote the growth of axons from developing neurons [165]. The exact mechanism is unknown, however recently evidence suggests that two key factors secreted by SCs, glial cell line-derived neurotrophic factor (GDNF) and NT-3, may play a substantial role in the growth regulatory process of axons [166]. SCs are also known to migrate into the CNS and remyelinate the demyelinated axons after spinal cord injury (SCI). Due to their ability to secrete multiple growth factors, transplanting SCs hold promise as a therapeutic strategy for spinal cord repair [167-168]. Transplanting SC engineered to secrete neurotrophin and chondroitinase enhanced axonal regeneration, and improved locomotor and sensory function [169].

We showed previously that the size of the channels of transplantable scaffolds strongly affects SC migration speed [170]. Here we explore axon growth in channels coupled with the migration of SCs, which offer trophic support to the regenerating axons. We designed a micropatterned channel platform using polydimethylsiloxane (PDMS) and co-cultured DRG neurons with SCs for 21 days to investigate the presence of migrating SC on the penetration of axon into the channels. The effect of SCs on the axons were compared with nerve growth factor (NGF) released from a collagen gel and in different size channels.

5.2 Materials and methods

5.2.1 Materials

PDMS substrates were prepared using an 184-silicone elastomer kit purchased from Dow Corning (Midland, MI). Poly-L-Lysine was purchased from Trevigen (Gaithersburg, MD). Sodium bicarbonate, Poly-D-Lysine, Fluoro-2 deoxy-uridine, Uridine, Cytosine β -Darabinofuranoside (AraC), Anti-Thy 1.1 antibody (cat. no. M-7898), and Rabbit Complement were purchased from Sigma-Aldrich (St. Louis). Heat inactivated Fetal Bovine Serum was purchased from Hyclone (Logan, Utah). Bovine Pituitary Extract (BPE) was purchased from Clonetics (Allendale, NJ). Forskolin was purchased from Calbiochem (Billerica, MA). Type I Collagenase was purchased from Worthington (Lakewood, NJ). Neurobasal Medium 1X, B-27 Supplement, Glutamax-I, Albumax-I, Nerve Growth Factor, Dulbecco's modified Eagle medium (DMEM), penicillin, streptomycin, 0.25% trypsin-EDTA, 1X-phosphate buffered saline (PBS), HEPES buffer were purchased from Invitrogen (Carlsbad, CA). Fluo-4 AM, cell permeant (cat. no. F-14201) was purchased from ThermoFisher Scientific (Grand Island, NY). Bovine Serum Albumin (BSA) was purchased from US Biological (Marblehead, MA). Rabbit anti-Myelin Protein Zero antibody (cat. no. ab31851) was purchased from Abcam (Cambridge, MA). Mylar films were from InfinityGraphics (East Lansing, MI). Type I collagen (cat. no. #354236) was purchased from Corning (Corning, NY).

5.2.2 Patterned channel cell co-culture system fabrication

The entire design is shown in Figure 6.1. The micropatterned PDMS channels are prepared as previously described in Chapter 5, with two squares cut closely along with both ends of channels as an open area to seed cells. In order to create a sealed channel environment, the side of channel

pattern is facing down and tightly attached to the PLL coated polystyrene substrate. Crosslinked collagen gel (375 μ l type I collagen + 27 μ l NaHCO₃ + 50 μ l DMEM) was used as a glue to seal the edges, which helps to prevent the cells to be flushed outside the channel system.

5.2.3 DRG neuron and Schwann Cell isolation and culture

All procedures for cell isolation were approved by the Institutional Animal Care and Use Committee at Michigan State University.

DRG neurons are isolated from 5-8 day-old Sprague-Dawley rats as described in Chapter 3. Briefly, after sacrificing the pups by decapitation, the skin overlying the spinal cord is cut away and any excess tissue is removed from the spinal cord. The spine is then completely removed from the body, and the spinal cord is extracted. Using a fine pair of tweezers and a pair of microsurgery scissors, approximately 10-16 DRGs are collected from both sides, trimmed of nerve roots and transferred to 5 ml of ice-cold HBSS buffer containing 1 ml penicillin/streptomycin. The dissection medium containing DRGs are then transferred into a new 15-ml tube, centrifuged at 900 RCF at 4 ℃ for 5 minutes. After centrifugation, the supernatant is removed and the DRGs are incubated in 6 ml of 0.05% Trypsin-EDTA (1X) (Sigma; 1 mg/ml, 45 min) at 37 ℃ and followed by 2 ml collagenase (Sigma; 500 U/ml, 20 min) at 37 ℃. After chemical dissociation, the ganglia are centrifuged at 900 RCF in 4 °C for 5 minutes and the supernatant is subsequently removed. The pellet is further resuspended in 10 ml of standard growth media and centrifuged, as described above. After washing with the medium, the cells are resuspended in standard growth media containing Neuralbasal A medium containing B-27 supplement, antibiotic (penicillin/streptomycin), Albumax-I and nerve growth factor. The

dissociated neurons are then plated onto the PLL coated pre-stretched surface and incubated at 37 C at $5\% \text{ CO}_2$.

Schwann cells were isolated using the same protocol as described previously [105]. One day old pups were sacrificed by decapitation. The sciatic nerves were extracted by making an incision from the tail up the spine to the inner thigh near the foot. Nerve sections were cut into small pieces and transferred into dissociation medium containing collagenase and trypsin and incubated for 45 minutes at 37 °C. Mechanical dissociation was performed using fire polished glass pasteur pipette. Cells were then centrifuged for 5 minutes and resuspended in DMEM containing 10% heat inactivated FBS and 1% antibiotic (penicillin/streptomycin). Purification procedure begins upon adding AraC into the medium after 48 hours of culture, following by antibody selection using Anti-thy 1.1 antibody and Rabbit Complement on day 5. After purification, the cells were cultured in complete SC growth medium containing DMEM, 10% FBS, 1X Penn/Strep, 21 µg/ml BPE, and 4 µM forskolin and placed in a humidified incubator containing 5% CO2 at 37 °C. The medium was replaced every 2 days until the cells reached 80%-90% confluence. Confluent cells were detached using 0.25% trypsin-EDTA and plated at a density of 5,000 cells per mL with 100µ1 added to the cut open square.

5.2.4 Fluorescent imaging

The penetration of axons into channels was visualized through fluorescent live cell imaging, by adding 1µl of Fluo-4 into each well and incubate the cells at 37 °C for 30 mins. Fluorescent images were taken by a Leica DM IL inverted microscope (Bannockburn, IL) equipped with SPOT RT color camera (Diagnostics Instruments, MI) using a 10X objective.

5.2.5 Pre-loaded collagen gel with NGF

The collagen gel was prepared by adding 10% reconstruction buffer (4.77g HEPES, 2.2g NaHCO₃ and 0.2g NaOH in 100ml H2O) and DMEM into type I collagen solution to achieve a final concentration of 2 mg/mL collagen, the mixed gel was then incubated at 37 °C overnight to crosslink. NGF was reconstituted to 100 mg/ml in sterile phosphate buffered saline (PBS, Sigma). To pre-load NGF into collagen gel, 20μl of NGF stocking solution was added into 1ml collagen gel before crosslinking.

5.2.6 Quantification of axon penetration depth

The axon penetration depth is defined as the furthest position the axons reach in each condition on each size channel. To quantify the axon penetration depth, a stage micrometer was first placed on objective to measure the diameter of the field viewed in eye pieces. The axon penetration depth was quantified under the microscope according to the diameter and the size of channels. All the numbers are estimated values down to tens. 5 batches of biological replicates were quantified with each batch containing at least 4 identical replicates for each condition and each channel size.

5.2.7 Statistical analyses

Data were expressed as a mean \pm standard deviation. ANOVA-Tukey's test was applied to assess for significance in Figure 5.3, 5.4 and 5.5. In all cases, p values of <0.05 were considered statistically significant.

5.3 Results and discussion

5.3.1 Design of the patterned channel cell co-culture system

We co-cultured DRGs and SCs at opposite ends of the micropatterned channels and evaluated different size channels ($50\mu m$, $100\mu m$, $150\mu m$, and $200\mu m$) as shown in Figure 5.1c. Freshly isolated DRGs were seeded at one end of the channels so that the cell bodies attached to the open area. As the axons grew and reached the start of the channels, they begin to penetrate into the channels, whereupon SCs were seeded at the other end of the channels to provide growth factors and migrate to the axons. As a positive control, in lieu of SCs, collagen gel pre-loaded with NGF was added at one end of the channels as shown in Figure 5.1d, which provided growth factors to the axons extending from the other side. As a negative control, the one end of the channels, previously seeded with SCs or coated with NGF-containing collagen gel, was left blank (Figure 5.1b).

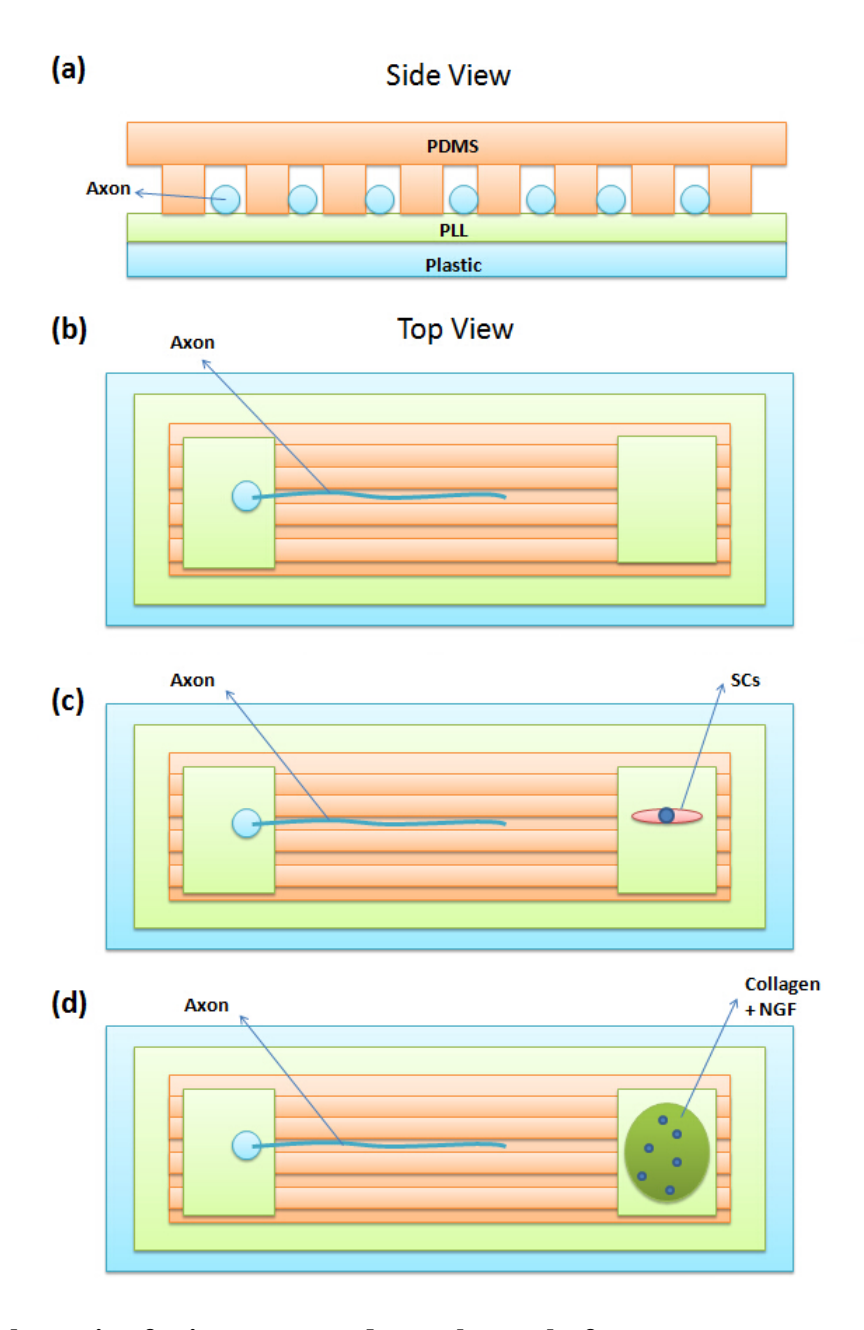


Figure 5.1. Schematic of micropatterned co-culture platform.

(a) Side view of the sealed channels. Polystyrene substrate is coated with a thin layer of PLL prior to overlaying the micropatterned PDMS. The sides of the channels are flush with the substrate to ensure a sealed channel environment for the axons to penetrate. (b) Top view of the platform. Freshly isolated DRG neurons are seeded in the open area at one end of the channels, with the regenerated axons penetrating into the channels. The open area on the opposite end of

(Figure 5.1 cont'd) the channels is left empty in the negative control group. (c) As the regenerated axons reach the end of the channels, SCs are seeded at the other end of the open area to promote axon penetration. (d) Collagen gel pre-loaded with NGF is alternatively added to the other end of the channels as a positive control.

5.3.2. Axons penetration into patterned channels

Figure 5.2 shows the regenerating axons penetrating into the channels towards the SCs or NGF loaded collagen of 21 day-old culture of DRGs. The Fluorescent images were illustrated by Fluo-4 live staining, which stained the calcium channel of live cells [171]. The axons penetrated into the channels and aligned in the channel direction. In the smaller size channels (50 and 100μm), single axons aligned straight and penetrated the channels, while in the larger size channels (150 and 200μm), multiple axons penetrated but with some degree of curvature. In the SC group, some of the SCs are shown in the images indicating that they had migrated from the other end and through the channel to the DRG. In the 150μm channels, the axons appear to cluster together to form fascicular-like bundles.

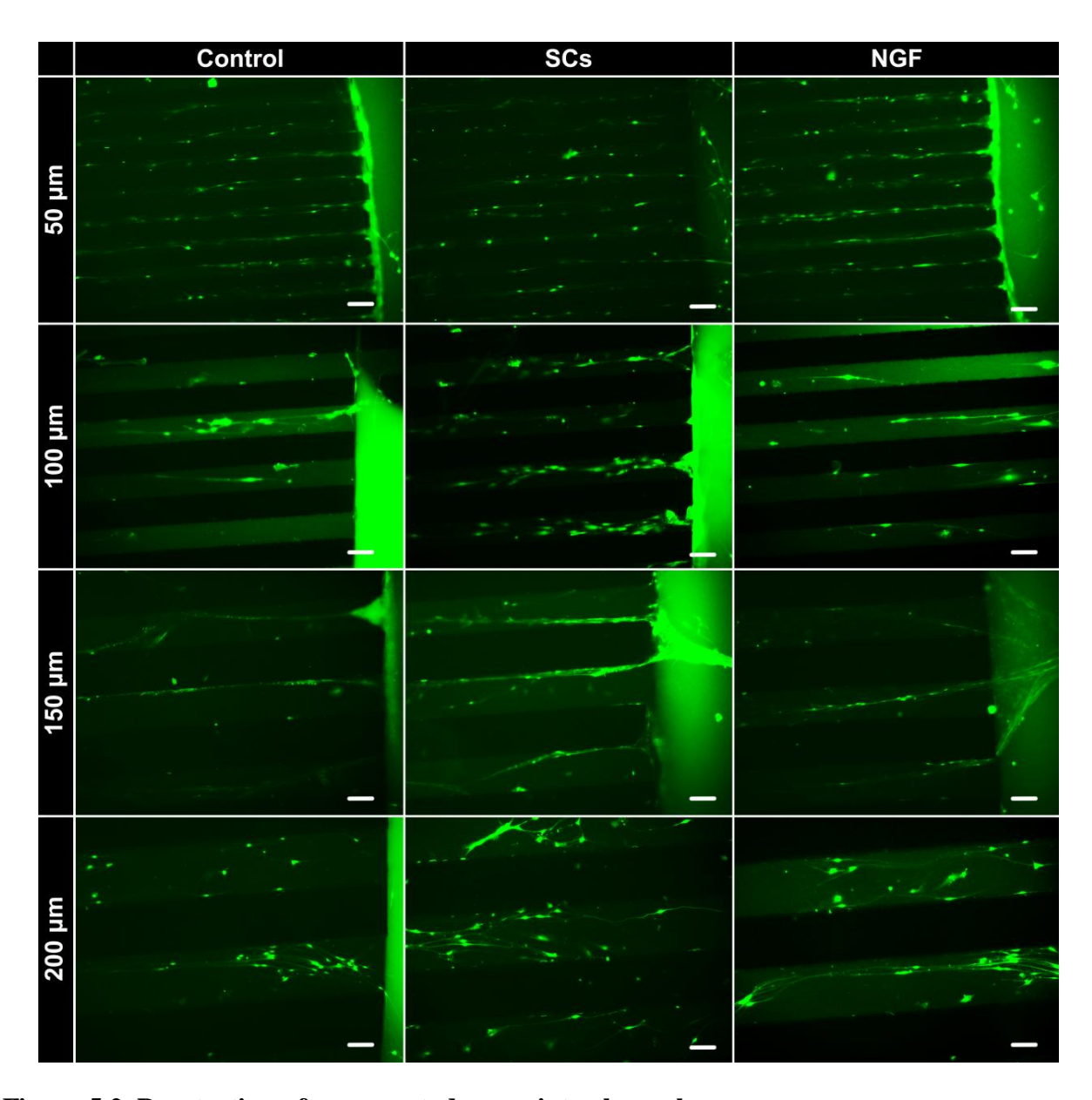


Figure 5.2. Penetration of regenerated axons into channels.

Freshly isolated DRG neurons were seeded in the open area, around 5 or 6 days later as the axons reached the channels and begin to penetrate into the channels, SCs were seeded in the open area at the other end. Collagen gel pre-loaded with NGF was used as a positive control. After 21 days of culture, fluorescent images were taken by Fluo-4 live staining using a 10X objective. Scale bar indicates $100\mu m$.

5.3.3 Comparison of axon penetration depth under different conditions

Figure 5.2 shows the axons successfully penetrated into the channels. Next we quantified the penetration depth after 21 days of culture, and compared among each group (including all the channel sizes) as shown in Figure 5.3. From the comparison results, both SC group and NGF group are significantly higher than the control group, indicating SC addition enhances axons penetration into the channels.

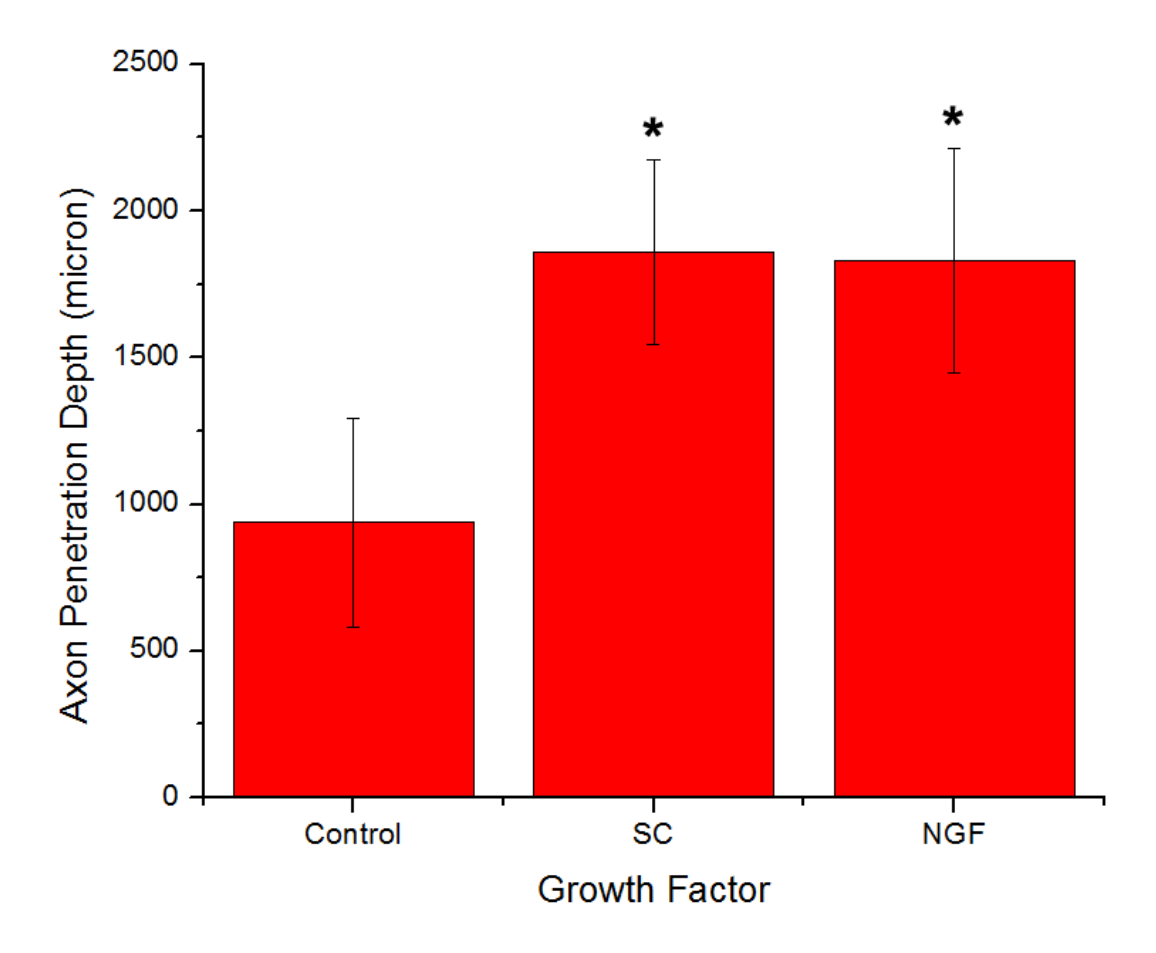


Figure 5.3. Quantification of axon penetration depth.

Comparison of penetration depth with all three conditions across all the channel sizes. ANOVA-TUKEY's test, * > control, p-value < 0.05.

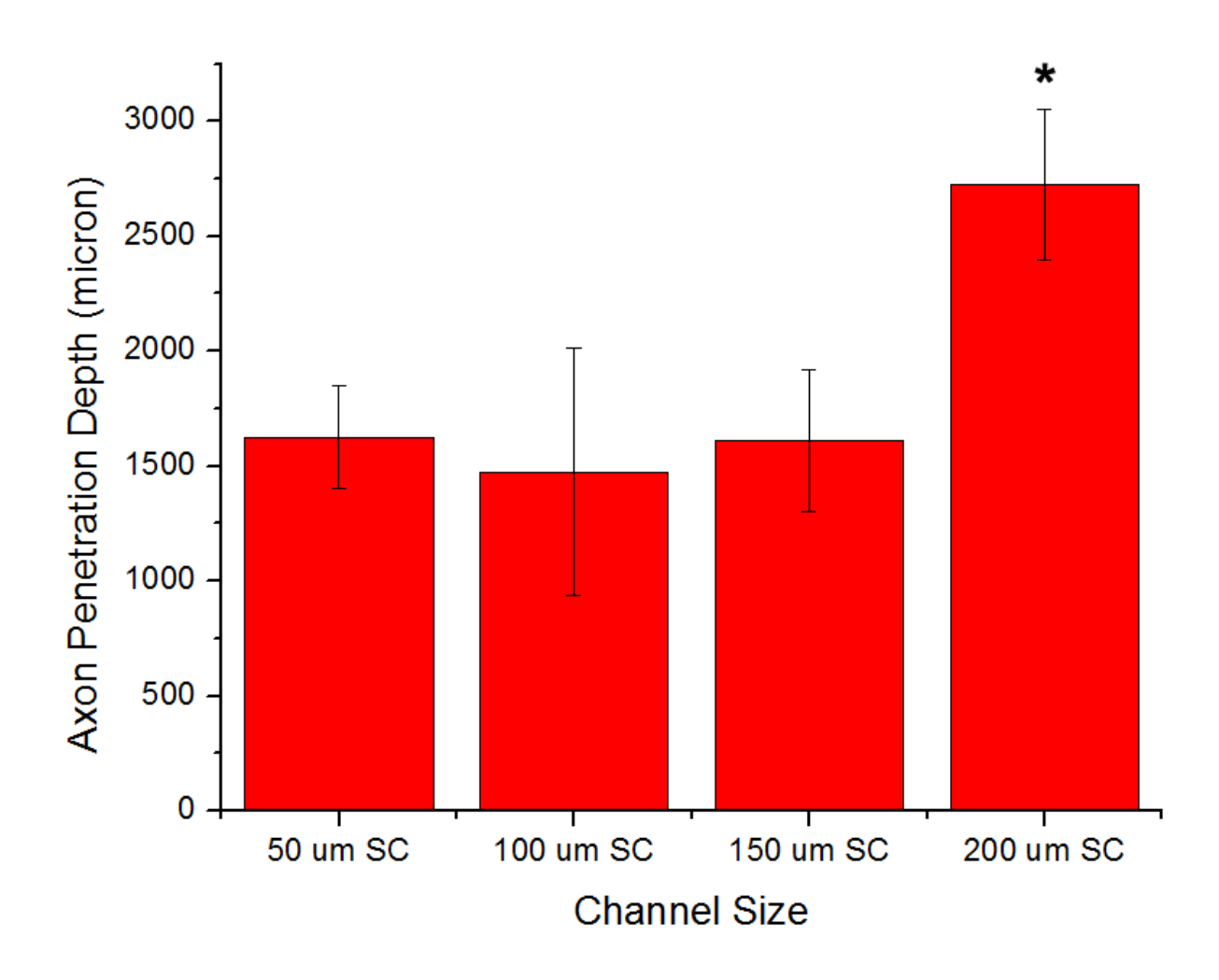
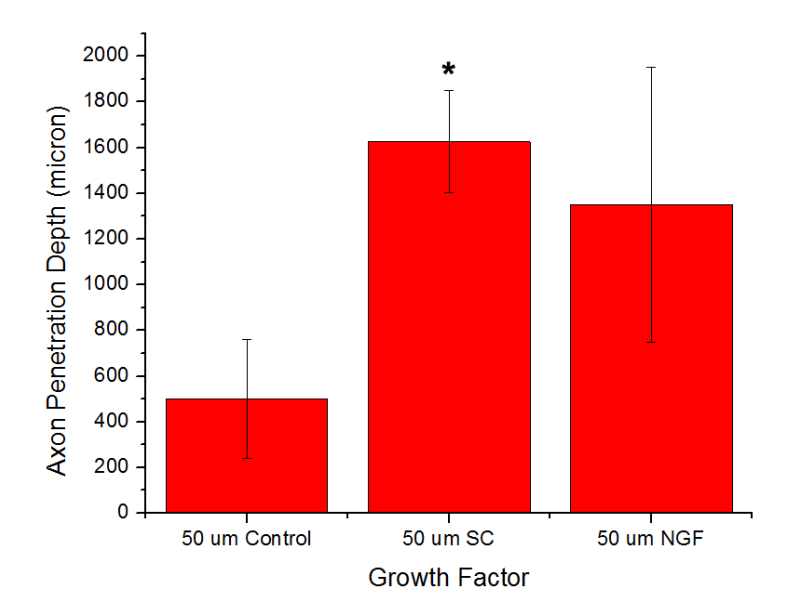


Figure 5.4. Comparison between different channel sizes in SC group.

Axon penetration depth in SC group in different sized channels. ANOVA-TUKEY's test, * > 50 μ m, p-value < 0.05.

(a)



(b)

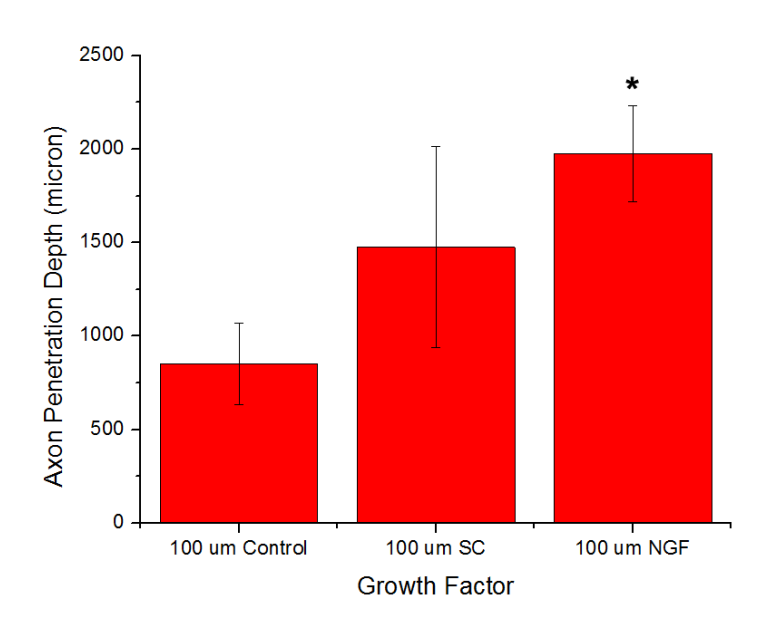
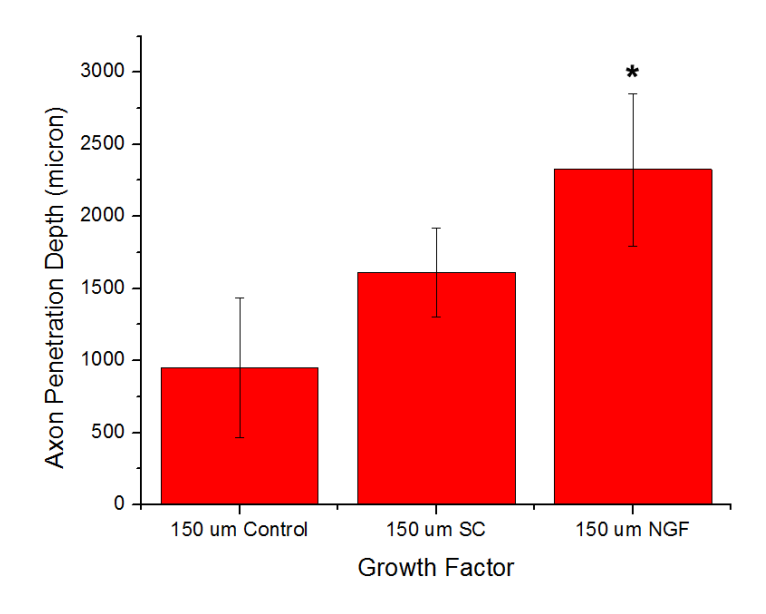


Figure 5.5. Comparison of SCs group with positive and negative control groups for each channel size.

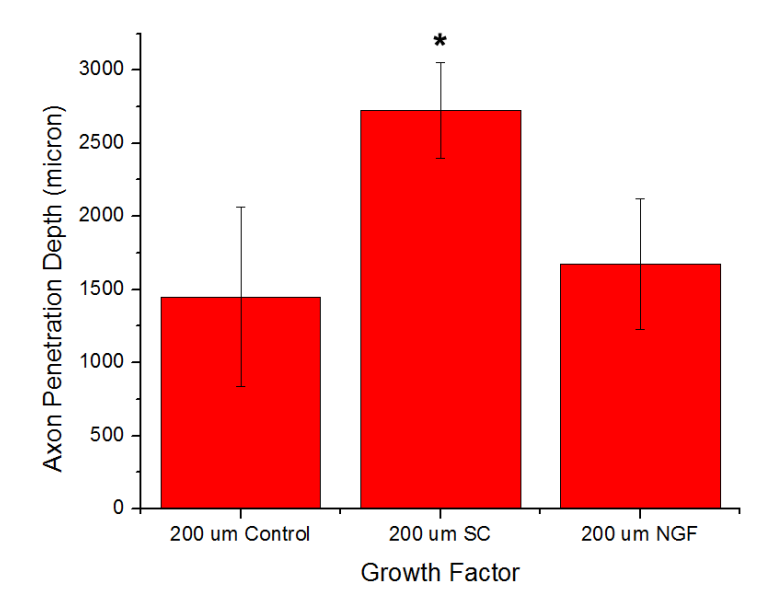
Axon penetration in (a) 50 μ m, (b) 100 μ m, (c) 150 μ m, and (d) 200 μ m. ANOVA-TUKEY's test, * > control, p-value < 0.05.

(Figure 5.5 cont'd)

(c)



(d)



Both the SC and the positive control group show much longer axons than the negative control group for all four channel sizes (Figure 5.3). However the difference between the SC and positive control group is not significant, but nevertheless differs with the channel size (Figure 5.4). The addition of SCs minimized the effect of channel size. The results indicate that the

addition of SCs or the NGF encapsulated gel effectively promote the penetration of the axons into the microchannels as compared to the negative control. Findings from this study could inform the future transplantable scaffold design for nerve repair.

The addition of SCs offers two main advantages. First SCs are known to secrete growth factors that are beneficial to axon growth, and second migrating SCs decreases the diffusion distance to the axons thereby accelerating the delivery of the secreted growth factors. However, it is important to regulate the timing of SC addition since SCs could hamper the growth of the axons due to competition for nutrition as well as secretion of factors inhibitory to axon growth. Therefore, an ideal transplantable scaffold should be able to inhibit SCs from migrating towards the axons until after the axon growth period is completed. However, the scaffold should attract SCs towards the axons after their growth period to thereby myelinate the axon. To enable better control of SC migration, LbL self-assembled multilayers could be used to provide sandwich layers of compounds to repel and attract the SCs [88].

CHAPTER 6 CONCLUSION AND FUTURE WORK

6.1 Summary

The objective of this study was to design and characterize engineering approaches to promote both axon regeneration and SC migration. The first part of this study introduced the concept of pre-stretch induced anisotropy and created a pre-stretching device to induce axon regeneration and myelination. In the second part, we explored SC migration in micropatterned channel surfaces and evaluated the relationship between migration speed and channel size.

Chapter 2 and 3 demonstrated a novel approach to induce surface anisotropy through static prestretch, based on the finding that cells can sense and orient in the direction of maximum stiffness. This concept can be used to induce both stem cell differentiation and axon growth. Chapter 2 reported on MSC alignment on a statically pre-stretched surface which induced and differentiation without any addition of exogenous factors. In Chapter 3 we applied the same concept of pre-stretch induced anisotropy and extended the approach to promote axon alignment. We demonstrated that static pre-stretch induced anisotropy induced DRG neurons to form neatly aligned fascicular-like axon tracts. By showing the co-localization of SCs with the aligned axons and expression of myelin sheath component protein, we concluded that pre-stretch induced surface anisotropy is beneficial to enhancing axon alignment, growth, and myelination. The axon fascicles on the pre-stretched surface in vitro may be directly harvested and transplanted in vivo. Alternatively we could build this idea of pre-stretch induced anisotropy into future scaffold design for transplantation. However, due to the non-biodegradable property of PDMS, if prestretch is incorporated into transplantable scaffolds, alternative biodegradable materials are needed before *in vivo* application of the technology can be attempted.

Chapter 4 explored the extended migration of a large population of SCs on micropatterned channel surfaces with different channel sizes. We developed two methods to quantify the migration speed of a large cell population while minimizing the confounding effect of cell proliferation. The migration velocities of the SC population on different channel sizes were compared and the migration speed with respect to channel size was calculated. The results from both methods consistently indicate that a smaller size microgrooved surface channel accelerated the migration of SCs, which is be an important design variable to consider in transplantable scaffolds. This study simulated a migration behavior of SC population into empty scaffolds, and could be explored in transplantable scaffolds to determine whether the observations observed *in vitro* on cell migration translates *in vivo*.

Chapter 5 investigated the axon growth into channeled scaffolds combined with SC migration by co-culturing DRG neurons with SCs on micropatterned channels. This co-culture system aimed to mimic transplantable scaffolds *in vivo*, where axons penetrate into the channels and at the same time SCs migrate into the injury site to myelinate the axons. The results showed the presence of migrating SCs enhanced the axon penetration depth into the channels, independent of the channel size. An interesting finding is that axons bound together to form fascicular bundles in the 150µm channels, which was not observed in other size channels. Further study is needed to explore this fascicular behavior and test the myelination of axons.

6.2 Future perspectives

6.2.1 The penetration of axons into collagen filled 3D channel scaffold

One of the biggest challenges that emerged in the application of transplantable scaffolds is the transition from 2D to 3D design. Apart from a limited number of studies on 3D environment, it remains a major challenge to mimic the real 3D *in vivo* environment. One option is to fill the sealed channels with 3D gels such as collagen or other ECM components, however we found the axons had difficulty penetrating into the gel filled channels. Therefore, further research is needed to modify the design of 3D channels and manipulate the experimental variables to enable the axons to penetrate into the gel.

6.2.2 The incorporation of pre-stretch with channel scaffold

Chapters 2 and 3 characterized the pre-stretch induced anisotropic surface and investigated its ability to control cell behavior including stem cell differentiation and axon regeneration. In chapters 4 and 5 the migration of SCs and its impact on axon regeneration in patterned channels were explored. Thus a future study could combine the pre-stretched surface with patterned channels to create a pre-stretched anisotropic cell culture system with microchannels that possess multiple functions. The pre-stretched surface enhances axon alignment and thickness, while the migrating SCs in the patterned channels promotes axon penetration, therefore a pre-stretched anisotropic microchannel cell culture system could be developed to promote neatly aligned axons that penetrate into channels, with thicker axons that bind together to form fascicles and SCs to fulfill myelination. This idea can be designed in two ways, first is to place a micropatterned channel piece on the flat pre-stretched surface such that the effects of the pre-stretch and channels are combined, which acts as a transient design to compare with the previous studies. In

the second design the patterned microchannels will be directly pre-stretched without flat substrate. In this case, further mechanical engineering is required to provide an even stretch to the channels, and more features, i. e. cover piece, are need to ensure the sealing of the system, the medium diffusion in the channels, and the seeding of cells. In both cases, the SC migration into patterned channels on pre-stretched surface would need to be measured, such as the axon length, thickness, as well as fascicular behavior and myelination.

Investigating pre-stretched anisotropic microchannels would provide insight into the future development of transplantable scaffolds for nerve regeneration. These *in vitro* results will provide valuable information into the design of pre-stretched into a channel containing scaffolds for transplantation, i.e. the degree of pre-stretch, the size of channels. Figure 6.1 depicts a schematic of a pre-stretched microchannel both for *in vitro* optimization and future *in vivo* transplantation.

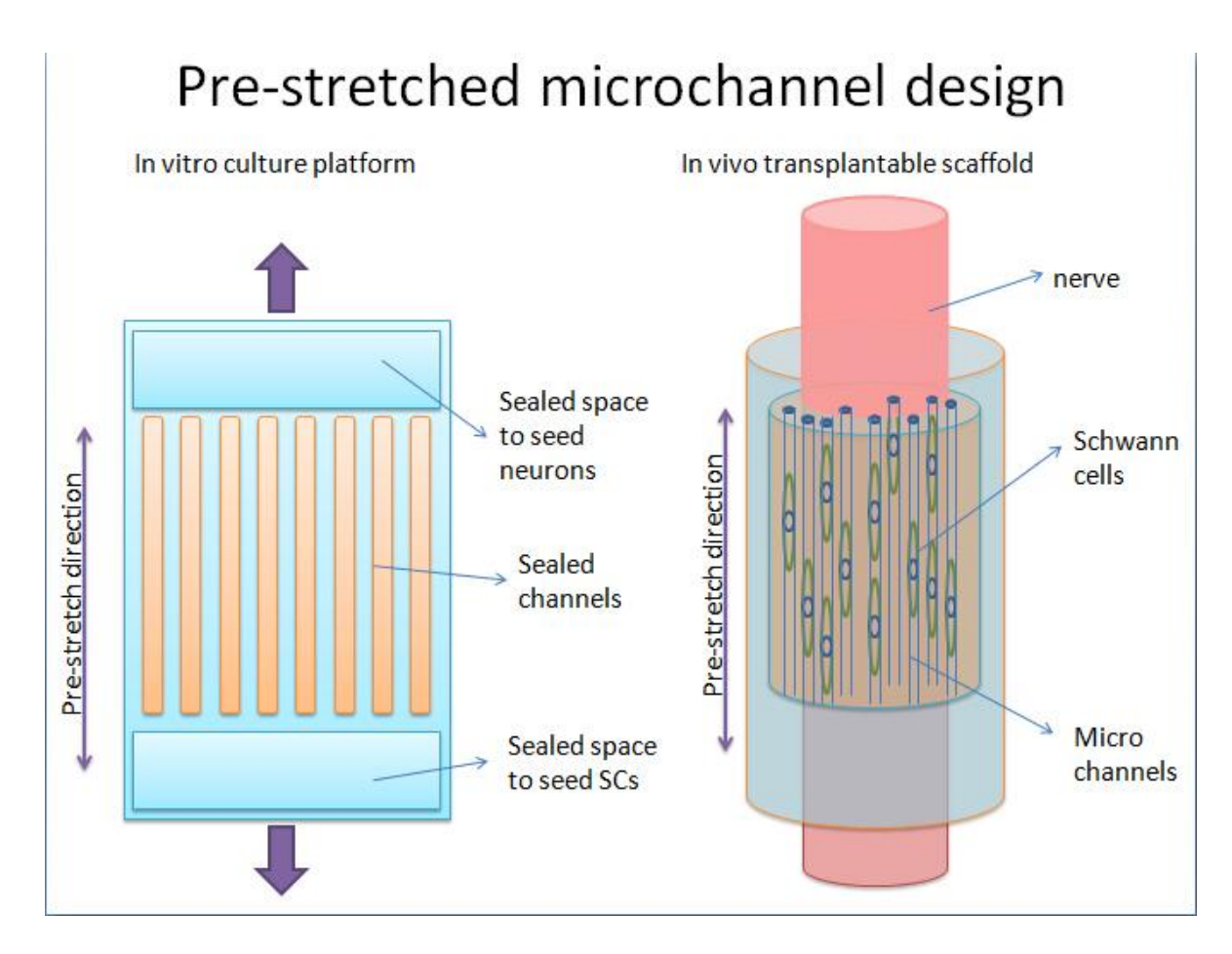


Figure 6.1. Schematic of pre-stretched microchannel design.

The left side shows a design of the *in vitro* study for parameter optimization. Microchannels are sealed in the center area with two flat spaces for seeding the neurons and SCs at opposite ends. The whole cell culture platform could be pre-stretched. The right side shows a future design of transplantable pre-stretched microchannel scaffold.

6.2.3 The applicability of the Layer-by-Layer technology on transplantable scaffold design

In recent decades, PEMs have been employed in tissue engineering, regenerative medicine, and drug delivery applications [172-174]. Simply by altering the pH [175], ionic strength [176], thickness [177], and post assembly modifications [178], researchers have successfully

manipulated the chemical, physical, and topographical properties of these multilayer structures [179]. Their highly tunable properties render them a wide range of abilities in modulating cellular behaviors. Therefore, LbL coated scaffolds could be designed to not only assist cell adhesion and axon guidance, but also deliver drugs locally to promote nerve regeneration and remyelination after SCI (Figure 6.2). In this section we report on studies that modulate the chemical and physical properties of PEMs for tissue engineering applications as well as recent research efforts using PEMs to maintain and direct neural regeneration after SCI. An important aspect that has not been examined extensively is the application of PEMs in enhancing myelination; therefore we close with a perspective on the incorporation of PEMs to enhance myelination through transplantable scaffolds.

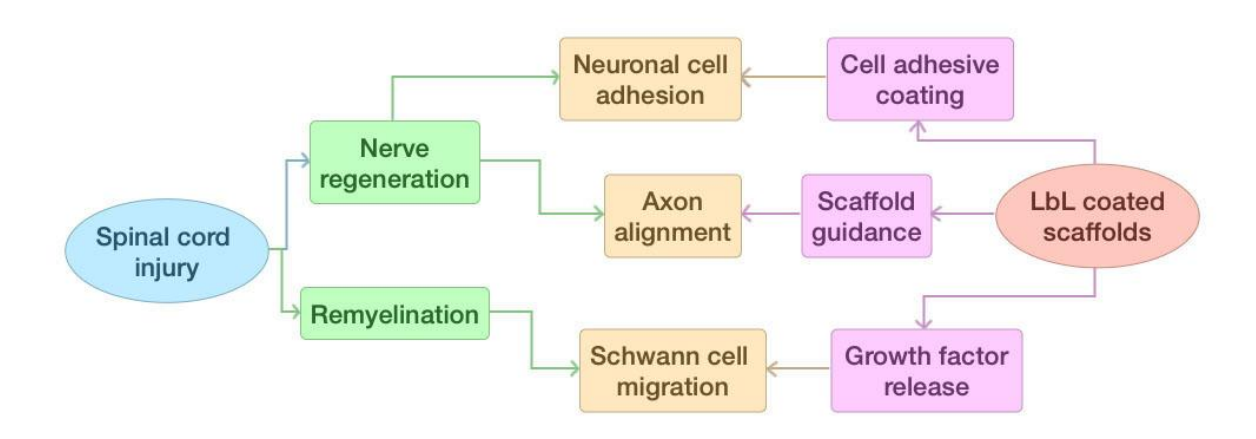


Figure 6.2. Applicability of the LbL technology for SCI repair.

Two major problems after SCI are nerve regeneration and remyelination. Neuronal cell adhesion and axon alignment are required for nerve regeneration, and Schwann cell migration is required for remyelination. LbL-coated scaffolds could address both issues by providing cell adhesive properties, axon guidance, and growth factor release.

It is well known that cell-substrate adhesion is essential for tissue regeneration. The interaction between the adherent cell and its microenvironment ultimately determines cell fate. On an artificial substrate, such as a scaffold, cell adhesion involves the following steps: (1) initial attachment, (2) cellular probing and sensing, (3) cytoskeleton organization, and (4) focal contact formation [104]. To enhance tissue integration, biomaterial surfaces can be modified with adhesion molecules that mimic the ECM to promote cell attachment. Upon attachment, the cells actively pull on the substrate and sense the response of the substrate, which causes the cells to modulate the cytoskeleton organization and thereby the cell shape and orientation. The resultant focal adhesion triggers intercellular signaling pathways that impact cell morphology, attachment, function, viability, and proliferation [180]. Incorporating a monolayer or multilayer coating of adhesion molecules or surface charge has been a standard method for enhancing focal adhesion formation, which leads to desired tissue integration with the scaffold [181].

Over the last decade, the layer-by-layer (LbL) technique has been more frequently applied to generate PEM surfaces which contain bioactive molecules to support living tissues [172-173, 182]. In particular, PEMs have been extensively explored as a coating to modulate cell adhesion. PEM films with strong cytophilic as well as cytophobic properties have been successfully constructed [183], as well as films that can reverse their adhesive properties from being cell repelling to cell binding [184]. These developments hold promise for designing transplantable scaffolds with more versatile and diverse capabilities.

The LbL technique produces nanoscale coatings by sequential adsorption of polycationic and polyanionic materials. The initial layer of deposition of either polycation or polyanion is dependent on the substrate charge. Since each adsorption step reverses the charge on the surface,

alternating the deposition of positively and negatively charged compounds leads to a self-assembled bilayer structure, stabilized by strong electrostatic forces [185-186], that can be tuned to achieve a desired number of bilayers with specific thicknesses [187-188]. Although the construction of LbL multilayers is mainly driven by electrostatic attraction between the positively and negatively charged compounds, other types of forces i.e. hydrogen bonding, hydrophobic interactions and van der Waals forces may also be employed to build LbL films. These forces have been found to affect the stability, morphology, as well as thickness of the films [189]. Since most of the biomaterial and adhesion molecules are inherently charged, they can be readily incorporated into the LbL process.

Factors essential to LbL film formation, their mechanical properties and stability include the pH, concentration, and ionic strength of the polyelectrolytes used in building the bilayers. Different adsorption parameters, such as pH, salt concentration, and the number of bilayers impact the intrinsic properties of the PEM films, such as their surface roughness, stiffness, the degree of hydration, and thickness, which subsequently determine the ability of the cells to adhere onto the surface [183, 190-191]. The thickness of PEM films depends on the ionic strength, however, this dependence can be modulated by salt-induced phase separation of the polyelectrolyte complexes [192]. The growth of the LbL films can be either linear or exponential, mainly depending on the polyelectrolytes used as well as the number of bilayers applied [193-196], whereby the resulting film thickness largely affects the adhesive behavior of the cells on the PEM films [190-191, 197-198]. For linearly growing multilayers the thickness increases with the number of bilayers and can result in a shift in the cell adhesion behavior. Increasing the number of bilayers of poly(diallyldimethylammonium chloride) (PDAC)/sulfonated poly(styrene) (SPS) from 10 to 20, corresponding to a film thickness of ~ 38 to 96 nm, respectively, altered the film from being

cytophilic to cytophobic [57], highlighting the versatility (i.e. easily controlled cell adhesive properties) of these self-assembled PEMs.

Compared to traditional coating approaches, PEM films have many advantages: (1) the LbL process and equipment are relatively simple and easy to apply; (2) they are suitable for coating almost all charged surfaces; (3) there are abundant natural and synthetic colloids with an intrinsic charge that can be used to build bilayer complexes; (4) their flexibility to conform to any surface facilitates coating of nanometer thickness on irregular shapes and sizes; (5) the assembly and disassembly of the coating is easily controlled; and (6) the desired thickness is easily regulated by the number of multilayers deposited [172, 185-186, 199-202]. Thus they can be applied to virtually any charged substrate, attesting to their adaptability to transplantable devices for tissue engineering applications. However, the long term stability of LbL films *in vivo* is still dubious, as even minor changes in pH can alter the film structure resulting in instability of the films [203-204]. Nevertheless, the instability induced by pH change could be addressed by cross-linking the polyelectrolyte layers either chemically or through photo-coupling [205-207].

There is growing interest in incorporating bio-recognition moieties into tissue engineering constructs. As such, LbL coatings can readily incorporate ECM components onto tissue engineering scaffolds. ECM molecules, such as collagen and laminin, known to promote axonal regeneration, neural cell differentiation, adhesion, and migration in the CNS [208], can be easily incorporated into PEMs for these purposes [209]. Compared to other techniques for creating biomaterial-adhesion molecule composites, such as blending [210] and surface deposition [211], electrostatic and covalent bonded polyelectrolyte bilayer complexes can produce much stronger and more stable structures [212]; providing a better approach.

In addition to native biomolecules and peptides, non-native proteins and peptides have been used to promote neural adhesion. For example, poly-L (D)-lysine (PLL, PDL), known to enhance neural cell adhesion, proliferation, and neurite elongation [213], can form electrostatic bonds, due to their positive charge, with the negatively charged cell membrane to assist cell adhesion [214]. Capitalizing on this, researchers have designed PEM films using PLL or PDL as the polycations and as the terminated layer, which showed excellent cell adhesive properties [8, 184, 215-216]. Besides polypeptides, natural polyelectrolytes including nucleic acids, proteins and polysaccharides, such as, alginic acid, chondroitin sulfate, heparin, chitosan, HA, cellulose sulfate, and dextran sulfate have been used to build PEM films [217-219].

The LbL technique has proved to be an attractive means of incorporating functional molecules that can enhance neural cell adhesion. In contrast to adhesion studies of cortical neurons and neural stem cells, adhesion of glial cells i.e. oligodendrocytes and Schwann cells, to PEM films has not been extensively investigated. One study found that scaffolds coated with laminin enhanced adhesion of the Schwann cells to the surface [220]. The incorporation of Schwann cells into scaffolds for SCI could aid neurite regeneration as well as remyelination [17]. Given their flexibility and ease of application, the LbL technique could be exploited for incorporating ECM molecules as well as growth factors into PEM coated scaffolds to enhance Schwann cell adhesion and growth, and remyelination of axons.

LbL coatings have been applied to tissue engineering constructs, e.g. implantable scaffolds, to enhance cell adhesion [221]. However, in a preponderance of studies, PEMs were deposited on silicon or glass substrates [222-223], rather than transplantable scaffolds or biomaterials. In

addition, compared to the extensive studies of endothelial cells and fibroblasts, which are used as models to study cellular adhesion, proliferation, and cytotoxicity [200, 224], studies of neural cell adhesion have been relatively few. Thin films composed of laminin/Poly-D-lysine (PDL) or fibronectin/PDL bilayers with poly(styrenesulfonate) (PSS)/ poly(ethyleneimine) (PEI) multilayers as precursor film have been assembled on silicone rubber substrate to increase the hydrophilicity of the rubber surface. These ultra-thin films (bilayer thickness 3.5-4.4 nm) enhanced adhesion of primary neurons, without apparent cytotoxicity [225]. Similarly, nanoscale PEI-laminin films constructed on oxide covered silicon wafers also showed significantly enhanced chick cortical neuron adhesion and differentiation without deleterious effects on the impedance of the electrodes [226]. These findings suggest that ultra-thin LbL coatings lend themselves well to supporting neural activity recording. Wu et al. demonstrated that LbL assembly of hyaluronic acid (HA) based films, mimicking ECM, deposited on aminofunctionalized glass slides successfully supported hippocampal and cortical neuron cell adhesion, neurite extension and network formation [197]. Kotov's group reported neural stem cell adhesion and differentiation on LbL coated carbon nanotube (CNT). They demonstrated both cell adhesion and early differentiation of neural stem cells on PEI/ single-walled carbon nanotubes (SWNTs) films, as indicated by positive staining for neuron marker MAP2 [7]. Similarly, heparin/poly-L-lysine (PLL) multilayers built on electrospun PCL scaffolds provided enhanced adhesive properties for neuronal progenitor cells to attach and furthermore coating the PLL terminating layers with BDNF enhanced neurite outgrowth [8]. Studies using LbL as a coating to enhance neural adhesion are summarized in Table 6.1.

Table 6.1. LbL application in neural adhesion

Year	LbL films	Cell type	Outcome	Reference
2003	$ [PSS/PEI]_3 + [fibronectin/PDL]_4 \\ [PSS/PEI]_3 + [laminin/PDL]_4 $	Primary neurons	Cell adhesion and neuronal network development	Ai et al. [225]
2005	[laminin/PEl] _n	Cortical neurons	Cell adhesion and differentiation potential	He et al. [226]
2006	[HA/poly(allylamine hydrochloride) (PAH)] _n [HA/collagen (COL)] _n	Hippocampal neurons Cortical neurons	Neurite length decreases with bilayer number	Wu et al. [197]
2007	[SWNT/PEI] ₆	Neural stem cells	Cell adhesion and differentiation potential	Jan et al. [7]
2008	[heparin/PLL]₅	Neuronal progenitors	Cell adhesion and improved neurite branching	Thouas et al. [227]
2011	[heparin/PLL] _n +BDNF	Neuronal progenitors	Cell adhesion and improve neurite length	Zhou et al. [8]

To mimic the organization and complexity of nerve tissue architecture, not only are cell-surface interactions with the scaffold important but also cell-cell interactions. Patterned co-cultures of multiple cell types have been employed to mimic the micro-environment through spatial localization of different cell types [228-229]. Among the approaches to generate patterned co-cultures, micro-contact printing has been frequently applied to selectively adhere different cell types to specific regions, facilitated by patterned surface molecules [230-232]. Similarly, LbL films have also been used to fabricate patterned surfaces of cell co-cultures [85, 233].

Neural regeneration requires neuron-glial cell interactions [234]. This requires selective growth of neuronal processes, and well-controlled surface properties could facilitate the necessary cell-cell interactions. With a high-aspect-ratio, axons are very responsive to topographical features,

such as substrate curvature and fiber diameter [235-236], which can be manipulated to promote their growth. Glial cells (astrocytes and oligodendrocytes) have their own requirements for adhesion and growth. Neurons and glial cells function as interdependent networks, and there exists bidirectional communication between these cells [237-238]. Thus, it is important to mediate the intercellular communication during nerve regeneration after SCI. An approach to guiding neural regeneration could be through engineering spatial organization of the adhesive molecules on a substrate that is selectively permissive to either neuron or glial cell adhesion. Indeed patterned co-cultures of neurons and astrocytes were achieved using LbL incorporated microcontact printing, where the neurons attached to areas coated with SPS, followed by subsequent seeding and attachment of the astrocytes on areas coated with PDAC as shown in Figure 6.3 [85]. Since glial cells are an abundant source of soluble factors which impact neuronal cell growth [239], spatially organized co-culture of neurons and glial cells could be engineered to provide a favorable environment for neuron growth.

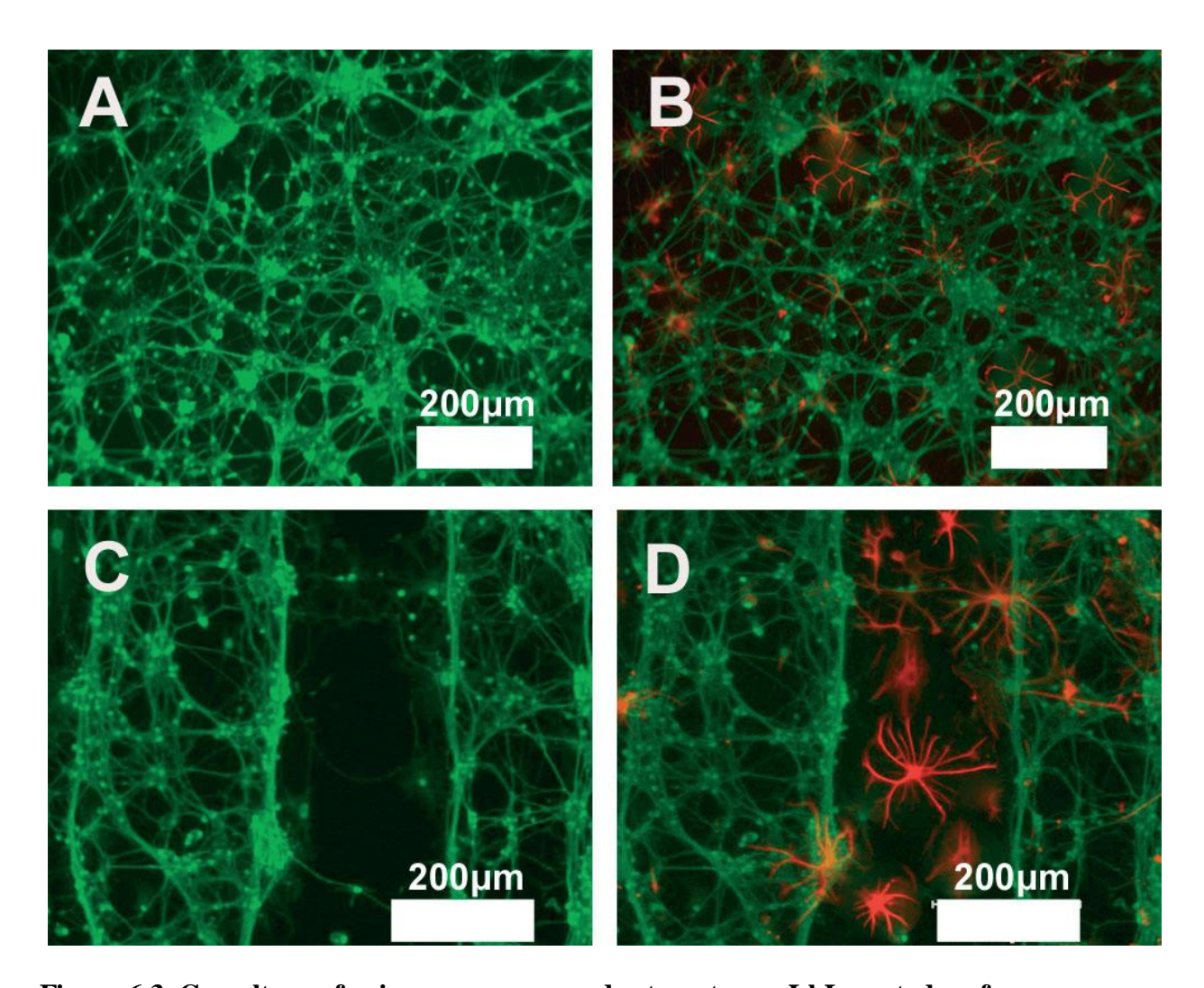


Figure 6.3. Co-culture of primary neurons and astrocytes on LbL-coated surfaces.

(a) Monoculture of neurons on non-patterned SPS surface. (b) Co-culture of neurons and astrocytes on non-patterned SPS surface. (c) Primary neurons on patterned surface. (d) Co-culture of neurons and astrocytes on patterned surface (Scale bars: 200 μm). Neurons were labeled with neurofilament staining (green), and astrocytes were labeled with glial fibrillary acidic protein (GFAP) staining [100]. (Reproduced with permission from Ref. [100]. Copyright Wiley-VCH Verlag GmbH & Co. KGaA.)

In addition to cell adhesion applications, PEM films with tunable drug delivery capabilities have engendered much interest and hold promise as a versatile coating for implantable devices and tissue engineering scaffolds. A variety of biomolecules such as antibiotics, cytokines, and growth factors, when incorporated into PEM films, have been able to retain their bioactivity [88, 240-241]. A drug delivery system utilizing PEMs offers promise for implantable devices, ranging from preventing infection [242] to delivery of growth factors to enhance tissue regeneration [243]. *In vivo*, hybrid LbL films coated on three-dimensional scaffolds have been shown to release microgram-level of Bone Morphogenetic Protein 2 (BMP-2) over a period of two weeks. The released protein was capable of directing the native progenitor cells to differentiate into bone [244]. In general, drugs can be integrated into PEM films through a variety of forces such as pH-induced ionic attraction, electrostatic interactions, or covalent bonding. Thus, the drug release can be controlled by manipulating the environment through changes in the pH, ionic strength, and temperature [189].

Over the years the application of LbL drug delivery has shifted from non-degradable to degradable films. The non-degradable systems relied on diffusion of chemicals of low molecular weight from the films. The loading of drugs on these films can be easily controlled by varying the number of layers. However, the diffusion controlled drug release from these non-degradable LbL films could only be sustained for a few hours. Typically a "burst" profile is associated with these non-degradable LbL [245]. Using degradable synthetic polymers in LbL films overcame the initial burst limitation and produced a more linear release profile. These release rates could be tuned by controlling the polymer degradation rates. These degradable LbL drug release systems capitalize on a change in the pH to release the drug to the environment [246]. Macdonald et al. showed that a linear drug release profile can be achieved through manipulating

the hydrolytic surface degradation of the biocompatible and degradable polymers, instead of relying on diffusion, bulk release, or large pH changes [247]. This surface erosion induced linear release and enabled better control of the drug release characteristics of the system. Chen et al. reported another approach to prolong a controlled, linear drug release is to manipulate the arrangement sequence. LbL films were built with positively charged 21-arm poly[2-(dimethylamino)ethyl methacrylate] (star-PDMAEMA) and negatively charged insulin (INS) and glucose oxidase (GOD). These films were sensitive to glucose since GOD can convert glucose into gluconic acid. A subsequent decreased in the pH of the solution resulted in rearrangement in the morphology of the star polymer layer, resulting in the *in vitro* release of insulin [241]. Thus, the drug release behavior in degradable PEM films is mainly dependent on the erosion or degradation of the multilayer nanostructures.

The incorporation of LbL drug delivery systems into therapeutic approaches for biomedical applications has grown in recent years [223, 240, 248-250]. An area that could benefit from the development of LbL drug delivery systems is neural medicine. *In situ* delivery of functional molecules from biodegradable LbL surface coatings on transplantable scaffolds are being explored [251]. LbL drug delivery systems could be capitalized upon to provide local controlled delivery of neuroprotective or neuroregenerative drugs for conditions including SCI repair [88, 216, 251]. To overcome the drawbacks of directly injecting soluble neurotrophins, growth factors such as BDNF could be incorporated into PEM coating on transplantable scaffolds for SCI repair. As discussed in section 1.2, NTFs play a vital role in enhancing neural cell survival and axon outgrowth during development as well as after trauma. They promote survival and provide neuroprotection to motor and sensory neurons, as well as enhance axonal regeneration [31]. The delivery of NTFs several weeks post-injury leads to improvement in neuronal survival

and axonal regeneration in the spinal cord [252]. However, the half-life of NTFs through a single injection is only a few hours, thus approaches to facilitate sustained local delivery is key [253]. In addition to the release time, the dosage, the location of NTF delivery, and release kinetics must also be tightly controlled. Therefore, a controlled, sustained release of NTFs should be an integral component of any strategy that aims to achieve functional regeneration of axons after SCI. LbL drug delivery systems have demonstrated their unique advantage in providing a longer release profile as compared to other drug delivery methods [254]. Gradual degradation of a hydrogen-bonded PAA/PEG/lysozyme film on agarose scaffold was found to successfully release active protein over a period of one month. Since the protein size and isoelectric point of lysozyme is similar to BDNF, this LbL drug release system hold promise for sustaining release of active BDNF from three-dimensional agarose scaffolds [251]. The cumulative lysozyme release profile is shown in Figure 6.4.

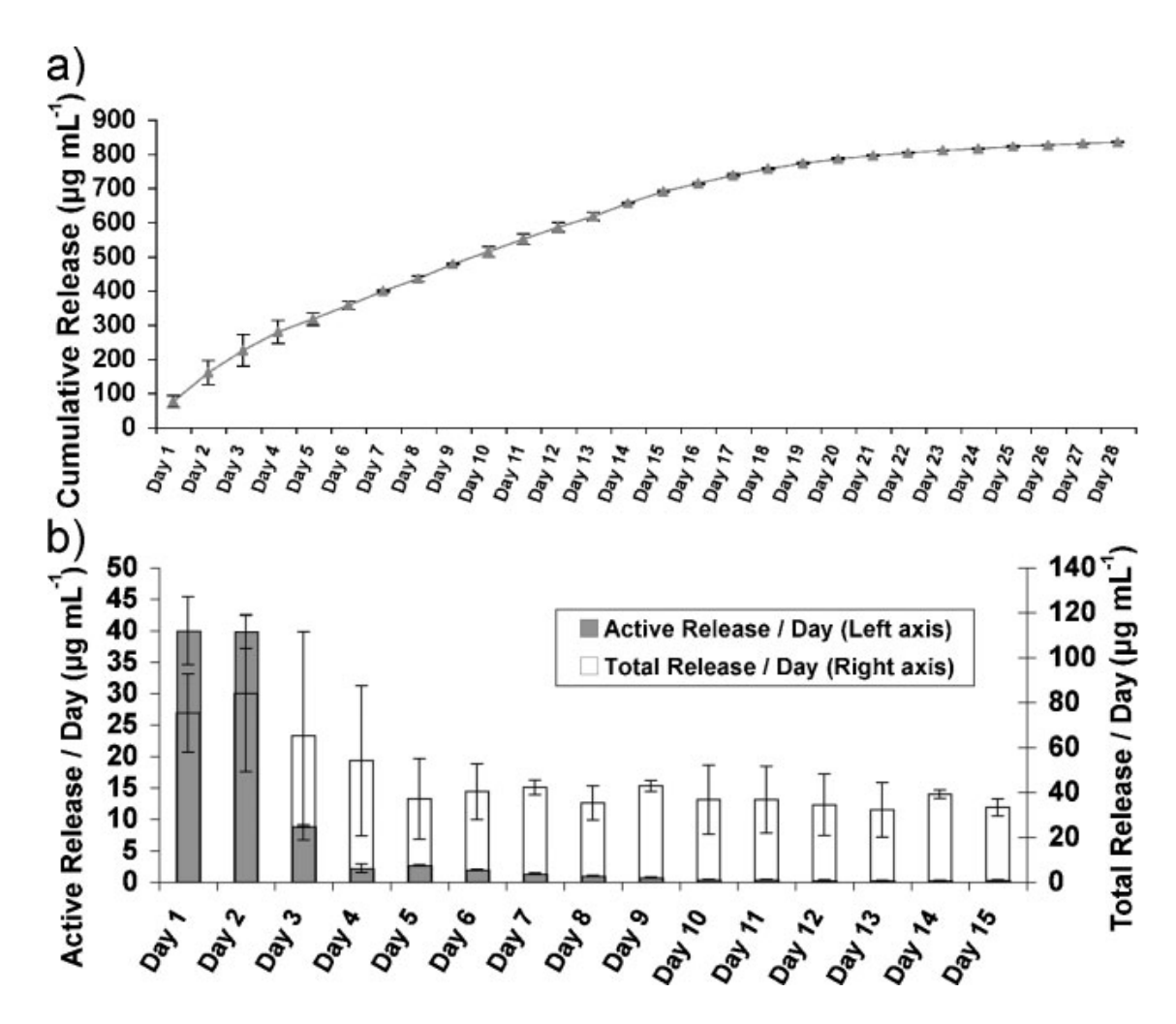


Figure 6.4. Lysozyme release profile from LbL for 4 weeks.

(a) Physiological pHtriggered cumulative release of lysozyme from LbL-coated 3% agarose hydrogel. (b) Total and enzymatically active lysozyme released per day [119]. (Reproduced with permission from Ref. [119]. Copyright Wiley- VCH Verlag GmbH & Co. KGaA.)

In addition, the LbL approach enables the loading of multiple growth factors within the multilayer structure [240]. This is significant since different NTFs are required in the nervous systems, for example, the subset of rat dorsal root ganglions that mediate pain (nociceptors) contain different subpopulations of neurons, with 65% depending on GDNF, 35% depending on NGF alone, and 9% depending on both factors [255]. Thus, to regenerate the nervous system

after trauma or injury would require multiple NTFs. LbL techniques would be amenable and could easily incorporate and deliver multiple growth factors for neural regeneration after SCI. Much work is needed to study delivery systems that can deliver multiple growth factors for SCI repair.

Effective therapies for SCI do not exist. Therapies for SCI must be able to regrow axons that traverse the lesion site, myelinate the axons, protect from neuronal death, suppress inflammation and prevent the formation of a reactive cell layer, and up-regulate the beneficial effects of glial cells (i.e. growth factor secretion and neuronal protection). Successful therapies may require scaffolds that can address each of these issues. We propose that the LbL approach could help to achieve most if not all of these goals through their: 1) flexibility in coating any surface topography, 2) tunable thickness and architecture, and 3) ability to incorporate multiple biofunctional molecules (i.e. drugs, growth factors, ECM proteins, nucleic acids, etc.) required for proper nerve regeneration. These LbL films could perform simultaneous roles as structural elements, drug carriers, and cell binding sites. Biodegradable PEM coated transplantable scaffolds that are capable of *in vivo* drug release of anti-inflammation drugs or growth factors could be useful in long-term nerve regeneration and myelination after SCI. These scaffolds could be situated close to the lesion site, ensuring not only physical guidance for axon alignment, but also long-term sustained release of growth factors.

In summary, due to their technological ease, flexibility in structure and components, and the ability for controlled release, LbL self-assembled films could be integrated into transplantable scaffolds to provide a robust and versatile platform to create novel scaffolds that promote cell adhesion and deliver drugs to repair spinal cord injury.

APPENDIX

Appendix SC migration velocity quantification

A.1 Grid pattern for data acquisition.

For each set of experiment, the images were taken daily of each sample in a grid pattern for the entire 1 cm * 1 cm patterned surface. The grid is composed of successive rectangular images (1600 * 1200 pixel) which are numbered sequentially (column and row) from one end to the other end of the microgrooves and from top to bottom. The number of cells in each image were counted and entered into each grid. Table A.1 - A. 6 show the grid records of SC migration from day 8 to day 15 on 50 µm, 100 µm, and 150 µm microgrooved surfaces.

Table A.1. Grid record of SC migration on day 8 for $50\,\mu m$ (a), $100\,\mu m$ (b), and $150\,\mu m$ (c) microgrooved surfaces.

(a)

9	8	7	6	5	4	3	2	1	
									1
						3	23	21	2
				2	7	2	0	26	3
								18	4
	1	0	1	2	0	1	0	15	5
					2	1	1	13	6
	1	3	3	0	0	7	8	28	7
					4	1	6	46	8
					1	3	0	26	9
		2	1	9	0	1	1	3	10
			6	5	3	6	6	5	11

(Table A.1 cont'd)

(b)

9	8	7	6	5	4	3	2	1	
	1	10	4	1	1	2	0	2	1
		2	0	4	1	1	1	0	2
						2	2	2	3
				2	0	0	0	0	4
			1	1	1	0	2	1	5
		2	3	13	4	2	2	7	6
					2	0	3	4	7
	1	1	1	2	1	1	1	12	8
1	0	0	2	1	0	0	3	19	9
	2	0	6	2	1	0	4	27	10
	1	2	2	0	5	0	0	1	11

(c)

9	8	7	6	5	4	3	2	1	
									1
							1	15	2
							1	24	3
			1	0	0	2	1	24	4
						2	3	9	5
							7	24	6
		2	3	0	1	0	2	15	7
		2	2	6	0	0	1	5	8
							1	2	9
					2	2	0	3	10
			2	0	0	0	0	3	11

Table A.2. Grid record of SC migration on day 9 for 50 μm (a), 100 μm (b), and 150 μm (c) microgrooved surfaces.

(a)

9	8	7	6	5	4	3	2	1	
1	1	0	2	9	15	1	1	0	1
	1	2	6	1	0	5	27	32	2
		2	0	2	10	4	5	45	3
			3	0	0	0	5	21	4
2	1	0	2	0	0	4	5	22	5
						1	3	24	6
	1	10	2	0	0	11	19	41	7
1	0	2	8	1	6	4	12	62	8
		1	0	4	3	5	4	51	9
		2	1	6	0	1	2	19	10
1	0	4	8	9	5	8	6	10	11

(b)

9	8	7	6	5	4	3	2	1	
2	1	4	3	0	0	1	0	0	1
	4	6	1	3	1	0	1	0	2
	3	0	2	2	1	7	3	0	3
		7	0	3	0	0	0	0	4
	1	8	2	2	0	0	1	2	5
		3	5	15	7	2	2	10	6
							5	0	7
	2	0	0	2	3	7	0	18	8
	1	6	1	3	0	2	5	28	9
	1	0	3	3	0	0	1	37	10
	1	2	0	0	6	2	0	6	11

(Table A.2 cont'd)

(c)

9	8	7	6	5	4	3	2	1	
		1	0	0	2	2	1	14	1
			2	0	0	1	3	46	2
							4	31	3
		1	1	1	3	3	4	34	4
				2	1	1	1	24	5
		2	0	0	0	0	11	44	6
	2	1	4	6	3	1	5	28	7
							1	9	8
			1	0	0	0	1	8	9
		4	1	1	6	0	2	2	10
			1	0	0	0	0	5	11

Table A.3. Grid record of SC migration on day 10 for $50\,\mu m$ (a), $100\,\mu m$ (b), and $150\,\mu m$ (c) microgrooved surfaces.

(a)

9	8	7	6	5	4	3	2	1	
	1	2	4	8	15	4	0	2	1
		2	3	0	0	9	28	24	2
		2	0	4	8	5	5	25	3
			3	0	0	1	8	9	4
			1	1	0	4	11	14	5
			1	0	0	2	8	14	6
	1	7	5	1	1	4	15	36	7
	2	1	2	2	1	5	15	35	8
				4	1	6	9	48	9
		2	1	2	2	1	0	27	10
		4	9	9	1	7	3	9	11

(Table A.3 cont'd)

(b)

9	8	7	6	5	4	3	2	1	
		4	6	1	0	0	1	0	1
		3	0	1	0	3	2	0	2
	2	2	1	2	1	2	0	1	3
		6	0	0	4	0	1	2	4
	1	4	3	1	0	0	0	2	5
	1	3	3	3	4	1	9	7	6
	2	0	1	5	11	3	1	0	7
1	1	0	1	0	1	4	2	19	8
		2	3	5	2	2	8	20	9
1	0	0	1	2	0	0	1	12	10
	1	0	0	3	6	2	0	9	11

(c)

9	8	7	6	5	4	3	2	1	
					2	2	3	11	1
			1	0	2	7	6	35	2
						2	12	40	3
	1	2	0	1	5	6	22	64	4
				2	0	0	7	20	5
							12	33	6
	1	1	4	4	1	1	13	37	7
			1	0	0	0	3	14	8
		1	0	0	0	0	1	5	9
								2	10
			2	0	0	0	1	4	11

Table A.4. Grid record of SC migration on day 13 for $50\,\mu m$ (a), $100\,\mu m$ (b), and $150\,\mu m$ (c) microgrooved surfaces.

(a)

9	8	7	6	5	4	3	2	1	
2	7	8	15	25	35	21	11	16	1
2	3	9	10	5	13	24	44	56	2
		14	13	20	17	25	46	67	3
3	15	13	9	1	1	6	25	61	4
			2	4	5	15	31	44	5
1	0	0	3	1	7	15	33	49	6
	10	30	18	4	8	17	29	70	7
5	12	12	29	18	9	31	64	137	8
1	3	5	11	6	10	21	64	106	9
	1	1	9	2	0	11	59	100	10
	3	17	28	27	34	18	22	49	11

(b)

9	8	7	6	5	4	3	2	1	
	4	4	0	1	0	0	0	0	1
	2	15	6	0	2	2	3	4	2
	7	14	18	2	5	16	14	7	3
3	28	44	22	1	0	2	7	40	4
9	47	22	4	4	0	0	4	11	5
2	4	6	21	7	10	4	14	22	6
		3	7	31	20	12	21	23	7
8	20	8	5	25	60	63	35	44	8
	1	12	14	12	11	9	22	52	9
	1	0	7	12	21	4	13	51	10
		4	5	5	14	17	11	29	11

(Table A.4 cont'd)

(c)

9	8	7	6	5	4	3	2	1	
		5	9	6	24	55	36	27	1
	2	1	3	8	26	31	44	96	2
				2	6	30	93	119	3
	1	0	3	14	23	80	90	112	4
	3	3	1	1	1	15	70	104	5
			1	1	1	51	120	209	6
	5	5	5	3	6	40	97	151	7
2	5	3	5	3	3	5	54	104	8
			1	0	0	0	18	75	9
						2	9	27	10
			1	5	2	1	13	20	11

Table A.5. Grid record of SC migration on day 14 for $50\,\mu m$ (a), $100\,\mu m$ (b), and $150\,\mu m$ (c) microgrooved surfaces.

(a)

9	8	7	6	5	4	3	2	1	
16	24	5	18	37	41	55	15	39	1
6	6	8	1	0	10	32	71	79	2
	5	9	20	21	32	35	55	82	3
12	30	15	15	1	1	13	40	85	4
			1	3	0	18	29	70	5
2	0	3	3	2	5	12	40	82	6
4	15	33	38	17	13	16	44	117	7
8	21	22	26	18	11	48	92	149	8
2	3	6	3	7	10	22	94	121	9
			8	7	4	20	57	81	10
	2	4	10	18	27	16	33	68	11

(Table A.5 cont'd)

(b)

9	8	7	6	5	4	3	2	1	
	2	4	0	0	0	0	0	2	1
	5	14	5	1	2	1	3	1	2
	5	22	18	1	6	14	11	9	3
5	35	63	20	10	1	3	12	29	4
17	38	30	12	6	0	0	5	14	5
	5	6	23	9	13	12	25	17	6
1	0	4	11	44	30	26	19	26	7
	24	4	8	22	68	52	26	33	8
	2	13	13	8	9	19	24	48	9
			4	8	8	5	18	47	10
		2	4	13	7	17	7	35	11

(c)

9	8	7	6	5	4	3	2	1	
		13	33	6	4	5	36	60	1
1	5	4	0	2	27	43	55	123	2
			1	0	7	50	109	142	3
	2	0	1	7	33	71	97	131	4
	2	1	0	2	0	48	97	142	5
					13	60	129	267	6
	6	9	7	4	10	39	91	187	7
1	1	1	2	3	1	10	59	156	8
			1	0	0	2	21	66	9
				1	0	14	14	43	10
					1	0	2	1	11

Table A.6. Grid record of SC migration on day 15 for $50\,\mu m$ (a), $100\,\mu m$ (b), and $150\,\mu m$ (c) microgrooved surfaces.

(a)

9	8	7	6	5	4	3	2	1	
47	50	18	27	95	63	83	36	79	1
17	22	15	17	37	31	50	99	122	2
3	13	28	47	44	40	59	81	129	3
14	70	37	23	6	10	19	60	121	4
		1	1	6	8	36	53	131	5
	2	8	5	6	24	33	66	117	6
7	41	48	47	33	20	19	66	128	7
13	37	46	41	54	42	77	135	230	8
2	5	14	20	26	33	62	107	171	9
1	3	2	12	10	14	53	102	190	10
	3	15	25	31	56	35	82	143	11

(b)

9	8	7	6	5	4	3	2	1	
	8	24	1	2	4	3	0	7	1
	10	27	13	3	7	16	15	11	2
2	9	36	20	11	10	17	30	31	3
23	39	42	29	10	8	7	34	51	4
38	84	52	17	7	2	2	19	37	5
4	11	13	33	22	27	35	49	20	6
8	11	6	46	102	59	67	39	32	7
15	55	17	19	24	58	58	74	62	8
1	16	34	43	24	16	35	49	88	9
5	3	2	11	11	11	21	35	83	10
5	1	4	8	41	24	31	16	35	11

(Table A.6 cont'd)

(c)

9	8	7	6	5	4	3	2	1	
		1	1	1	4	3	12	55	1
				3	12	52	53	108	2
	1	0	1	0	7	91	94	169	3
			2	0	2	49	102	149	4
		3	2	6	10	67	127	163	5
					9	77	112	201	6
1	0	3	2	1	14	49	93	215	7
		1	4	2	1	5	34	90	8
					4	2	15	37	9
				1	1	12	9	29	10
					1	4	2	1	11

A.2 Definition of leading edge.

The leading edge is defined as the furthest location that the cells traversed in each row and is highlighted in yellow. An equivalent distance (e) of image x-y was calculated by multiplying the column number (x) by the actual length of the image (l).

9	8	7	6	5	4	3	2	1	
	4	4	0	1	0	0	0	0	1
	2	15	6	0	2	2	3	4	2
	7	14	18	2	5	16	14	7	3
3	28	44	22	1	0	2	7	40	4
9	47	22	4	4	0	0	4	11	5
2	4	6	21	7	10	4	14	22	6
		3	7	31	20	12	21	23	7
8	20	8	5	25	60	63	35	44	8
	1	12	14	12	11	9	22	52	9
	1	0	7	12	21	4	13	51	10
		4	5	5	14	17	11	29	11

Figure A.1. Definition of leading edge.

(Figure A.1 cont'd) The leading edge is highlighted in yellow illustrated by the grid record of day 13, 100 µm microgrooved surface.

A.3 Binary method.

The binary method counts images as yes (1) or no (0), and converts the entire grid to a binary field where only the images marked as "1", highlighted in yellow, are selected for subsequent calculations.

9	8	7	6	5	4	3	2	1	
0	1	0	0	0	0	0	0	0	1
0	1	0	0	0	0	0	0	0	2
0	1	0	0	0	0	0	0	0	3
1	0	0	0	0	0	0	0	0	4
1	0	0	0	0	0	0	0	0	5
1	0	0	0	0	0	0	0	0	6
0	0	1	0	0	0	0	0	0	7
1	0	0	0	0	0	0	0	0	8
0	1	0	0	0	0	0	0	0	9
0	1	0	0	0	0	0	0	0	10
0	0	1	0	0	0	0	0	0	11

Figure A.2. Binary processing method.

The images counted as "1" are highlighted in yellow after binary processing. The figure is illustrated by the grid record of day 13, 100 µm microgrooved surface.

A. 4 Calculation of migration velocities

The average distance the cells traverse based on the column number is plotted over time, the y-axis indicates the column number in the images (Figure A.4). The slope is then converted into micron per day by multiplying the actual distance in the image (1212.12 µm) to obtain the migration velocity (Figure A.5).

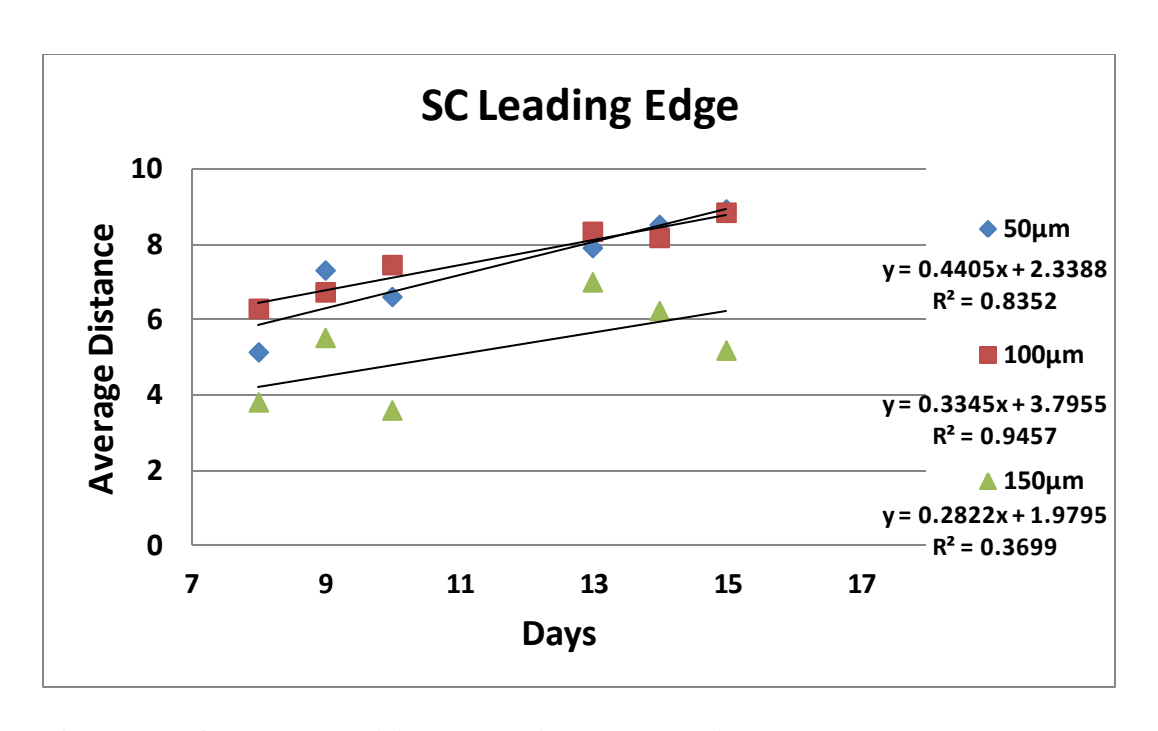


Figure A.3. Plot of average position at leading edge vs. time.

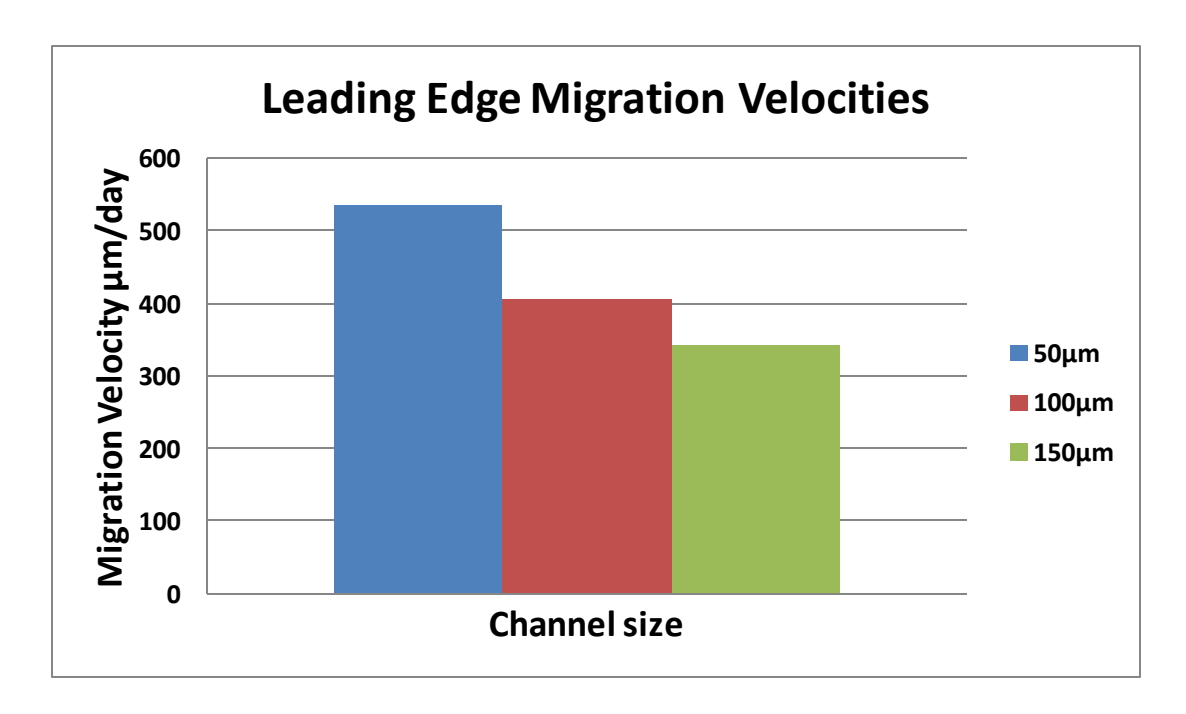


Figure A.4. Plot of migration velocity with channel size.

BIBLIOGRAPHY

BIBLIOGRAPHY

- 1. Bauchet L, Lonjon N, Perrin FE, Gilbert C, Privat A, Fattal C: **Strategies for spinal cord repair after injury: a review of the literature and information**. *Ann Phys Rehabil Med* 2009, **52**(4):330-351.
- 2. Bareyre FM: Neuronal repair and replacement in spinal cord injury. *J Neurol Sci* 2008, **265**(1-2):63-72.
- 3. Tohda C, Kuboyama T: Current and future therapeutic strategies for functional repair of spinal cord injury (vol 132, pg 57, 2011). Pharmacol Therapeut 2012, 134(1):125-125.
- 4. Gao M, Lu P, Bednark B, Lynam D, Conner JM, Sakamoto J, Tuszynski MH: Templated agarose scaffolds for the support of motor axon regeneration into sites of complete spinal cord transection. *Biomaterials* 2013, 34(5):1529-1536.
- 5. Fortun J, Hill CE, Bunge MB: Combinatorial strategies with Schwann cell transplantation to improve repair of the injured spinal cord. Neurosci Lett 2009, 456(3):124-132.
- 6. Gorio A, Torrente Y, Madaschi L, Bresolin N, Di Giulio AM: **Transplantation of autologous dermal stem cells into the spinal cord after traumatic injury.** Cell **migration and differentiation.** *J Neurotraum* 2003, **20**(10):1120-1120.
- 7. Jan E, Kotov NA: Successful Differentiation of Mouse Neural Stem Cells on Layer-by-Layer Assembled Single-Walled Carbon Nanotube Composite. Nano Letters 2007, 7(5):1123-1128.
- 8. Zhou K, Sun G, Bernard C, Thouas G, Nisbet D, Forsythe J: **Optimizing interfacial features to regulate neural progenitor cells using polyelectrolyte multilayers and brain derived neurotrophic factor**. *Biointerphases* 2011, **6**(4):189-199.
- 9. Stocum DL: **Chapter 4 Regeneration of Neural Tissues**. In *Regenerative Biology and Medicine (Second Edition)*. San Diego: Academic Press; 2012:67-97.
- 10. Sorensen A, Alekseeva T, Katechia K, Robertson M, Riehle MO, Barnett SC: Long-term neurite orientation on astrocyte monolayers. aligned by microtopography. *Biomaterials* 2007, **28**(36):5498-5508.
- 11. Coman L, Barbin G, Charles P, Zalc B, Lubetzki C: **Axonal signals in central nervous system myelination, demyelination and remyelination**. *J Neurol Sci* 2005, **233**(1-2):67-71.
- 12. Totoiu MO, Keirstead HS: **Spinal cord injury is accompanied by chronic progressive demyelination**. *Journal of Comparative Neurology* 2005, **486**(4):373-383.

- 13. Lee JK, Zheng B: Role of myelin-associated inhibitors in axonal repair after spinal cord injury. Exp Neurol 2012, 235(1):33-42.
- 14. Evercooren ABV, Avellana Adalid V, Lachapelle F, Liblau R: Schwann cell transplantation and myelin repair of the CNS. Mult Scler 1997, 3(2):157-161.
- 15. Duncan ID, Hoffman RL: Schwann cell invasion of the central nervous system of the myelin mutants. *J Anat* 1997, **190**:35-49.
- 16. Someya Y, Koda M, Dezawa M, Kamada T, Nishio Y, Okawa A, Yoshinaga K, Moriya H, Yamazaki M: **Transplantation of bone marrow stromal cell-derived Schwann cells promotes axonal regeneration and functional recovery after contusion injury of adult rat spinal cord.** *J Neurotraum* 2006, **23**(5):785-786.
- 17. Wiliams RR, Bunge MB: Schwann cell transplantation: a repair strategy for spinal cord injury? *Prog Brain Res* 2012, **201**:295-312.
- 18. Neukirchen D, Bradke F: **Neuronal polarization and the cytoskeleton**. *Semin Cell Dev Biol* 2011, **22**(8):825-833.
- 19. Roach P, Parker T, Gadegaard N, Alexander MR: **Surface strategies for control of neuronal cell adhesion: A review**. *Surf Sci Rep* 2010, **65**(6):145-173.
- 20. Gros T, Sakamoto JS, Blesch A, Havton LA, Tuszynski MH: **Regeneration of long-tract** axons through sites of spinal cord injury using templated agarose scaffolds. *Biomaterials* 2010, **31**(26):6719-6729.
- 21. Cao H, Liu T, Chew SY: **The application of nanofibrous scaffolds in neural tissue engineering**. *Advanced Drug Delivery Reviews* 2009, **61**(12):1055-1064.
- 22. Santos E, Hernández RM, Pedraz JL, Orive G: Novel advances in the design of three-dimensional bio-scaffolds to control cell fate: translation from 2D to 3D. Trends in Biotechnology 2012, 30(6):331-341.
- 23. Previtera ML, Hui M, Verma D, Shahin AJ, Schloss R, Langrana NA: **The effects of substrate elastic modulus on neural precursor cell behavior**. *Ann Biomed Eng* 2013, **41**(6):1193-1207.
- 24. Vozzi G, Flaim CJ, Bianchi F, Ahluwalia A, Bhatia S: Microfabricated PLGA scaffolds: a comparative study for application to tissue engineering. *Materials Science and Engineering:* C 2002, **20**(1–2):43-47.
- 25. Gentile FT, Doherty EJ, Rein DH, Shoichet MS, Winn SR: Polymer Science for Macroencapsulation of Cells for Central-Nervous-System Transplantation. *React Polym* 1995, **25**(2-3):207-227.

- 26. Malafaya PB, Silva GA, Reis RL: **Natural-origin polymers as carriers and scaffolds for biomolecules and cell delivery in tissue engineering applications**. *Advanced Drug Delivery Reviews* 2007, **59**(4–5):207-233.
- 27. Norman LL, Aranda-Espinoza H: Cortical Neuron Outgrowth is Insensitive to Substrate Stiffness. Cellular and Molecular Bioengineering 2010, 3(4):398-414.
- 28. Rajnicek AM, Britland S, McCaig CD: Contact guidance of CNS neurites on grooved quartz: influence of groove dimensions, neuronal age and cell type. *J Cell Sci* 1997, 110:2905-2913.
- 29. Fricke R, Zentis PD, Rajappa LT, Hofmann B, Banzet M, Offenhäusser A, Meffert SH: Axon guidance of rat cortical neurons by microcontact printed gradients. *Biomaterials* 2011, **32**(8):2070-2076.
- 30. Thompson DM, Buettner HM: **Oriented Schwann cell monolayers for directed neurite outgrowth**. *Ann Biomed Eng* 2004, **32**(8):1120-1130.
- 31. Thorne RG, Frey WH: **Delivery of neurotrophic factors to the central nervous system Pharmacokinetic considerations**. *Clin Pharmacokinet* 2001, **40**(12):907-946.
- 32. Fiore M, Chaldakov GN, Aloe L: Nerve Growth Factor as a Signaling Molecule for Nerve Cells and also for the Neuroendocrine-Immune Systems. Rev Neuroscience 2009, 20(2):133-145.
- 33. Binder DK, Scharfman HE: **Brain-derived neurotrophic factor**. *Growth Factors* 2004, **22**(3):123-131.
- 34. Maisonpierre PC, Belluscio L, Squinto S, Ip NY, Furth ME, Lindsay RM, Yancopoulos GD: Neurotrophin-3: a neurotrophic factor related to NGF and BDNF. Science 1990, 247(4949 Pt 1):1446-1451.
- 35. Zechel S, Werner S, Unsicker K, von Bohlen und Halbach O: **Expression and Functions of Fibroblast Growth Factor 2 (FGF-2) in Hippocampal Formation**. *Neuroscientist* 2010, **16**(4):357-373.
- 36. Barres BA, Hart IK, Coles HSR, Burne JF, Voyyodic JT, Richardson WD, Raff MC: Cell-Death and Control of Cell-Survival in the Oligodendrocyte Lineage. *Cell* 1992, **70**(1):31-46.
- 37. Deng L-X, Hu J, Liu N, Wang X, Smith GM, Wen X, Xu X-M: **GDNF modifies** reactive astrogliosis allowing robust axonal regeneration through Schwann cell-seeded guidance channels after spinal cord injury. *Experimental Neurology* 2011, 229(2):238-250.

- 38. Brown XQ, Ookawa K, Wong JY: Evaluation of polydimethylsiloxane scaffolds with physiologically-relevant elastic moduli: interplay of substrate mechanics and surface chemistry effects on vascular smooth muscle cell response. *Biomaterials* 2005, 26(16):3123-3129.
- 39. Lotters JC, Olthuis W, Veltink PH, Bergveld P: **The mechanical properties of the rubber elastic polymer polydimethylsiloxane for sensor applications**. *J Micromech Microeng* 1997, **7**(3):145-147.
- 40. Gottlieb M, Macosko CW: Stress-Strain Relations for Pdms Networks. *J Rheol* 1979, **23**(3):393-393.
- 41. VanLandingham MR, Drzal PL, White CC: **Indentation creep and relaxation measurements of polymers**. *Mater Res Soc Symp P* 2005, **841**:193-204.
- 42. Kim TK, Kim JK, Jeong OC: **Measurement of nonlinear mechanical properties of PDMS elastomer**. *Microelectron Eng* 2011, **88**(8):1982-1985.
- 43. Callister WD, Rethwisch DG: Fundamentals of Materials Science and Engineering: An Integrated Approach: Wiley; 2012.
- 44. Lopera S, Mansano RD: **Plas ma-Based Surface Modification of Polydimethylsiloxane for PDMS-PDMS Molding**. *ISRN Polymer Science* 2012, **2012**:5.
- 45. Bhattacharya S, Datta A, Berg JM, Gangopadhyay S: **Studies on surface wettability of poly(dimethyl) siloxane (PDMS) and glass under oxygen-plasma treatment and correlation with bond strength.** *J Microelectromech S* 2005, **14**(3):590-597.
- 46. Kim B, Peterson ETK, Papautsky I: **Long-term stability of plasma oxidized PDMS surfaces**. *P Ann Int Ieee Embs* 2004, **26**:5013-5016.
- 47. Matsuda T, Takahashi K, Nariai T, Ito T, Takatani T, Fujio Y, Azuma J: N-cadherin-mediated cell adhesion determines the plasticity for cell alignment in response to mechanical stretch in cultured cardiomyocytes. *Biochem Bioph Res Co* 2005, 326(1):228-232.
- 48. Wang JHC, Yang GG, Li ZZ, Shen W: **Fibroblast responses to cyclic mechanical stretching depend on cell orientation to the stretching direction**. *J Biomech* 2004, **37**(4):573-576.
- 49. Xu BY, Song GB, Ju Y, Li X, Song YH, Watanabe S: RhoA/ROCK, cytoskeletal dynamics, and focal adhesion kinase are required for mechanical stretch-induced tenogenic differentiation of human mesenchymal stem cells. *J Cell Physiol* 2012, 227(6):2722-2729.
- 50. Guo Y, Zhang XZ, Zhang CQ, Li RX, Zeng QC, Guo C, Zhang YJ: Effects of mechanical stimulus on mesenchymal stem cells differentiation toward cardiomyocytes. *Asian Biomed* 2011, **5**(5):655-661.

- 51. Huang CH, Chen MH, Young TH, Jeng JH, Chen YJ: Interactive Effects of Mechanical Stretching and Extracellular Matrix Proteins on Initiating Osteogenic Differentiation of Human Mesenchymal Stem Cells. *J Cell Biochem* 2009, 108(6):1263-1273.
- 52. Goli-Malekabadi Z, Tafazzoli-Shadpour M, Rabbani M, Janmaleki M: **Effect of uniaxial** stretch on morphology and cytoskeleton of human mesenchymal stem cells: static vs. dynamic loading. *Biomed Tech* 2011, **56**(5):259-265.
- 53. Kaunas R, Hsu HJ: A kinematic model of stretch-induced stress fiber turnover and reorientation. *J Theor Biol* 2009, **257**(2):320-330.
- 54. Wang JHC, Goldschmidt-Clermont P, Wille J, Yin FCP: **Specificity of endothelial cell reorientation in response to cyclic mechanical stretching**. *J Biomech* 2001, **34**(12):1563-1572.
- 55. Collinsworth AM, Torgan CE, Nagda SN, Rajalingam RJ, Kraus WE, Truskey GA: Orientation and length of mammalian skeletal myocytes in response to a unidirectional stretch. Cell Tissue Res 2000, 302(2):243-251.
- 56. Haston WS, Shields JM, Wilkinson PC: **The Orientation of Fibroblasts and Neutrophils on Elastic Substrata**. *Exp Cell Res* 1983, **146**(1):117-126.
- 57. Mehrotra S, Hunley SC, Pawelec KM, Zhang LX, Lee I, Baek S, Chan C: Cell Adhesive Behavior on Thin Polyelectrolyte Multilayers: Cells Attempt to Achieve Homeostasis of Its Adhesion Energy. *Langmuir* 2010, 26(15):12794-12802.
- 58. Baek S, Gleason RL, Rajagopal KR, Humphrey JD: **Theory of small on large: Potential utility in computations of fluid-solid interactions in arteries**. *Comput Method Appl M* 2007, **196**(31-32):3070-3078.
- 59. S. Zeinali-Davarani JC, S. Baek: On parameter estimations for biaxial mechanical behavior of arteries. *J Biomech* 2009, **42**:524-530.
- 60. C.A. Figueroa SB, C.A. Taylor, J.D. Humphrey: A computational framework for coupled fluid-solid growth in cardiovascular simulations. Comput Method Appl M 2009, 198:3583-3602.
- 61. Cheng CM, Steward RL, Leduc PR: **Probing cell structure by controlling the mechanical environment with cell-substrate interactions**. *J Biomech* 2009, **42**(2):187-192.
- 62. Chen CS: **Mechanotransduction a field pulling together?** *J Cell Sci* 2008, **121**(20):3285-3292.
- 63. Hoffman-Kim D, Mitchel JA, Bellamkonda RV: **Topography, Cell Response, and Nerve Regeneration**. *Annu Rev Biomed Eng* 2010, **12**:203-231.

- 64. Kai D, Prabhakaran MP, Jin GR, Ramakrishna S: **Guided orientation of cardiomyocytes on electrospun aligned nanofibers for cardiac tissue engineering**. *J Biomed Mater Res B* 2011, **98B**(2):379-386.
- 65. Davies PF, Remuzzi A, Gordon EJ, Dewey CF, Gimbrone MA: **Turbulent Fluid Shear-Stress Induces Vascular Endothelial-Cell Turnover Invitro**. *P Natl Acad Sci USA* 1986, **83**(7):2114-2117.
- 66. Salameh A, Wustmann A, Karl S, Blanke K, Apel D, Rojas-Gomez D, Franke H, Mohr FW, Janousek J, Dhein S: Cyclic Mechanical Stretch Induces Cardiomyocyte Orientation and Polarization of the Gap Junction Protein Connexin43. Circ Res 2010, 106(10):1592-1602.
- 67. Zheng WF, Jiang B, Wang D, Zhang W, Wang Z, Jiang XY: **A microfluidic flow-stretch chip for investigating blood vessel biomechanics**. *Lab Chip* 2012, **12**(18):3441-3450.
- 68. Neyt C, Welch M, Langston A, Kohtz J, Fishell G: **A short-range signal restricts cell movement between telencephalic proliferative zones**. *J Neurosci* 1997, **17**(23):9194-9203.
- 69. Altman J: Postnatal development of the cerebellar cortex in the rat. IV. Spatial organization of bipolar cells, parallel fibers and glial palisades. *J Comp Neurol* 1975, 163(4):427-447.
- 70. Song GB, Ju Y, Shen XD, Luo Q, Shi YS, Qin J: **Mechanical stretch promotes proliferation of rat bone marrow mesenchymal stem cells**. *Colloid Surface B* 2007, **58**(2):271-277.
- 71. Boccafoschi F, Bosetti M, Gatti S, Cannas M: **Dynamic Fibroblast Cultures Response to Mechanical Stretching**. *Cell Adhes Migr* 2007, **1**(3):124-128.
- 72. Leong WS, Wu SC, Pal M, Tay CY, Yu HY, Li HQ, Tan LP: Cyclic tensile loading regulates human mesenchymal stem cell differentiation into neuron-like phenotype. *J Tissue Eng Regen M* 2012, **6**:s68-s79.
- 73. Murry CE, Jennings RB, Reimer KA: **Preconditioning with Ischemia a Delay of Lethal Cell Injury in Ischemic Myocardium**. *Circulation* 1986, **74**(5):1124-1136.
- 74. Naruse K, Yamada T, Sokabe M: **Involvement of SA channels in orienting response of cultured endothelial cells to cyclic stretch**. *Am J Physiol-Heart C* 1998, **274**(5):H1532-H1538.
- 75. James CD, Davis R, Meyer M, Turner A, Turner S, Withers G, Kam L, Banker G, Craighead H, Isaacson M *et al*: **Aligned microcontact printing of micrometer-scale poly-L-lysine structures for controlled growth of cultured neurons on planar microelectrode arrays**. *Ieee T Bio-Med Eng* 2000, **47**(1):17-21.

- 76. Dowell-Mesfin NM, Abdul-Karim MA, Turner AM, Schanz S, Craighead HG, Roysam B, Turner JN, Shain W: **Topographically modified surfaces affect orientation and growth of hippocampal neurons**. *J Neural Eng* 2004, **1**(2):78-90.
- 77. Neidlinger-Wilke C, Grood E, Claes L, Brand R: **Fibroblast orientation to stretch begins within three hours**. *J Orthopaed Res* 2002, **20**(5):953-956.
- 78. Tohda C, Kuboyama T: Current and future therapeutic strategies for functional repair of spinal cord injury. *Pharmacol Therapeut* 2011, **132**(1):57-71.
- 79. Li Y, Field PM, Raisman G: Repair of adult rat corticospinal tract by transplants of olfactory ensheathing cells. *Science* 1997, **277**(5334):2000-2002.
- 80. Geller HM, Fawcett JW: **Building a bridge: Engineering spinal cord repair**. *Exp Neurol* 2002, **174**(2):125-136.
- 81. Berns EJ, Sur S, Pan LL, Goldberger JE, Suresh S, Zhang SM, Kessler JA, Stupp SI: Aligned neurite outgrowth and directed cell migration in self-assembled monodomain gels. *Biomaterials* 2014, 35(1):185-195.
- 82. Chua JS, Chng CP, Moe AAK, Tann JY, Goh ELK, Chiam KH, Yim EKF: Extending neurites sense the depth of the underlying topography during neuronal differentiation and contact guidance. *Biomaterials* 2014, **35**(27):7750-7761.
- 83. Loverde JR, Pfister BJ: Parallels between Axon Stretch Growth and Regeneration Following Injury. *J Neurotraum* 2012, **29**(10):A28-A29.
- 84. Suter DM, Miller KE: **The emerging role of forces in axonal elongation**. *Prog Neurobiol* 2011, **94**(2):91-101.
- 85. Kidambi S, Lee I, Chan C: Primary Neuron/Astrocyte Co-Culture on Polyelectrolyte Multilayer Films: A Template for Studying Astrocyte-Mediated Oxidative Stress in Neurons. Advanced Functional Materials 2008, 18(2):294-301.
- 86. Xia H, Chen Q, Fang Y, Liu D, Zhong D, Wu H, Xia Y, Yan Y, Tang W, Sun X: Directed neurite growth of rat dorsal root ganglion neurons and increased colocalization with Schwann cells on aligned poly(methyl methacrylate) electrospun nanofibers. Brain Research 2014, 1565(0):18-27.
- 87. Mitchel JA, Hoffman-Kim D: Cellular Scale Anisotropic Topography Guides Schwann Cell Motility. Plos One 2011, 6(9).
- 88. Mehrotra S, Lynam D, Liu C, Shahriari D, Lee I, Tuszynski M, Sakamoto J, Chan C: **Time Controlled Release of Arabinofuranosylcytosine (Ara-C) from Agarose Hydrogels using Layer-by-Layer Assembly: An In Vitro Study**. *J Biomat Sci-Polym E* 2012, **23**(1-4):439-463.

- 89. Smith DH: Stretch growth of integrated axon tracts: Extremes and exploitations. *Prog Neurobiol* 2009, **89**(3):231-239.
- 90. Lau K, Tao H, Liu HJ, Wen J, Sturgeon K, Sorfazlian N, Lazic S, Burrows JTA, Wong MD, Li DY *et al*: **Anisotropic stress orients remodelling of mammalian limb bud ectoderm**. *Nat Cell Biol* 2015, **17**(5):569-U595.
- 91. Liu C, Baek S, Kim J, Vasko E, Pyne R, Chan C: Effect of Static Pre-stretch Induced Surface Anisotropy on Orientation of Mesenchymal Stem Cells. Cell Mol Bioeng 2014, 7(1):106-121.
- 92. Miller ED, Li K, Kanade T, Weiss LE, Walker LM, Campbell PG: **Spatially directed guidance of stem cell population migration by immobilized patterns of growth factors**. *Biomaterials* 2011, **32**(11):2775-2785.
- 93. Ahmed Z, Brown RA: Adhesion, alignment, and migration of cultured Schwann cells on ultrathin fibronectin fibres. *Cell Motil Cytoskel* 1999, **42**(4):331-343.
- 94. Hsu SH, Chen CY, Lu PS, Lai CS, Chen CJ: **Oriented Schwann cell growth on microgrooved surfaces**. *Biotechnology and Bioengineering* 2005, **92**(5):579-588.
- 95. Miller C, Jeftinija S, Mallapragada S: Micropatterned Schwann cell-seeded biodegradable polymer substrates significantly enhance neurite alignment and outgrowth. *Tissue Eng* 2001, 7(6):705-715.
- 96. Wang HB, Mullins ME, Cregg JM, McCarthy CW, Gilbert RJ: Varying the diameter of aligned electrospun fibers alters neurite outgrowth and Schwann cell migration. *Acta Biomaterialia* 2010, **6**(8):2970-2978.
- 97. Bauchet L, Mille-Hamard L, Baillet-Derbin C, Horvat JC: **Transplantation of autologous dorsal root ganglia into the peroneal nerve of adult rats: Uni- and bidirectional axonal regrowth from the grafted DRG neurons**. *Experimental Neurology* 2001, **167**(2):312-320.
- 98. Kuhlengel KR, Bunge MB, Bunge RP: Implantation of Cultured Sensory Neurons and Schwann-Cells into Lesioned Neonatal Rat Spinal-Cord .1. Methods for Preparing Implants from Dissociated Cells. *Journal of Comparative Neurology* 1990, 293(1):63-73.
- 99. Rosario CM, Aldskogius H, Carlstedt T, Sidman RL: **Differentiation and Axonal Outgrowth Pattern of Fetal Dorsal-Root Ganglion-Cells Orthotopically Allografted into Adult-Rats**. *Experimental Neurology* 1993, **120**(1):16-31.
- 100. Marwah J, Teitelbaum H, Prasad KN: *Neural Transplantation, CNS Neuronal Injury, and Regeneration*: Taylor & Francis; 1994.

- 101. Pfister BJ, Iwata A, Taylor AG, Wolf JA, Meaney DF, Smith DH: **Development of transplantable nervous tissue constructs comprised of stretch-grown axons**. *Journal of Neuroscience Methods* 2006, **153**(1):95-103.
- 102. Khuong HT, Midha R: Advances in Nerve Repair. Curr Neurol Neurosci 2013, 13(1).
- 103. Bi XP, Li W: Fabrication of Flexible Microlens Array through Vapor-induced Room Temperature Dewetting on Plasma Treated Parylene-C. *Ieee Eng Med Bio* 2014:2085-2088.
- 104. Liu C, Baek S, Kim J, Vasko E, Pyne R, Chan C: Effect of Static Pre-stretch Induced Surface Anisotropy on Orientation of Mesenchymal Stem Cells. Cel Mol Bioeng 2013:1-16.
- 105. Mantuano E, Jo M, Gonias SL, Campana WM: Low Density Lipoprotein Receptor-related Protein (LRP1) Regulates Rac1 and RhoA Reciprocally to Control Schwann Cell Adhesion and Migration. *Journal of Biological Chemistry* 2010, **285**(19):14259-14266.
- 106. Koch D, Rosoff WJ, Jiang JJ, Geller HM, Urbach JS: Strength in the Periphery: Growth Cone Biomechanics and Substrate Rigidity Response in Peripheral and Central Nervous System Neurons. *Biophys J* 2012, **102**(3):452-460.
- 107. Franze K, Guck J: **The biophysics of neuronal growth**. *Rep Prog Phys* 2010, **73**(9).
- 108. Heidemann SR, Lamoureux P, Buxbaum RE: **Growth Cone Behavior and Production of Traction Force**. *J Cell Biol* 1990, **111**(5):1949-1957.
- 109. Brushart TM, Mathur V, Sood R, Koschorke GM: **Dispersion of Regenerating Axons across Enclosed Neural Gaps**. *J Hand Surg-Am* 1995, **20A**(4):557-564.
- 110. Waxman SG, McDonald WI: Form and Function in the Brain and Spinal Cord: Perspectives of a Neurologist: MIT Press; 2003.
- 111. Suh YS, Chung K, Coggeshall RE: A Study of Axonal Diameters and Areas in Lumbosacral Roots and Nerves in the Rat. Journal of Comparative Neurology 1984, 222(4):473-481.
- 112. Gao MY, Lu P, Bednark B, Lynam D, Conner JM, Sakamoto J, Tuszynski MH: Templated agarose scaffolds for the support of motor axon regeneration into sites of complete spinal cord transection. *Biomaterials* 2013, 34(5):1529-1536.
- 113. Schmalenberg KE, Uhrich KE: Micropatterned polymer substrates control alignment of proliferating Schwann cells to direct neuronal regeneration. *Biomaterials* 2005, **26**(12):1423-1430.

- 114. Wen X, Tresco PA: Effect of filament diameter and extracellular matrix molecule precoating on neurite outgrowth and Schwann cell behavior on multifilament entubulation bridging device in vitro. J Biomed Mater Res A 2006, 76A(3):626-637.
- 115. Karafyllidis IG, Lagoudas DC: **Microtubules as mechanical force sensors**. *Biosystems* 2007, **88**(1-2):137-146.
- 116. Ellisman MH: **Beyond Neurofilaments and Microtubules**. *Neurosci Res Prog B* 1981, **19**(1):43-58.
- 117. Hursh JB: Conduction velocity and diameter of nerve fibers. Am J Physiol 1939, 127(1):131-139.
- Ouyang H, Nauman E, Shi RY: Contribution of cytoskeletal elements to the axonal mechanical properties. *J Biol Eng* 2013, **7**(1).
- 119. Mitchison T, Kirschner M: Cytoskeletal Dynamics and Nerve Growth. Neuron 1988, 1(9):761-772.
- 120. Peter SJ, Mofrad MRK: Computational Modeling of Axonal Microtubule Bundles under Tension. *Biophys J* 2012, **102**(4):749-757.
- 121. Kidd GJ, Ohno N, Trapp BD: **Biology of Schwann cells**. *Hand Clinic* 2013, **115**:55-79.
- 122. Beighley R, Spedden E, Sekeroglu K, Atherton T, Demirel MC, Staii C: **Neuronal alignment on asymmetric textured surfaces**. *Appl Phys Lett* 2012, **101**(14).
- 123. Park J, Koito H, Li JR, Han A: Microfluidic compartmentalized co-culture platform for CNS axon myelination research. *Biomed Microdevices* 2009, **11**(6):1145-1153.
- 124. Solanki A, Chueng STD, Yin PT, Kappera R, Chhowalla M, Lee KB: **Axonal Alignment and Enhanced Neuronal Differentiation of Neural Stem Cells on Graphene-Nanoparticle Hybrid Structures**. *Adv Mater* 2013, **25**(38):5477-5482.
- 125. Paivalainen S, Nissinen M, Honkanen H, Lahti O, Kangas SM, Peltonen J, Peltonen S, Heape AM: Myelination in mouse dorsal root ganglion/Schwann cell cocultures. *Mol Cell Neurosci* 2008, **37**(3):568-578.
- 126. Lee S, Leach MK, Redmond SA, Chong SYC, Mellon SH, Tuck SJ, Feng ZQ, Corey JM, Chan JR: A culture system to study oligodendrocyte myelination processes using engineered nanofibers. *Nat Methods* 2012, **9**(9):917-+.
- 127. Faweett JW, Keynes RJ: **Peripheral Nerve Regeneration**. *Annu Rev Neurosci* 1990, **13**(1):43-60.
- 128. Liu C, Pyne R, Baek S, Sakamoto J, Tuszynski MH, Chan C: **Axonal Regeneration and Myelination: Applicabilityof the Layer-by-Layer Technology**. In *Layer-by-Layer*

- Films for Biomedical Applications. Wiley-VCH Verlag GmbH & Co. KGaA; 2015:525-546.
- 129. Bunge RP: The Role of the Schwann-Cell in Trophic Support and Regeneration. *J Neurol* 1994, **242**(1):S19-S21.
- 130. Madigan NN, McMahon S, O'Brien T, Yaszemski MJ, Windebank AJ: Current tissue engineering and novel therapeutic approaches to axonal regeneration following spinal cord injury using polymer scaffolds. Respiratory Physiology & Neurobiology 2009, 169(2):183-199.
- 131. Spivey EC, Khaing ZZ, Shear JB, Schmidt CE: **The fundamental role of subcellular topography in peripheral nerve repair therapies**. *Biomaterials* 2012, **33**(17):4264-4276.
- 132. Gnavi S, Fomasari BE, Tonda-Turo C, Ciardelli G, Zanetti M, Geuna S, Perroteau I: **The influence of electrospun fibre size on Schwann cell behaviour and axonal outgrowth**. *Mat Sci Eng C-Mater* 2015, **48**:620-631.
- 133. Gupta D, Venugopal J, Prabhakaran MP, Dev VRG, Low S, Choon AT, Ramakrishna S: Aligned and random nanofibrous substrate for the in vitro culture of Schwann cells for neural tissue engineering. *Acta Biomaterialia* 2009, 5(7):2560-2569.
- 134. Guenard V, Kleitman N, Morrissey TK, Bunge RP, Aebischer P: Syngeneic Schwann-Cells Derived from Adult Nerves Seeded in Semipermeable Guidance Channels Enhance Peripheral-Nerve Regeneration. *J Neurosci* 1992, **12**(9):3310-3320.
- 135. Son YJ, Thompson WJ: Schwann-Cell Processes Guide Regeneration of Peripheral Axons. *Neuron* 1995, **14**(1):125-132.
- 136. Dai LS, Alt W, Schilling K, Retzlik J, Gieselmann V, Magin TM, Kappler J: A fast and robust quantitative time-lapse assay for cell migration. Exp Cell Res 2005, 311(2):272-280.
- 137. Sekine K, Tabata H, Nakajima K: Cell Polarity and Initiation of Migration.

 Comprehensive Developmental Neuroscience: Cellular Migration and Formation of Neuronal Connections 2013:231-244.
- 138. Han IS, Seo TB, Kim KH, Yoon JH, Yoon SJ, Namgung U: **Cdc2-mediated Schwann cell migration during peripheral nerve regeneration**. *J Cell Sci* 2007, **120**(2):246-255.
- 139. Theveneau E, Mayor R: Chapter 4 Neural Crest Cell Migration: Guidance, Pathways, and Cell-Cell Interactions. In Neural Crest Cells. Edited by Trainor PA. Boston: Academic Press; 2014:73-88.
- 140. Tomita K, Hata Y, Kubo T, Fujiwara T, Yano K, Hosokawa K: Effects of the in vivo predegenerated nerve graft on early Schwann cell migration: Quantitative analysis using S100-GFP mice. *Neurosci Lett* 2009, 461(1):36-40.

- 141. Barriga EH, Mayor R: Embryonic cell-cell adhesion: a key player in collective neural crest migration. *Curr Top Dev Biol* 2015, **112**:301-323.
- 142. Liu C, Pyne R, Kim J, Wright NT, Baek S, Chan C: **The impact of pre-stretch induced surface anisotropy on axon regeneration**. *Tissue Eng Part C Methods* 2015.
- 143. Bi XP, Crum BP, Li W: Super Hydrophobic Parylene-C Produced by Consecutive O-2 and SF6 Plasma Treatment. *J Microelectromech S* 2014, 23(3):628-635.
- 144. Wolf K, Mazo I, Leung H, Engelke K, von Andrian UH, Deryugina EI, Strongin AY, Brocker EB, Friedl P: Compensation mechanism in tumor cell migration: mesenchymal-amoeboid transition after blocking of pericellular proteolysis. *J Cell Biol* 2003, **160**(2):267-277.
- 145. Kulesa PM, Fraser SE: **Cell dynamics during somite boundary formation revealed by time-lapse analysis**. *Science* 2002, **298**(5595):991-995.
- 146. Jiang XY, Bruzewicz DA, Wong AP, Piel M, Whitesides GM: **Directing cell migration** with asymmetric micropatterns. *P Natl Acad Sci USA* 2005, **102**(4):975-978.
- 147. Kumar G, Ho CC, Co CC: **Guiding cell migration using one-way micropattern arrays**. *Adv Mater* 2007, **19**(8):1084-1090.
- 148. Lopez TJ, De Vries GH: **Isolation and serum-free culture of primary Schwann cells from human fetal peripheral nerve**. *Exp Neurol* 1999, **158**(1):1-8.
- 149. Reffay M, Petitjean L, Coscoy S, Grasland-Mongrain E, Amblard F, Buguin A, Silberzan P: Orientation and Polarity in Collectively Migrating Cell Structures: Statics and Dynamics. *Biophys J* 2011, **100**(11):2566-2575.
- 150. Hamilton DW, Oakley C, Jaeger NAF, Brunette DM: **Directional change produced by perpendicularly-oriented microgrooves is microtubule-dependent for fibroblasts and epithelium**. *Cell Motil Cytoskel* 2009, **66**(5):260-271.
- 151. Walboomers XF, Croes HJE, Ginsel LA, Jansen JA: **Growth behavior of fibroblasts on microgrooved polystyrene**. *Biomaterials* 1998, **19**(20):1861-1868.
- 152. Gerecht S, Bettinger CJ, Zhang Z, Borenstein JT, Vuniak-Novakovic G, Langer R: **The effect of actin disrupting agents on contact guidance of human embryonic stem cells**. *Biomaterials* 2007, **28**(28):4068-4077.
- 153. Teixeira AI, Abrams GA, Bertics PJ, Murphy CJ, Nealey PF: **Epithelial contact guidance on well-defined micro- and nanostructured substrates**. *J Cell Sci* 2003, **116**(10):1881-1892.
- 154. Mai JY, Sun C, Li S, Zhang X: A microfabricated platform probing cytoskeleton dynamics using multidirectional topographical cues. *Biomed Microdevices* 2007, 9(4):523-531.

- 155. Silver J, Miller JH: **Regeneration beyond the glial scar**. *Nat Rev Neurosci* 2004, **5**(2):146-156.
- 156. Schwab ME: **Nogo and axon regeneration**. Curr Opin Neurobiol 2004, **14**(1):118-124.
- 157. Blesch A, Tuszynski MH: **Spinal cord injury: plasticity, regeneration and the challenge of translational drug development**. *Trends Neurosci* 2009, **32**(1):41-47.
- Hurtado A, Moon LD, Maquet V, Blits B, Jerome R, Oudega M: Poly (D,L-lactic acid) macroporous guidance scaffolds seeded with Schwann cells genetically modified to secrete a bi-functional neurotrophin implanted in the completely transected adult rat thoracic spinal cord. *Biomaterials* 2006, 27(3):430-442.
- 159. Moore MJ, Friedman JA, Lewellyn EB, Mantila SM, Krych AJ, Ameenuddin S, Knight AM, Lu L, Currier BL, Spinner RJ *et al*: **Multiple-channel scaffolds to promote spinal cord axon regeneration**. *Biomaterials* 2006, **27**(3):419-429.
- 160. Stokols S, Tuszynski MH: **The fabrication and characterization of linearly oriented nerve guidance scaffolds for spinal cord injury**. *Biomaterials* 2004, **25**(27):5839-5846.
- 161. Chen BK, Knight AM, de Ruiter GCW, Spinner RJ, Yaszemski MJ, Currier BL, Windebank AJ: **Axon Regeneration through Scaffold into Distal Spinal Cord after Transection**. *J Neurotraum* 2009, **26**(10):1759-1771.
- 162. Pawar K, Cummings BJ, Thomas A, Shea LD, Levine A, Pfaff S, Anderson AJ: Biomaterial bridges enable regeneration and re-entry of corticospinal tract axons into the caudal spinal cord after SCI: Association with recovery of forelimb function. Biomaterials 2015, 65:1-12.
- 163. Tabesh H, Amoabediny G, Nik NS, Heydari M, Yosefifard M, Siadat SOR, Mottaghy K: The role of biodegradable engineered scaffolds seeded with Schwann cells for spinal cord regeneration. *Neurochem Int* 2009, **54**(2):73-83.
- 164. Bhatheja K, Field J: Schwann cells: Origins and role in axonal maintenance and regeneration. *Int J Biochem Cell B* 2006, **38**(12):1995-1999.
- 165. Riethmacher D, SonnenbergRiethmacher E, Brinkmann V, Yamaai T, Lewin GR, Birchmeier C: Severe neuropathies in mice with targeted mutations in the ErbB3 receptor. *Nature* 1997, 389(6652):725-730.
- 166. Jessen KR, Mirsky R: **The origin and development of glial cells in peripheral nerves**. *Nat Rev Neurosci* 2005, **6**(9):671-682.
- 167. Xu XM, Zhang SX, Li HY, Aebischer P, Bunge MB: **Regrowth of axons into the distal spinal cord through a Schwann-cell-seeded mini-channel implanted into hemisected adult rat spinal cord**. Eur J Neurosci 1999, **11**(5):1723-1740.

- 168. Tetzlaff W, Okon EB, Karimi-Abdolrezaee S, Hill CE, Sparling JS, Plemel JR, Plunet WT, Tsai EC, Baptiste D, Smithson LJ et al: A Systematic Review of Cellular Transplantation Therapies for Spinal Cord Injury. J Neurotraum 2011, 28(8):1611-1682.
- 169. Kanno H, Pressman Y, Moody A, Berg R, Muir EM, Rogers JH, Ozawa H, Itoi E, Pearse DD, Bunge MB: Combination of Engineered Schwann Cell Grafts to Secrete Neurotrophin and Chondroitinase Promotes Axonal Regeneration and Locomotion after Spinal Cord Injury. *J Neurosci* 2014, 34(5):1838-1855.
- 170. Liu C, Kray J, Toomajian V, Chan C: Schwann Cells Migration on Patterned PDMS Microgrooved Surface. Tissue Eng Part C Methods 2015, Submitted.
- 171. Sargoy A, Sun XP, Barnes S, Brecha NC: Differential Calcium Signaling Mediated by Voltage-Gated Calcium Channels in Rat Retinal Ganglion Cells and Their Unmyelinated Axons. *Plos One* 2014, 9(1).
- 172. Detzel CJ, Larkin AL, Rajagopalan P: **Polyelectrolyte multilayers in tissue engineering**. *Tissue Eng Part B Rev* 2011, **17**(2):101-113.
- 173. Decher G: Polyelectrolyte multilayer films: From interfacing molecules to propertyengineered materials. *Abstr Pap Am Chem S* 2000, **219**:U510-U510.
- 174. Qiu XP, Leporatti S, Donath E, Mohwald H: **Studies on the drug release properties of polysaccharide multilayers encapsulated ibuprofen microparticles**. *Langmuir* 2001, **17**(17):5375-5380.
- 175. Shiratori SS, Rubner MF: **pH-dependent thickness behavior of sequentially adsorbed layers of weak polyelectrolytes**. *Macromolecules* 2000, **33**(11):4213-4219.
- 176. Choi J, Rubner MF: Influence of the degree of ionization on weak polyelectrolyte multilayer assembly. *Macromolecules* 2005, **38**(1):116-124.
- 177. Caruso F, Niikura K, Furlong DN, Okahata Y: **Ultrathin multilayer polyelectrolyte** films on gold: Construction and thickness determination .1. Langmuir 1997, 13(13):3422-3426.
- 178. Dubas ST, Schlenoff JB: **Factors controlling the growth of polyelectrolyte multilayers**. *Macromolecules* 1999, **32**(24):8153-8160.
- 179. Schlenoff JB, Dubas ST: **Mechanism of polyelectrolyte multilayer growth: Charge overcompensation and distribution**. *Macromolecules* 2001, **34**(3):592-598.
- 180. Alberts B: *Molecular Biology of the Cell: Reference Edition*: Garland Publishing, Incorporated; 2008.

- 181. Vivet V, Mesini P, Cuisinier FJG, Gergelly C, Decher G: **Polyelectrolyte multilayer films containing poly**(**L-lysine**) **grafted with a RGD-tripeptide.** *Abstr Pap Am Chem S* 2002. **223**:U410-U410.
- 182. Gribova V, Auzely-Velty R, Picart C: Polyelectrolyte Multilayer Assemblies on Materials Surfaces: From Cell Adhesion to Tissue Engineering. Chemistry of Materials 2011, 24(5):854-869.
- 183. Mendelsohn JD, Yang SY, Hiller J, Hochbaum AI, Rubner MF: **Rational design of cytophilic and cytophobic polyelectrolyte multilayer thin films**. *Biomacromolecules* 2003, **4**(1):96-106.
- 184. Richert L, Boulmedais F, Lavalle P, Mutterer J, Ferreux E, Decher G, Schaaf P, Voegel JC, Picart C: Improvement of stability and cell adhesion properties of polyelectrolyte multilayer films by chemical cross-linking. *Biomacromolecules* 2004, 5(2):284-294.
- 185. Schonhoff M: **Self-assembled polyelectrolyte multilayers**. *Curr Opin Colloid In* 2003, **8**(1):86-95.
- 186. Decher G, Hong JD, Schmitt J: **Buildup of Ultrathin Multilayer Films by a Self-Assembly Process .3. Consecutively Alternating Adsorption of Anionic and Cationic Polyelectrolytes on Charged Surfaces**. *Thin Solid Films* 1992, **210**(1-2):831-835.
- 187. Sukhorukov GB, Mohwald H, Decher G, Lvov YM: Assembly of polyelectrolyte multilayer films by consecutively alternating adsorption of polynucleotides and polycations. *Thin Solid Films* 1996, **284**:220-223.
- 188. Sukhorukov GB, Schmitt J, Decher G: **Reversible swelling of polyanion/polycation** multilayer films in solutions of different ionic strength. *Ber Bunsen Phys Chem* 1996, **100**(6):948-953.
- 189. de Villiers MM, Otto DP, Strydom SJ, Lvov YM: **Introduction to nanocoatings produced by layer-by-layer (LbL) self-assembly**. *Advanced Drug Delivery Reviews* 2011, **63**(9):701-715.
- 190. Elbert DL, Herbert CB, Hubbell JA: **Thin polymer layers formed by polyelectrolyte multilayer techniques on biological surfaces**. *Langmuir* 1999, **15**(16):5355-5362.
- 191. Richert L, Engler AJ, Discher DE, Picart C: Elasticity of native and cross-linked polyelectrolyte multilayer films. *Biomacromolecules* 2004, **5**(5):1908-1916.
- 192. Izumrudov V, Kharlampieva E, Sukhishvili SA: **Salt-induced multilayer growth:** Correlation with phase separation in solution. *Macromolecules* 2004, **37**(22):8400-8406.
- 193. Collin D, Lavalle P, Garza JM, Voegel JC, Schaaf P, Martinoty P: **Mechanical properties of cross-linked hyaluronic acid/poly-(L-lysine) multilayer films**. *Macromolecules* 2004, **37**(26):10195-10198.

- 194. von Klitzing R: **Internal structure of polyelectrolyte multilayer assemblies**. *Physical Chemistry Chemical Physics* 2006, **8**(43):5012-5033.
- 195. Hubsch E, Ball V, Senger B, Decher G, Voegel JC, Schaaf P: Controlling the growth regime of polyelectrolyte multilayer films: Changing from exponential to linear growth by adjusting the composition of polyelectrolyte mixtures. *Langmuir* 2004, 20(5):1980-1985.
- 196. Porcel C, Lavalle P, Decher G, Senger B, Voegel JC, Schaaf P: Influence of the polyelectrolyte molecular weight on exponentially growing multilayer films in the linear regime. *Langmuir* 2007, **23**(4):1898-1904.
- 197. Wu ZR, Ma J, Liu BF, Xu QY, Cui FZ: Layer-by-layer assembly of polyelectrolyte films improving cytocompatibility to neural cells. *J Biomed Mater Res A* 2007, 81A(2):355-362.
- 198. Hillberg AL, Holmes CA, Tabrizian M: Effect of genipin cross-linking on the cellular adhesion properties of layer-by-layer assembled polyelectrolyte films. *Biomaterials* 2009, **30**(27):4463-4470.
- 199. Yeo SJ, Kang H, Kim YH, Han S, Yoo PJ: Layer-by-Layer Assembly of Polyelectrolyte Multilayers in Three-Dimensional Inverse Opal Structured Templates. ACS Applied Materials & Interfaces 2012, 4(4):2107-2115.
- 200. Wittmer CR, Phelps JA, Saltzman WM, Van Tassel PR: **Fibronectin terminated multilayer films: Protein adsorption and cell attachment studies**. *Biomaterials* 2007, **28**(5):851-860.
- 201. Richert L, Boulmedais F, Lavalle P, Mutterer J, Ferreux E, Decher G, Schaaf P, Voegel J-C, Picart C: Improvement of Stability and Cell Adhesion Properties of Polyelectrolyte Multilayer Films by Chemical Cross-Linking. *Biomacromolecules* 2003, 5(2):284-294.
- 202. Blacklock J, Vetter A, Lankenau A, Oupick ý D, Möhwald H: **Tuning the mechanical properties of bioreducible multilayer films for improved cell adhesion and transfection activity**. *Biomaterials* 2010, **31**(27):7167-7174.
- 203. Sun B, Flessner RM, Saurer EM, Jewell CM, Fredin NJ, Lynn DM: Characterization of pH-induced changes in the morphology of polyelectrolyte multilayers assembled from poly(allylamine) and low molecular weight poly(acrylic acid). *Journal of Colloid and Interface Science* 2011, 355(2):431-441.
- 204. Mermut O, Lefebvre J, Gray DG, Barrett CJ: **Structural and mechanical properties of polyelectrolyte multilayer films studied by AFM**. *Macromolecules* 2003, **36**(23):8819-8824.

- 205. Lehaf AM, Moussallem MD, Schlenoff JB: Correlating the Compliance and Permeability of Photo-Cross-Linked Polyelectrolyte Multilayers. *Langmuir* 2011, 27(8):4756-4763.
- 206. Picart C, Schneider A, Etienne O, Mutterer J, Schaaf P, Egles C, Jessel N, Voegel JC: Controlled Degradability of Polysaccharide Multilayer Films In Vitro and In Vivo. Adv Funct Mater 2005, **15**(11):1771-1780.
- 207. Sukhishvili SA: **Responsive polymer films and capsules via layer-by-layer assembly**. *Curr Opin Colloid In* 2005, **10**(1-2):37-44.
- 208. Venstrom KA, Reichardt LF: Extracellular-Matrix .2. Role of Extracellular-Matrix Molecules and Their Receptors in the Nervous-System. Faseb J 1993, 7(11):996-1003.
- 209. Gribova V, Gauthier-Rouvière C, Albig &-Rizo C, Auzely-Velty R, Picart C: Effect of RGD functionalization and stiffness modulation of polyelectrolyte multilayer films on muscle cell differentiation. *Acta Biomaterialia* 2013, **9**(5):6468-6480.
- 210. Cheng MY, Cao WL, Cao Y, Gong YD, Zhao NM, Zhang XF: **Studies on nerve cell affinity of biodegradable modified chitosan films**. *J Biomat Sci-Polym E* 2003, **14**(10):1155-1167.
- 211. Park KS, Kim SM, Kim MS, Lee I, Rhee JM, Lee HB, Khang G: Effect of cell-adhesive-molecule-coated poly(lactide-co-glycolide) film on the cellular Behaviors of olfactory ensheathing cells and Schwann cells. *J Appl Polym Sci* 2008, **107**(2):1243-1251.
- 212. Rao SS, Winter JO: Adhesion molecule-modified biomaterials for neural tissue engineering. Front Neuroeng 2009, 2:6.
- 213. Cai L, Lu J, Sheen V, Wang S: **Optimal poly(L-lysine) grafting density in hydrogels for promoting neural progenitor cell functions**. *Biomacromolecules* 2012, **13**(5):1663-1674.
- 214. Mazia D, Schatten G, Sale W: Adhesion of Cells to Surfaces Coated with Polylysine Applications to Electron-Microscopy. *J Cell Biol* 1975, 66(1):198-200.
- 215. Ai H, Meng H, Ichinose I, Jones SA, Mills DK, Lvov YM, Qiao X: **Biocompatibility of layer-by-layer self-assembled nanofilm on silicone rubber for neurons**. *J Neurosci Meth* 2003, **128**(1–2):1-8.
- 216. Thouas GA, Contreras KG, Bernard CC, Sun G-Z, Tsang K, Zhou K, Nisbet DR, Forsythe JS: Biomaterials for spinal cord regeneration: Outgrowth of presumptive neuronal precursors on electrospun poly(ε)-caprolactone scaffolds microlayered with alternating polyelectrolytes. In Engineering in Medicine and Biology Society, 2008 EMBS 2008 30th Annual International Conference of the IEEE: 20-25 Aug. 2008 2008; 2008:1825-1828.

- 217. Becker AL, Johnston APR, Caruso F: **Peptide Nucleic Acid Films and Capsules: Assembly and Enzymatic Degradation**. *Macromol Biosci* 2010, **10**(5):488-495.
- 218. Cai KY, Rechtenbach A, Hao JY, Bossert J, Jandt KD: **Polysaccharide-protein surface** modification of titanium via a layer-by-layer technique: Characterization and cell behaviour as pects. *Biomaterials* 2005, **26**(30):5960-5971.
- 219. Dhamodharan R, McCarthy TJ: **Adsorption of alginic acid and chondroitin sulfate-A to amine functionality introduced on polychlorotrifluoroethylene and glass surfaces**. *Macromolecules* 1999, **32**(12):4106-4112.
- 220. Wen XJ, Tresco PA: Effect of filament diameter and extracellular matrix molecule precoating on neurite outgrowth and Schwann cell behavior on multifilament entubulation bridging device in vitro. J Biomed Mater Res A 2006, 76A(3):626-637.
- 221. Truong YB, Glattauer V, Briggs KL, Zappe S, Ramshaw JAM: Collagen-based layer-by-layer coating on electrospun polymer scaffolds. *Biomaterials* 2012, **33**(36):9198-9204.
- 222. Aggarwal N, Altgärde N, Svedhem S, Michanetzis G, Missirlis Y, Groth T: **Tuning Cell Adhesion and Growth on Biomimetic Polyelectrolyte Multilayers by Variation of pH During Layer-by-Layer Assembly**. *Macromolecular Bioscience* 2013:n/a-n/a.
- 223. Gribova V, Auzely-Velty R, Picart C: **Polyelectrolyte Multilayer Assemblies on Materials Surfaces: From Cell Adhesion to Tissue Engineering**. Chem Mater 2012, **24**(5):854-869.
- 224. Yamanlar S, Sant S, Boudou T, Picart C, Khademhosseini A: Surface functionalization of hyaluronic acid hydrogels by polyelectrolyte multilayer films. *Biomaterials* 2011, 32(24):5590-5599.
- 225. Ai H, Meng HD, Ichinose I, Jones SA, Mills DK, Lvov YM, Qiao XX: **Biocompatibility** of layer-by-layer self-assembled nanofilm on silicone rubber for neurons. *Journal of Neuroscience Methods* 2003, **128**(1-2):1-8.
- 226. He W, Bellamkonda RV: Nanoscale neuro-integrative coatings for neural implants. *Biomaterials* 2005, **26**(16):2983-2990.
- 227. Thouas GA, Contreras KG, Bernard CC, Sun GZ, Tsang K, Zhou K, Nisbet DR, Forsythe JS: Biomaterials for spinal cord regeneration: outgrowth of presumptive neuronal precursors on electrospun poly(epsilon)-caprolactone scaffolds microlayered with alternating polyelectrolytes. Conf Proc IEEE Eng Med Biol Soc 2008, 2008:1825-1828.
- 228. Krsko P, McCann TE, Thach T-T, Laabs TL, Geller HM, Libera MR: Length-scale mediated adhesion and directed growth of neural cells by surface-patterned poly(ethylene glycol) hydrogels. *Biomaterials* 2009, 30(5):721-729.

- 229. Fukuda J, Khademhosseini A, Yeh J, Eng G, Cheng JJ, Farokhzad OC, Langer R: Micropatterned cell co-cultures using layer-by-layer deposition of extracellular matrix components. *Biomaterials* 2006, **27**(8):1479-1486.
- 230. Chien H-W, Chang T-Y, Tsai W-B: **Spatial control of cellular adhesion using photocrosslinked micropatterned polyelectrolyte multilayer films**. *Biomaterials* 2009, **30**(12):2209-2218.
- 231. Khademhosseini A, Suh KY, Yang JM, Eng G, Yeh J, Levenberg S, Langer R: Layer-by-layer deposition of hyaluronic acid and poly-L-lysine for patterned cell co-cultures. *Biomaterials* 2004, **25**(17):3583-3592.
- 232. Charest JL, Eliason MT, Garcia AJ, King WP: Combined microscale mechanical topography and chemical patterns on polymer cell culture substrates. *Biomaterials* 2006, **27**(11):2487-2494.
- 233. Chien HW, Chang TY, Tsai WB: **Spatial control of cellular adhesion using photocrosslinked micropatterned polyelectrolyte multilayer films**. *Biomaterials* 2009, **30**(12):2209-2218.
- 234. Horner PJ, Gage FH: **Regenerating the damaged central nervous system**. *Nature* 2000, **407**(6807):963-970.
- 235. Smeal RM, Rabbitt R, Biran R, Tresco PA: Substrate curvature influences the direction of nerve outgrowth. *Ann Biomed Eng* 2005, **33**(3):376-382.
- 236. Rajnicek AM, McCaig CD: Guidance of CNS growth cones by substratum grooves and ridges: effects of inhibitors of the cytoskeleton, calcium channels and signal transduction pathways. *J Cell Sci* 1997, **110**:2915-2924.
- 237. Gasser UE, Hatten ME: Neuron-glia interactions of rat hippocampal cells in vitro: glial-guided neuronal migration and neuronal regulation of glial differentiation. *J Neurosci* 1990, **10**(4):1276-1285.
- 238. Distasi C, Ariano P, Zamburlin P, Ferraro M: In vitro analysis of neuron-glial cell interactions during cellular migration. Eur Biophys J Biophy 2002, 31(2):81-88.
- 239. Houlgatte R, Mallat M, Brachet P, Prochiantz A: Secretion of Nerve Growth-Factor in Cultures of Glial-Cells and Neurons Derived from Different Regions of the Mouse-Brain. *J Neurosci Res* 1989, **24**(2):143-152.
- 240. Shah NJ, Macdonald ML, Beben YM, Padera RF, Samuel RE, Hammond PT: **Tunable** dual growth factor delivery from polyelectrolyte multilayer films. *Biomaterials* 2011, 32(26):6183-6193.
- 241. Chen X, Luo J, Wu W, Tan H, Xu F, Li J: The influence of arrangement sequence on the glucose-responsive controlled release profiles of insulin-incorporated LbL films. *Acta Biomater* 2012, **8**(12):4380-4388.

- 242. Li BY, Jiang BB, Boyce BM, Lindsey BA: Multilayer polypeptide nanoscale coatings incorporating IL-12 for the prevention of biomedical device-associated infections. *Biomaterials* 2009, **30**(13):2552-2558.
- 243. Cho Y, Lee JB, Hong J: **Tunable growth factor release from nano-assembled starch multilayers**. *Chemical Engineering Journal* 2013, **221**(0):32-36.
- 244. Macdonald ML, Samuel RE, Shah NJ, Padera RF, Beben YM, Hammond PT: **Tissue** integration of growth factor-eluting layer-by-layer polyelectrolyte multilayer coated implants. *Biomaterials* 2011, **32**(5):1446-1453.
- 245. Chung AJ, Rubner MF: **Methods of loading and releasing low molecular weight** cationic molecules in weak polyelectrolyte multilayer films. *Langmuir* 2002, **18**(4):1176-1183.
- 246. Vazquez E, Dewitt DM, Hammond PT, Lynn DM: Construction of hydrolytically-degradable thin films via layer-by-layer deposition of degradable polyelectrolytes. *J Am Chem Soc* 2002, **124**(47):13992-13993.
- 247. Macdonald M, Rodriguez NM, Smith R, Hammond PT: Release of a model protein from biodegradable self assembled films for surface delivery applications. *Journal of Controlled Release* 2008, 131(3):228-234.
- 248. Lankalapalli S, Kolapalli VRM: Polyelectrolyte complexes: A review of their applicability in drug delivery technology. *Indian J Pharm Sci* 2009, **71**(5):481-487.
- 249. Sato K, Yoshida K, Takahashi S, Anzai J-i: **pH- and sugar-sensitive layer-by-layer films and microcapsules for drug delivery**. Advanced Drug Delivery Reviews 2011, **63**(9):809-821.
- 250. Zhao Q, Li B: **pH-controlled drug loading and release from biodegradable microcapsules**. *Nanomedicine: Nanotechnology, Biology and Medicine* 2008, **4**(4):302-310.
- 251. Mehrotra S, Lynam D, Maloney R, Pawelec KM, Tuszynski MH, Lee I, Chan C, Sakamoto J: **Time Controlled Protein Release from Layer-by-Layer Assembled Multilayer Functionalized Agarose Hydrogels**. Adv Funct Mater 2010, **20**(2):247-258.
- 252. Novikova LN, Novikov LN, Kellerth JO: Survival effects of BDNF and NT-3 on axotomized rubrospinal neurons depend on the temporal pattern of neurotrophin administration. European Journal of Neuroscience 2000, 12(2):776-780.
- 253. Krewson CE, Klarman ML, Saltzman WM: **Distribution of Nerve Growth-Factor Following Direct Delivery to Brain Interstitium**. *Brain Research* 1995, **680**(1-2):196-206.
- 254. Wohl BM, Engbersen JFJ: **Responsive layer-by-layer materials for drug delivery**. *Journal of Controlled Release* 2012, **158**(1):2-14.

255. Kashiba H, Hyon B, Senba E: Glial cell line-derived neurotrophic factor and nerve growth factor receptor mRNAs are expressed in distinct subgroups of dorsal root ganglion neurons and are differentially regulated by peripheral axotomy in the rat. Neurosci Lett 1998, 252(2):107-110.